CREx Transverse Asymmetry Measurements

A dissertation presented to

the faculty of

the College of Arts and Sciences of Ohio University

In partial fulfillment

of the requirements for the degree

Doctor of Philosophy

Robert W. Radloff

August 2022

© 2022 Robert W. Radloff. All Rights Reserved.

This dissertation titled

CREx Transverse Asymmetry Measurements

by

ROBERT W. RADLOFF

has been approved for

the Department of Physics and Astronomy

and the College of Arts and Sciences by

Paul King

Lecturer of Physics and Astronomy

Florenz Plassmann

Dean, College of Arts and Sciences

Abstract

RADLOFF, ROBERT W., Ph.D., August 2022, Physics

CREx Transverse Asymmetry Measurements (155 pp.)

Director of Dissertation: Paul King

A number of recent experiments have been able to successfully measure the parity violating asymmetry of electron-nucleus scattering and use its value to constrain the nuclear structure. The most recent of these, the Calcium Radius Experiment (CREX), finished taking data in Hall A of Jefferson Lab in 2021, and successfully extracted a neutron radius for ^{48}Ca. While the main measurements of these experiments are parity violating, there is an increasing amount of interest in the parity conserving Beam Normal Single Spin Asymmetry (BNSSA) systematic. If not properly suppressed, the BNSSA can compete with or exceed the parity violating measurement. Recent attempts to model the contributions from standard model suppressed higher order diagrams have struggled to predict behavior of BNSSA for all nuclei.

This document reports new measurements of the BNSSA at a beam energy of 2.18 GeV for ^{12}C, ^{40}Ca, ^{48}Ca, and ^{208}Pb from the CREX running period. The values for ^{12}C, ^{40}Ca, and ^{48}Ca are found to agree with model predictions. The two values of calcium agree with each other, indicating no strong isotopic scaling. The value for ^{208}Pb is consistent with zero, in stark disagreement with model predictions. This thesis contains a discussion of how these values were measured, as well as a proposed method to phenomenologically scale models to bring them into closer agreement with world data at lower energies.

Acknowledgments

The list of people who've helped me along the path to where I am now is too long to fit in any document.

I'd like to thank my advisor Dr. Paul King for guiding me through this project, and teaching me what I needed to know to complete it. You hear a lot of horror stories of how some students are treated by their advisors, and I had those fears when I started grad school. Fortunately, Dr. King has always been happy to answer questions and support my work when I needed it. He always made me feel like my questions were worth asking, even when I thought I would look dumb for asking them. In all the hardships covid brought, I could not have asked for a more understanding person to work with.

I'd also like to thank Dr. Julie Roche for helping direct me through so much of my physics schooling and earlier research projects that lead me here. You have been an invaluable person to be able to talk to about all of my non-physics physics questions. Having somebody who has made a successful career in physics listen to me, tell me that they've been through the same situations, and offer real advice has been pivotal to my mental health. I probably wouldn't have made it through grad school without it.

Thank you to my committee members for taking time to read this whole thing. Hopefully I made it... bearable at least.

I also have to thank copper, who actually stuck with me through all of grad school(and most of undergrad). I always said we would get here eventually, I'm not sure you always believed me. But you were happy to stay regardless, and that's what counts.

At this point I will stop naming people to save room in the document for some physics. I'm thankful for everybody that stayed up all night in the physics offices in Clippinger to study with me, there is no way I would have made it through classes without y'all. I'll always cherish those hellish nights. I'm also thankful for all of my internet friends who probably won't read this because none of you know my real name.

I also have an immense appreciation for the other members of PREX-II/CREX collaboration. Only after talking to other people about their experiences in research have I realized how uncommon it is to have such a close knit and helpful group of collaborators. I wish I could have spent more than just a couple short years working together.

Lastly, I'd like to thank Dr. Georgeanne Purvinis, mom, for encouraging me to pursue science, helping me through my education, and getting me through life in general. I don't think I could come up with words to describe how thankful I am for everything you've done. But if you ask me a hard question on my defense I swear I will take this section out in the corrections.

This material is based upon work supported by the U.S. Department of Energy, Office of Science, Office of Nuclear Physics under contract DE-AC05-06OR23177. The PREX-II and CREX collaboration institutions were supported by the U.S. Department of Energy, the Natural Sciences and Engineering Research Council of Canada (NSERC), and the National Science Foundation (NSF). In particular, the Ohio University activities were supported by NSF awards 1614479 and 1913170.

Table of Contents

List of Tables

List of Figures

1 Introduction

In the endless pursuit of a greater understanding of the basic mechanics of the universe, the most simple questions often have the most complicated answers. The complex mingling of forces that makes our existence possible also makes predicting and measuring some basic properties of the microscopic world momentous goals. While there are many ways to approach unraveling these questions, nuclear physics takes arguably the most direct approach. The toolkit of experimental nuclear physics, while ever benefiting from new technologies and growing theoretical understanding, has had one tool remain consistent for most of its history. Scattering measurements are the foundation of this toolkit, present in every experiment in one way or another. Whether the source of particles is an accelerator, nuclear decay, or cosmological in origin, our window into the nuclear world often involves scattering.

The idea of the nucleus itself was born out of scattering experiments, namely the Geiger-Marsden Experiments, which served as inspiration for Rutherford's model of the dense atomic nucleus [1]. The previous theory, created by J.J. Thompson, included the assumption that the atom was made of a diffuse cloud of positive charge. The Geiger-Marsden experiments showed that the scattering of alpha particles was inconsistent with that assumption, and provided a set of experimental inputs that constrained Rutherford's model. Our theoretical understanding has come far since that time. We now know that the dense nucleus of Ruthorford's theory is a complicated system made of protons and neutrons, who are themselves complicated systems of quarks and gluons.

The theory we now use to describe these systems is the standard model of particle physics, which describes three of the four known fundamental forces of the universe. The electromagnetic and weak forces, whose interactions are defined by quantum electrodynamics (QED), and the strong force, whose interactions are defined by quantum chromodynamics (QCD). This framework has been successful in its ability to describe and

predict a wide variety of nuclear properties. To fully understand scattering off a nucleus requires an understanding of the fundamental forces that cause the parts of the nuclear system to organize themselves how they have. However, due to the nature of the theory, many exact calculations remain out of reach. To make matters worse, the standard model includes a significant number of free parameters, whose values are not predicted by theory alone. To compensate for these facts, most processes are described using situation specific models which use the standard model as a guide, but make assumptions where required to keep the theories manageable.

With this in mind, we return to the tools that created nuclear physics to test the assumptions that exist in our modern theories. There is still an enormous amount of information regarding nuclear structure that can be learned from scattering experiments.

2 Background and Motivation

2.1 The Calcium Radius Experiment

Figure 2.1

The PREX-II/CREX Logo, designed by Marisa Petrusky.

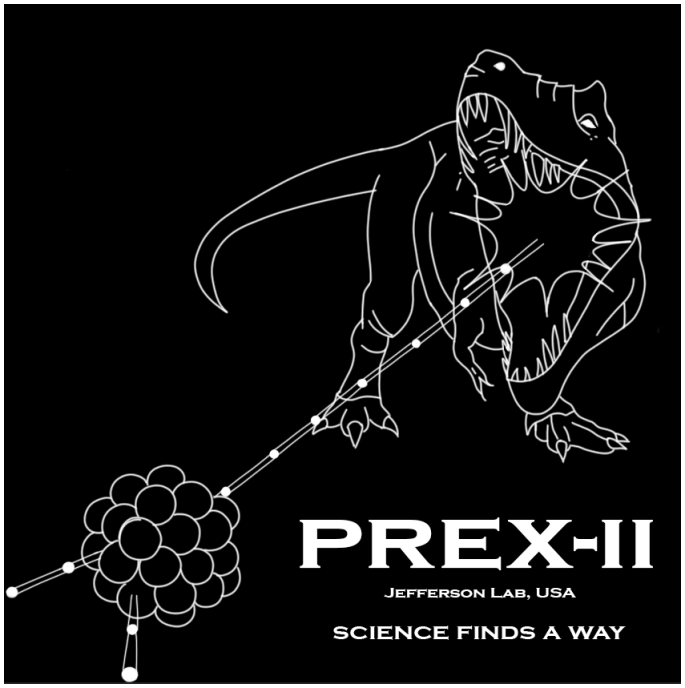

The Calcium Radius Experiment (CREX) ran in experimental Hall A during spring of 2020 at Thomas Jefferson National Lab. The main objective was to make a precision measurement of the weak charge radii of ^{48}Ca using parity violation electron scattering (PVES) as a probe. This measurement follows a long history of PVES experiments that made similar measurements on light nuclei(HAPPEx [2], QWEAK [3]) as well as very heavy nuclei(PREX, PREX-II). PREX-II and CREX ran consecutively, and shared one collaboration. The CREX measurements were designed to help bridge a gap in experimental knowledge left by other recent experiments by measuring an intermediate

mass nucleus, as well as providing the first information on the neutron scaling isotopic dependence.

The focus of this document is a set of auxiliary measurements of CREX, namely the corresponding beam normal single spin asymmetry (BNSSA) measurements. Taking advantage of the recently completed PREX-II setup allowed CREX to make BNSSA measurements of ^{12}C and ^{208}Pb at new kinematic, as well measurements on ^{40}Ca and ^{48}Ca. The measurements are mechanically similar to the main parity violating measurements, requiring a similarly rigorous set of analysis to properly constrain sources of uncertainty and background. However, the underlying physics that cause the process are very different, and therefore inspire their own discussion.

2.2 Electron Scattering By Nuclei

The standard model tells us that electrons only interact via the electromagnetic and weak forces. This makes them an interesting choice for probing the nucleus, an object whose structure is mostly controlled by strong force interactions. But it is precisely this fact that makes them a useful probe. While internally the forces that keep some nuclei bound are dominated by the strong force, the proton and neutron themselves are still particles that interact electroweakly. Using an electron probe keeps the scattering process cleanly defined by QED, while containing QCD elements of the nuclear structure behind the wall of form factors. QCD sets up the the scene, and we use QED to take a picture of the result.

2.2.1 Single Photon Exchange

The simplest description of electron nucleus scattering is given by a single photon exchange with the nucleus, shown in Figure 2.2. QED tells us that the scattering cross

Figure 2.2

A Feynmann diagram showing an electron exchanging one photon with a nucleus.

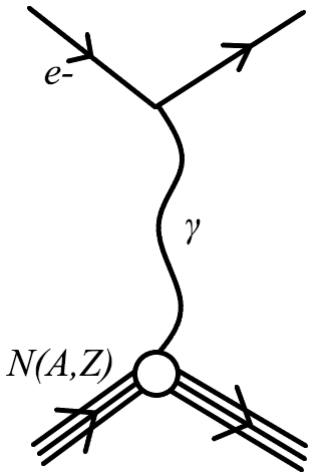

section can be written:

$$d\sigma = \frac{|\mathfrak{M}|^2}{F} dQ \tag{2.1}$$

where $F = 4((p_A \bullet p_B)^2 - m_A^2 m_B^2)^{1/2}$ is the "flux factor" for the process, dQ is the Lorentz invariant phase space factor (which conserves four momentum), and $\mathfrak{M}$ is the invariant amplitude for the diagram [4]. For relativistic electrons, the nucleus can be treated as a static charge distribution, and the invariant amplitude can be written [4]:

$$\mathfrak{M}_\gamma = \alpha[\bar{u_f}\gamma^\mu u_i]\left(\frac{g_{\mu\nu}}{q^2}\right)[j^\nu(q)] \tag{2.2}$$

where the first term, $[\bar{u_f}\gamma^\mu u_i]$, is the electron's vertex factor given in terms of initial and final Dirac spinors; the second term, $\left(\frac{-ig_{\mu\nu}}{q^2}\right)$, is the photon propagator given in terms of the four momentum transfer q and $g^{\mu\nu}$ tensor; and the third term, $[j^\nu(q)]$, is the vertex factor for the nucleus given in terms of its current $j^\nu(q)$.

For the case of a point like, spin-less nucleus of charge Ze, $j^{\nu}(x)$ is given by:

$$\begin{aligned} j^0(x) &= \rho(x) = Ze\delta(x), \\ j^{1,2,3}(x) &= 0 \end{aligned} \tag{2.3}$$

When Fourier transformed to momentum space, $j^0(q)$ becomes simply Ze. Combining this result with Equations 2.2 and 2.1 gives the Mott scattering cross section, expressed in the lab frame as [5]:

$$\left(\frac{d\sigma}{d\Omega}\right)_{Mott} = \frac{Z^2\alpha^2\cos^2\frac{\theta}{2}}{4E^2\sin^4\frac{\theta}{2}} \tag{2.4}$$

where α is the fine structure constant.

But the nucleus is not a point like particle. By making a change to equation 2.3 such that the delta function is replaced by a more general spatial distribution:

$$\begin{aligned} j^0(x) &= Ze\rho(x), \\ j^{1,2,3}(x) &= 0 \end{aligned} \tag{2.5}$$

The resulting cross section contains the same Mott scattering cross section calculated in equation 2.4, but this time the invariant amplitude is multiplied by a function that is the Fourier transform of the spatial distribution of charge in the nucleus. This function is called the charge form factor of the nucleus, denoted $F_{EM}(q)$ below.

$$\frac{d\sigma}{d\Omega} = \left(\frac{d\sigma}{d\Omega}\right)_{Mott} |F_{EM}(q)|^2 \tag{2.6}$$

Since neutrons have no net electric charge, the charge form factor is dominated by the spatial distribution of protons in the nucleus.

2.2.2 Weak Scattering

As mentioned at the start of the chapter, electrons can also interact weakly with a nucleus. This is thanks to a property of the standard model, known as electroweak unification, which states that the two forces are part of the same Lagrangian. In the Weinberg-Salam model the Lagrangian operates on the U(1) and SU(2) gauge groups,

which contain one (neutral) boson, and three (neutral, positive, negative) bosons respectively. The real neutral bosons, γ and Z^0, are combinations of the gauge fields, which causes them to mix at high energy. The Higgs mechanism is used to generate the masses of the bosons in a process called spontaneous symmetry breaking, at which point the H^0, Z^0, $W^{\pm}$, and the γ get their mass distribution. The relative strengths of the electroweak interactions are defined by the weak mixing angle θ_W:

$$\begin{aligned} \cos\theta_W &= \frac{M_W}{M_Z}, \\ \sin\theta_W &= \frac{e}{g} \end{aligned} \tag{2.7}$$

Where M_W and M_Z are the masses of the $W^{\pm}$ and Z^0 bosons, and g is a weak coupling constant similar to its electromagnetic counterpart e. Further discussion of this process is outside the scope of this document, more formal quantitative discussion can be found in Reference [4].

The weak force is mediated by the charged $W^{\pm}$, and the neutral Z^0 bosons. Charged current $W^{\pm}$ interactions are responsible for most of the observable effects of the weak force, such as for quark flavor changing and nuclear beta decay. Neutral current Z^0 interactions are responsible for more subtle processes, like neutrino scattering in cases where the flavor remains unchanged. Relevant to this document, the Z^0 can also mediate purely weak scattering between the electron and a nucleus. The main difference between these two forms of scattering is how the weak counterpart responds to the spin of the electron. A similar set of derivations to those shown in Section 2.2.1 can be used for the weak force counterpart of first order electron nucleus scattering, but some additional terms need to be defined and discussed first.

2.2.2.1 Parity, Helicity, and Chirality (oh my)

In Section 2.2.1 the Mott cross section was derived using QED. The electron was described using a set of Dirac Spinors that contain the electron's spin. However, the spin

dependence cancels out in the scattering off an unpolarized nucleus, and doesn't appear in the final cross section. The combination of the parity-odd geometry with the parity-even spin results in the spin reversing direction with respect to the momentum in a parity transform. In this case, we could invert all the spatial coordinates, resulting in a mirrored set of geometry, but an unchanged spin direction, and the process produces the same cross section. This is called a parity transformation. Parity transformations are useful for checking spin dependence because spin remains positive in the transform, therefore inverting the spin alone is equivalent to applying a parity transform.

The Dirac Spinors express the electron's spin in terms of their projections on to the momentum direction. This quantity is called the helicity:

$$H = \frac{\vec{S} \bullet \vec{p}}{|\vec{S}||\vec{p}|} \tag{2.8}$$

For massless particles, the helicity defines the handedness, or chirality, of the particle. But because the electron moves slower than the speed of light, this means the helicity is frame dependent. The more relativistic an electron is, the better estimate helicity becomes to the chirality. The weak force is actually sensitive to the chirality of the involved particles, and QED uses the γ^5 chiral projection operator to extract this information.

2.2.2.2 Parity Violating Electron Scattering

We can now follow the steps in Section 2.2.1 to write the cross section for weak scattering via a single Z^0. The invariant amplitude for diagram seen in Figure 2.3 is:

$$\mathfrak{M}_{NC} = \frac{g^2}{4\cos^2\theta_W}[\bar{u_f}\gamma^\mu(c_V^e - c_A^e\gamma^5)u_i]\left(\frac{-ig_{\mu\nu}}{q^2 + M_Z^2}\right)[j^\nu(q)] \tag{2.9}$$

where j^ν in this case is the weak current vertex factor for the nucleus, and $c_V = -\frac{1}{2}$ and $c_A = -\frac{1}{2} + 2\sin^2\theta_W$ are the vector and axial couplings for the electron, whose values are defined in the standard model.

Figure 2.3

A Feynmann diagram showing an electron exchanging one Z^0 with a nucleus.

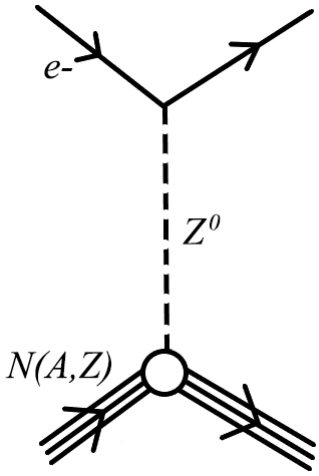

Using the same point like arguments for the distribution of weak charge would return a modified Mott equation, this time including a chirality dependence, as well as exchanging the factors of α for factors of g. This chirality dependence is due to the parity violating nature of the weak force vertex factors, and results in a different amplitude for opposite helicity states. We can then follow a similar separation of weak form factors from a point like scattering equation:

$$\frac{d\sigma}{d\Omega} = \left(\frac{d\sigma}{d\Omega}(H_{\pm})\right)_{Mott} |F_W(q)|^2 \tag{2.10}$$

where $F_W(q)$ is the Fourier transformed distribution of weak charge in the nucleus. The discrepancy between the proton and neutron contributions in this case is different from the electromagnetic case, as both nucleons have a net weak charge proportional to their quark contents. When the quark contributions, given in Table 2.1, are summed for the proton and neutron, the suppression factor is $\approx 0.07 : 0.99$. This results in a form factor that is much more sensitive to the distribution of neutrons rather than protons. The differences between the EM and weak distributions, as well as the pure proton and pure neutron distributions is

shown in Figure 2.4. We can use the precise measurements we have of the proton distribution from the world data of parity conserving electromagnetic scattering to extract a measurement of the neutron distribution.

Figure 2.4

A comparison of proton, neutron, electromagnetic, and weak density distributions of ^{208}Pb. Calculated with FSUGold. The blue circles represent the experimentally extracted charge distribution. Figure reproduced from Reference [6].

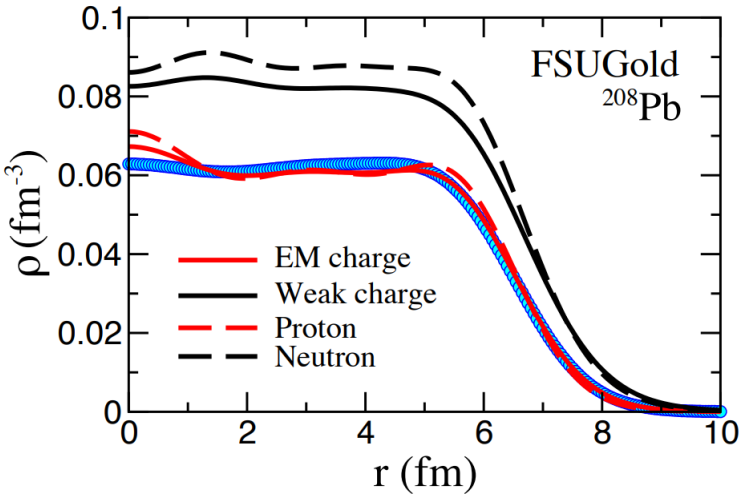

Table 2.1

Electromagnetic and weak quark charges for the up and down quarks, given as a function of θ_W [4].

Quark	EM Charge	Weak Coupling
u	$\frac{2}{3}$	$1 - \frac{8}{3}\sin^2\theta_w$
d	$-\frac{1}{3}$	$-1 + \frac{4}{3}\sin^2\theta_w$

2.2.2.3 Asymmetries

The parity conserving and parity violating parts of the electron nucleus scattering amplitudes are actually summed, namely, $\mathfrak{M}_{tot} = \mathfrak{M}_{\gamma} + \mathfrak{M}_{NC}$. Since the amplitudes are squared in the cross section, this results in the two terms producing interference. Considering $(\mathfrak{M}_{\gamma} \approx \frac{\alpha}{Q^2} \approx 10^{-2} GeV^{-2}) \gg (\mathfrak{M}_{NC} \approx \frac{g^2}{M_Z^2 \cos^2\theta_W} \approx G_F \approx 10^{-5} GeV^{-2})$, measuring weak scattering directly seems difficult when hidden behind its electromagnetic counterpart. But, by exploiting parity violation, we can cancel the parity conserving parts of the cross section using the asymmetry:

$$A_{PV} = \frac{d\sigma_+ - d\sigma_-}{d\sigma_+ + d\sigma_-} \tag{2.11}$$

Using equation 2.1 to substitute amplitudes in for the cross sections we can see:

$$A_{PV} = \frac{|\mathfrak{M}_{\gamma} + \mathfrak{M}_{NC}|^2 - |\mathfrak{M}_{\gamma} - \mathfrak{M}_{NC}|^2}{|\mathfrak{M}_{\gamma} + \mathfrak{M}_{NC}|^2 + |\mathfrak{M}_{\gamma} - \mathfrak{M}_{NC}|^2} \approx \frac{4\mathfrak{M}_{\gamma}\mathfrak{M}_{NC}}{2(\mathfrak{M}_{\gamma}^2 + \mathfrak{M}_{NC}^2)} \approx \frac{2\mathfrak{M}_{\gamma}\mathfrak{M}_{NC}}{\mathfrak{M}_{\gamma}^2} \tag{2.12}$$

results in a signal strength at the $\sim 10^{-7}$ or part per billion level. Including the form factors discussed in Sections 2.2.1 and 2.2.2.2 gives an estimated scaling of A_{PV} [7]:

$$A_{PV} \approx \frac{G_F Q^2}{4\pi\alpha\sqrt{2}} \frac{F_W(Q^2)}{F_p(Q^2)} \tag{2.13}$$

2.2.3 Multi-Photon Exchange

The Feynman diagram at the start of Section 2.2.1, namely Figure 2.2, contains an assumption that presents a problem when discussing signals at the part per billion level. Experimentally we can not choose that only this first order photon exchange happens. We make the assumption that only this diagram matters, since all of the other diagrams whose amplitudes would add to it are suppressed by factors of $\mathcal{O}(\alpha)$. Some of these diagrams are shown in Figure 2.5 for reference.

At first glance, one might assume that these electromagnetic interactions would cancel in the asymmetry and could be lumped in as corrections to the $\mathfrak{M}_{\gamma}$ term in Equation 2.12.

Figure 2.5

Some of the diagrams for higher order lepton nucleon scattering. Figure reproduced from Reference [8].

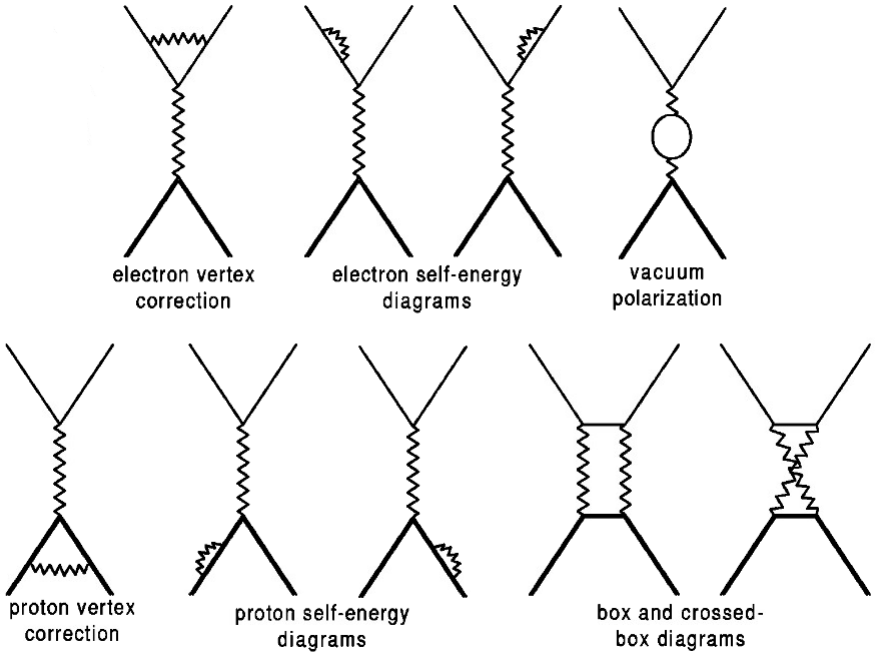

Figure 2.6

A two photon exchange Feynman diagram. Also called a box diagram.

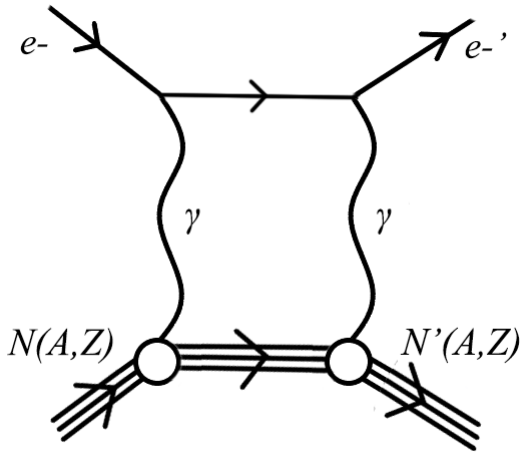

For the most part this is true, and to achieve the accuracy required for weak measurements these corrections are included. But the two photon exchange diagrams of the type shown in Figure 2.6 can enter measurements in complicated and surprising ways.

Recent reviews of experimental data measuring the ratio of the proton electric and magnetic form factors, such as the comparison of Rosenbluth separation to polarization transfer methods [9], have shown that these measurements can have a larger sensitivity to the two photon exchange than was originally predicted. This enhancement arises from interference between the real part of one and two photon amplitudes. Addition of the interference effects in the model calculation has been shown to contribute more significantly to the Rosenbluth measurement than the polarization transfer method. Including this correction in the results brings the two into agreement [9].

For transverse asymmetry measurements, De Rujula [10] showed that the two photon exchange is time reversal odd, and the interference between the imaginary part of one and two photon amplitudes creates an asymmetry that depends on the geometry of the scattering plane and the electron spin of the form:

$$A_T = \frac{\mathfrak{M}_\gamma \mathrm{Im}(\mathfrak{M}_{\gamma\gamma})}{|\mathfrak{M}_\gamma|^2}\left[\vec{S} \bullet \frac{\vec{p} \times \vec{p}'}{|\vec{p} \times \vec{p}'|}\right] \tag{2.14}$$

where $\vec{p}$ and $\vec{p}'$ are the initial and final electron momentum, and $\vec{S}$ is the electron's polarization, shown in Figure 2.7. When there is a spin component transverse to the momentum, this causes an asymmetry that varies azimuthally with respect to incident momentum. As a purely electromagnetic process, A_T is not parity violating, but due to its azimuthal dependence it can compete with the parity violating signal when sampled by finite solid angle detectors.

De Rujula calculated Eqn. 2.14 for electron-proton scattering using a modification to the proton's vertex term to provide bounds to the asymmetry in terms of the electric and magnetic form factors G_E and G_M. Functional forms of this asymmetry have been

Figure 2.7

Diagrams showing the important parameters for two photon exchange asymmetry. $\bar{p}, \bar{p}'$ *are the incoming and scattered electron momentum,* $\bar{S}$ *is the spin of the incoming electron,* $\hat{n}$ *is the scattering plane normal, and* ϕ *is the angle between the transverse spin component and* $\hat{n}$.

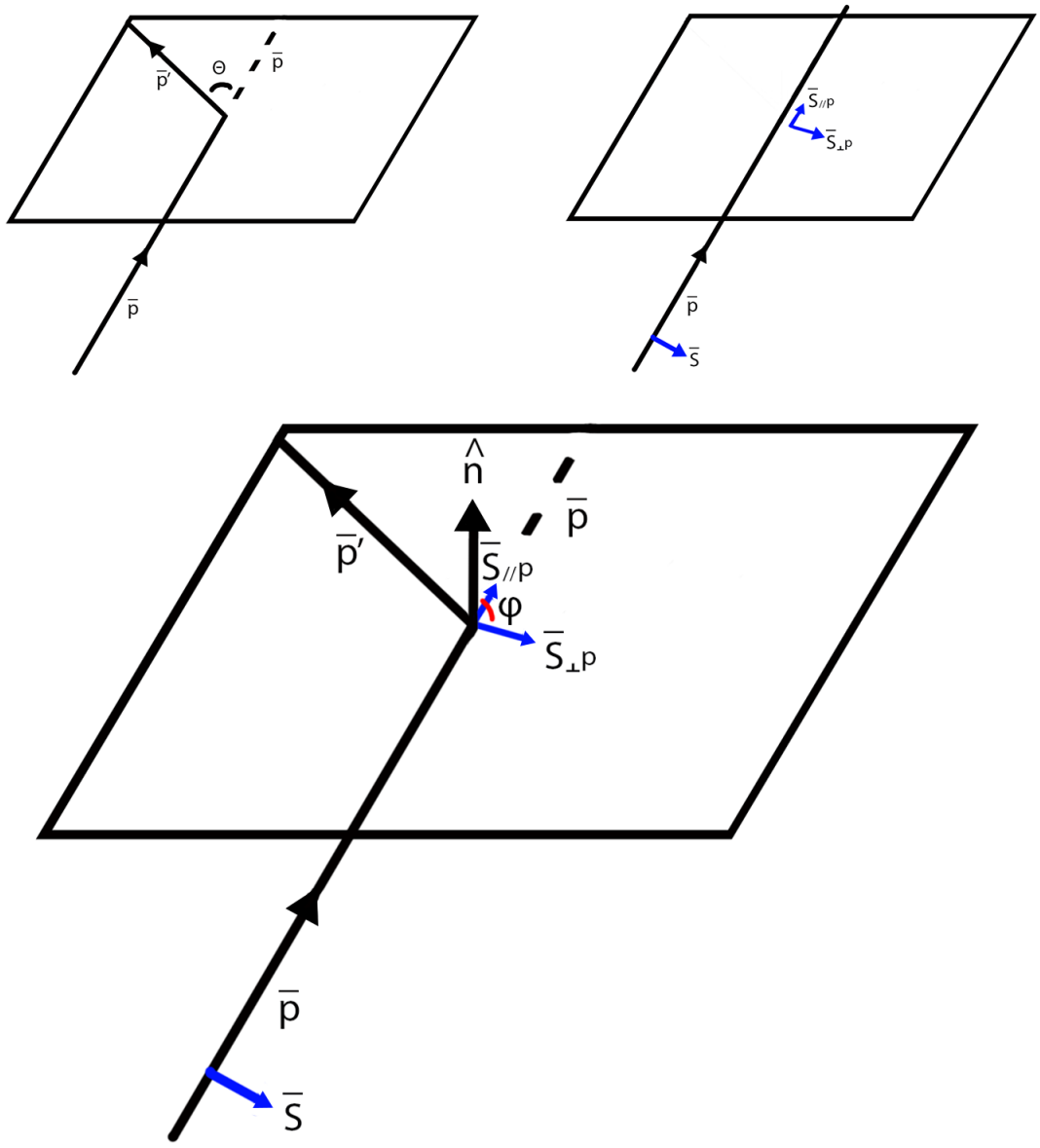

provided for small Q^2 by Afanasev [11] and more generally by Gorchtein [12] for the proton. However, attempts to follow this method for the nucleus have proven difficult. Initial assumptions that the nucleus would scale as the proton with a factor of $Z\alpha$ were quickly dismissed. Calculating the purely elastic contribution to the asymmetry has been done for a variety of nuclei using a method of numerically summing partial waves by Cooper and Horowitz [13]. This method captures resonances well, but underpredicts data in areas where inelastic contributions are dominant. Horowitz and Gorchtein [14] provide models that include the elastic contributions from the nucleus and combine them with scaled inelastic contributions from the proton, resulting in an asymmetry of the form:

$$A_T \approx A_{el} - \frac{m_e E_{lab} \sigma_{\gamma p} M}{8\pi^2 \sqrt{s}} \left(\frac{A}{Z}\right)\left(\frac{g_N(Q^2)}{F_N(Q^2)}\right) \tan\frac{\theta_{c.m.}}{2}\left(\ln\frac{Q^2}{m_e^2} - 2\right) \tag{2.15}$$

where $\sigma_{\gamma p}$ is the photo-absorbtion cross section, $g_N(Q^2)$ is the Compton form factor of the nucleus, and $F_N(Q^2)$ is the charge form factor of the nucleus. This method is in closer agreement with most data, but suffers from a large uncertainty in the scale factors attached to the inelastic contribution. Specifically, there is an absence of experimental data to constrain scaling of the Compton form factor, which is described with an exponential of the form $\exp\left[\frac{-B(Q^2)}{2}\right]$ [14]. Most recently Koshchii *et al.* [15] have attempted to use a modified absorbative potential in the Dirac formalism.

Koschii *et al.* [15] relate the Compton form factor to the virtual Compton tensor of a spinless target, $W^{\alpha\beta}$, which is itself a function of five Lorentz structures, $\tau_i^{\alpha\beta}$, and five corresponding amplitudes, $\mathfrak{F}_i$. In the forward angle and real Compton scattering limits, three of the five terms vanish, and the virtual Compton tensor is [15]:

$$W^{\alpha\beta} = \tau_1^{\alpha\beta}\mathrm{Im}\mathfrak{F}_1 + \tau_3^{\alpha\beta}\mathrm{Im}\mathfrak{F}_3 \tag{2.16}$$

The remaining two Lorentz structures of Equation 2.16, $\tau_{1,3}$, can be expressed in terms of the incoming and outgoing nucleus momenta (p_1, p_2), the two photon momenta (q_1, q_2),

and the combinations $\bar{q} = (q_1 + q_2)/2$, $\bar{p} = (p_1 + p_2)/2$:

$$\begin{aligned} \tau_1 &= q_1 q_2 g^{\alpha\beta} - q_1^\alpha q_2^\beta \\ \tau_3 &= (\bar{q}\bar{p})^2 g^{\alpha\beta} - \bar{q}\bar{p}(\bar{p}^\beta q_1^\alpha + \bar{p}^\alpha q_2^\beta) + (q_1 q_2)\bar{p}^\alpha \bar{p}^\beta \end{aligned} \tag{2.17}$$

The corresponding two amplitudes of Equation 2.16, $\Im_{1,3}$, can be expressed in terms of two structure functions F_1, F_2, and $x_{Bj} = Q^2/(2\bar{p}\bar{q})$ [15]:

$$\begin{aligned} Q^2 \Im_1 &= F_1 - \frac{F_2}{2x_{Bj}} \\ Q^2 \Im_3 &= -\frac{F_2}{\bar{p}\bar{q}} \end{aligned} \tag{2.18}$$

The exponential form of the Compton form factor enters in estimating the t dependence of $\Im_3$ using experimental Compton scattering. To first order in t the result is [15]:

$$\frac{\pi\alpha^2 M^2 \omega^2}{16} |\mathrm{Im}\Im_3|^2 \left(1 + \frac{\mathrm{Re}\Im_3}{\mathrm{Im}\Im_3}\right) \approx \frac{d\sigma}{d\Omega} \approx a \exp\left[- B|t|\right] F_{ch}^2(t) + \sigma_{inc} \tag{2.19}$$

Where $\omega = \frac{(p_1+q_1)^2 - M^2}{2M}$ and a, σ_{inc} are constants fit to the Compton scattering data [15].

These models still get much of their shape from the Compton form factor, and despite the inclusion of new experimental inputs, it contributes the largest source of uncertainty. This approach results in the closest theoretical description of the available experimental data yet. Despite this, the results of recent experiments, including PREX and CREX, demonstrate that no model has yet captured the behavior A_T across all measured nuclei. A detailed comparison between these models and existing data is contained in Section 5.1.

3 Lab Experimental Apparatus

Due to the precision nature of parity violation measurements, all parts of the accelerator system must be well understood. All experiments are designed with a goal of maximizing sensitivity to the signal, while minimizing sensitivity to background. While this is true in general for all experiments, small fluctuations in the qualities of the beam are often negligible to experiments that measure large changes. For example, if an experiment wanted to measure the cross section of electrons scattering off a lead target as a function of opening angle, they could place a detector on the horizontal plane of the beam and move it in a circle around the target. Since this cross section starts very large and drops rapidly as a function of angle, even very small shifts in the detector position at small angles will produce measurable changes in the signal above the background. If unwanted beam position fluctuations shift the background by 50%, but the background is one part per thousand, and the signal is 900 parts per thousand, a very precise measurement can still be made. However, at larger angles the cross section has dropped lower, and the signal might change at the same level as background fluctuations. To compensate for this, the experiment could place a second detector on the opposite side of the beam at the same angle and take the average of their signals, thereby canceling the sensitivity to horizontal position changes. This setup also allows the experiment to measure the size of horizontal fluctuations directly by taking the difference instead of average of what should be a symmetric signal.

The setup is largely the same for a spin sensitive measurement. We want to place detectors at positions where the maximum spin-dependent change in signal will be measured. But a parity violating signal is on the part per billion level, far below background signal for a single detector, and low enough that it can compete with the uncertainty in our ability to average out fluctuations using multiple detectors. Great care must be taken for this reason, as unexpected fluctuations of as little as a few microns are

enough to make data unusable if not handled properly. With careful attention, the fluctuations can be corrected out or their uncertainty contributions bounded systematically.

3.1 The Injector

The injector is the source of the polarized electrons used at CEBAF (Continuous Electron Beam Accelerator Facility). It can provides a continuous series of electron pulses at 1497 MHz up to 123 MeV [16]. The source has two gallium arsenide photoguns, seen on the left side of Figure 3.1, only one of which is active. The second gun is an older backup from a previous upgrade. The main gun is driven by three 499 MHz lasers. By giving each laser a phase with respect to the others, this set up allows halls A, B, and C to have individually controlled beam properties. The photoguns can produce a beam of 200 keV electrons at up 200 μA per hall [16]. The electron beam passes through a set of spin control magnets followed by a buncher and chopper to ensure separation between individual halls. The beam is then passed through a set of boosters and cryo-modules to reach the aforementioned 123 MeV.

Figure 3.1

The injector layout beginning with two photoguns (left) followed by beam line composed of focusing (FS) and spin solenoids (SS), Vertical (VW) and Horizontal (HW) Wien filters, quads (QW, QU), a buncher (PB) and beam position monitors (BP). Figure reproduced from Reference [17].

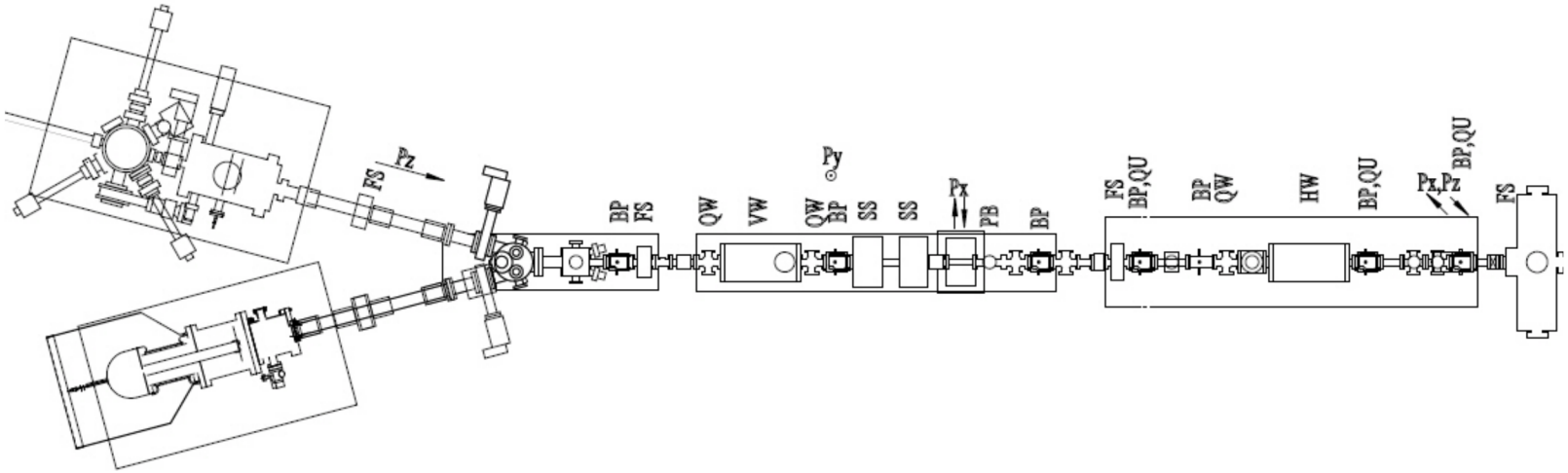

With this set up, hall D can be run in two different ways: If one hall is not currently ready for beam, hall D can divert one of the three laser's pulses. Or, if halls A, B, and C are running simultaneously, hall D run parasitically on a single hall by reducing its frequency to 250 MHz and diverting every other other pulse. These setups are shown in Figure 3.2. The latter option allows hall D to run simultaneously, but halves the current of another hall.

Figure 3.2

How RF kicker magnet timing aligns with laser pulses to allow for three or four hall running. Figure reproduced from Reference [18].

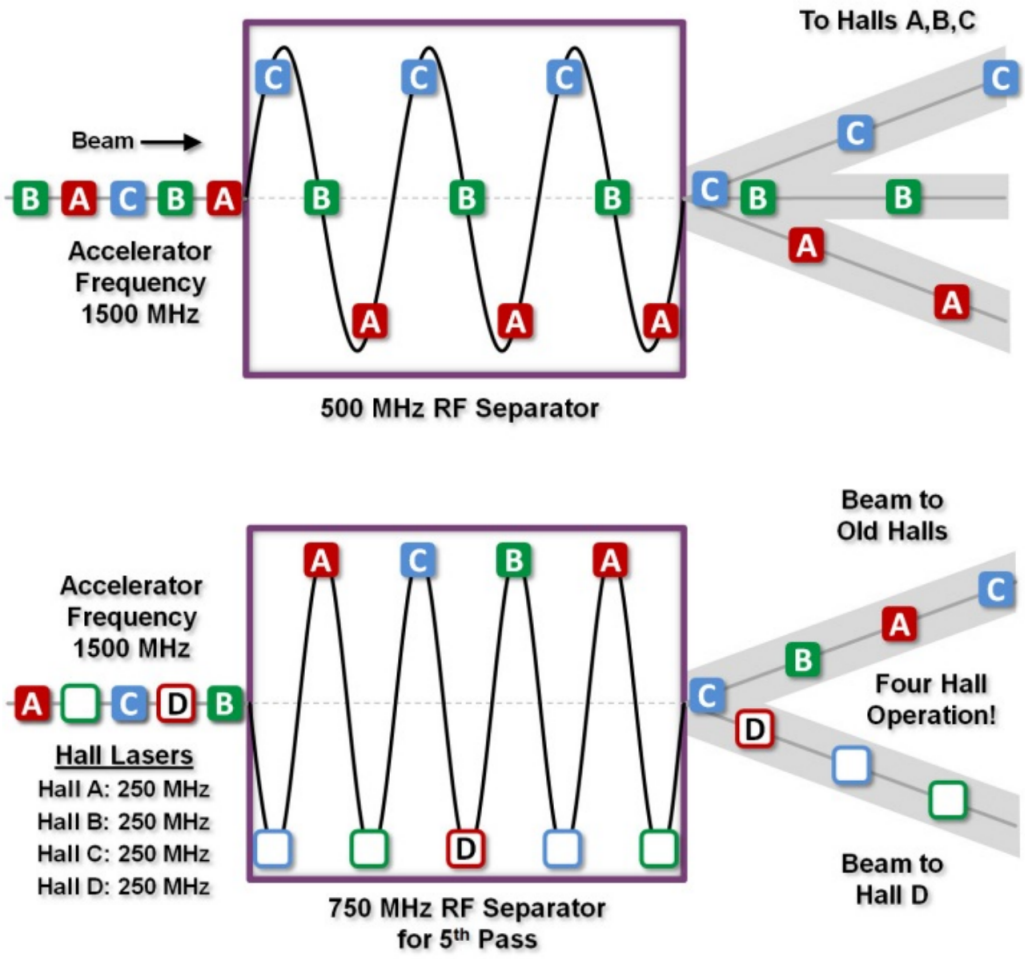

3.1.1 Spin Control

The injector has a litany of ways to control the polarization of the beam it supplies. These can be broken into the fast and slow spin control systems. The fast spin control is handled at the laser table, a diagram of which is shown in Figure 3.3. The lasers produce pulsed polarized linearly polarized light at 780 nm. Beams for halls A and B are combined using a 90/10 mirror, as hall B requires much lower intensity than the other halls. The pulses are combined inside a beam combiner prism, and the combined beam is sent to a Pockels cell. Pockels cells use the Pockels effect to induce birefringence in a crystal in response to an applied electric field. This allows them to turn linear polarized light into left and right circularly polarized light, and function as voltage controlled half wave plates, thereby swapping polarization at high frequencies. When it strikes the photocathode, the circularly polarized light preferentially excites bands in the gallium arsenide that free electrons of a particular spin state. This setup results in a rapidly toggle-able two state continuous stream of polarized electrons with polarization magnitude $> 90\%$.

The slow spin control system is largely used to constrain systematics associated with changing the polarization. There are multiple ways to change the polarization located at different points in the injector. The laser table has two half wave plates that minimize uncertainties related to the polarization of the laser before it reaches the photogun. The first is an insertable half wave plate (IHWP) which is placed before the Pockels cell. The IHWP was inserted and removed on a regular schedule, approximately every eight hours of data taking. It inverts the linear polarization which, in turn, swaps the helicity produced by a given voltage on the Pockels cell, resulting in roughly equal statistics using each polarization at the laser table. The second is a rotatable half wave plate (RHWP) which is placed after the Pockels cell. The RHWP is used to correct for undesired birefringent effects which result in deviations from the ideal performance of the phototocathode. The process for minimizing them is to use an intentional polarization induced transport

Figure 3.3

A diagram of how the three beams are combined on the laser table and where the spin control devices are located. Figure reproduced from Reference [19].

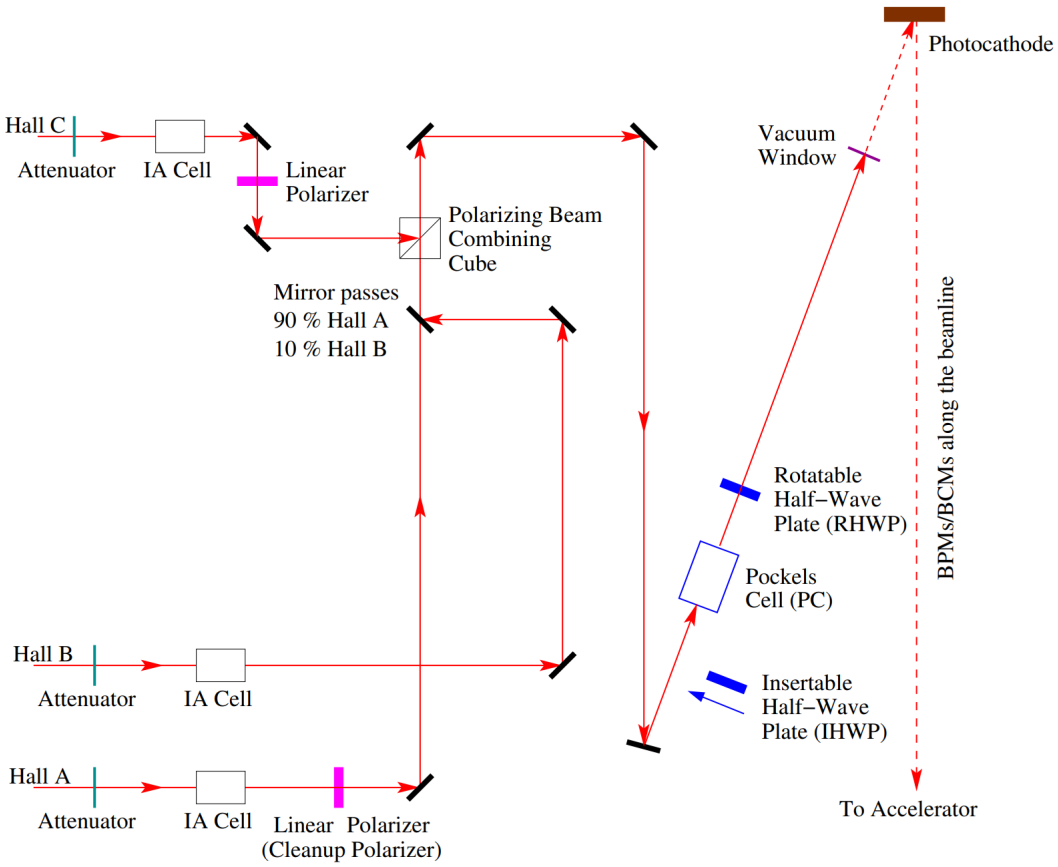

asymmetry to produce large position differences. The RHWP angle is then chosen to minimize the sensitivity to these differences [20]. Both devices require mechanical movement and therefore take more time to invert the polarization than the aforementioned fast control system.

The rest of the slow spin control system works on the electrons rather than the laser table. This is the part of the system that allows for precise control of the spin vector, rather than merely swapping states. The system consists of two Wien filters, (labeled horizontal

and vertical in reference to the axis about which they are able to rotate the spin) and two solenoid magnets arranged as shown in Figure 3.1.

Wien filters use orthogonal electric and magnetic fields to rotate the spin via Larmor precession in the magnetic field, while simultaneously canceling the Lorentz force using the electric field. An example Wien filter layout is shown in Figure 3.4. The relative strength of the fields must match the velocity, given by $v = \frac{E}{B}$ in order avoid changing the momentum. The frequency of spin precession is given by $\omega = \frac{egB}{2m_e}$. The rate of spin precession in the cavity can be adjusted by proportionally increasing the fields, as the frequency is only dependent on B.

Figure 3.4

A diagram of the inside of a Wien filter. The layout shown is for a vertical precession. Figure reproduced from Reference [17].

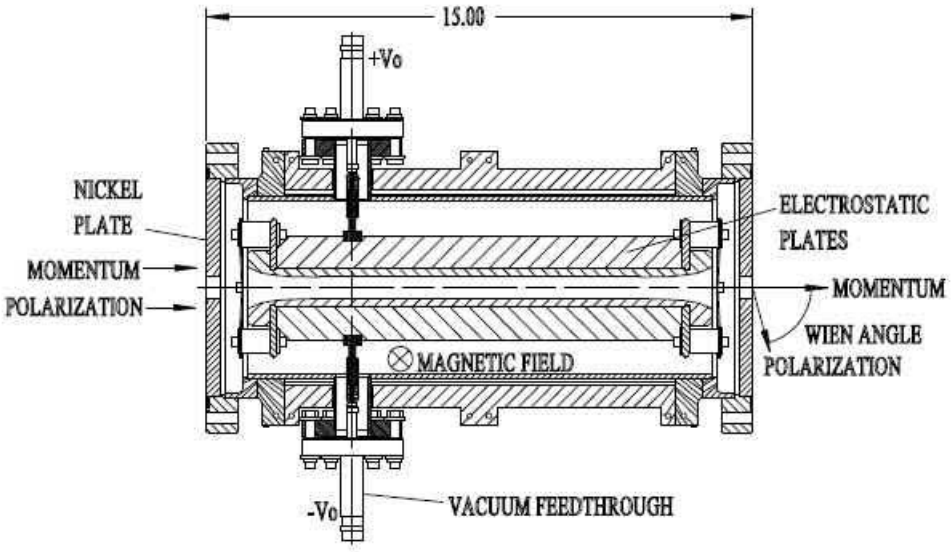

As another systematic check, the spin direction was also occasionally inverted using the solenoids. The solenoids cause azimuthal spin rotation, and are tuned to rotate the spin

from vertical to beam left, or beam right depending on the polarity. The focusing of the beam is not affected by the polarity of the solenoids, only the magnitude of their field strength, so a simple flip in polarity changes the effect on the spin while leaving the focusing unchanged. This combined arrangement allows the spin vector to be set by three orthogonal rotations. For transverse running, the polarization direction was set to vertical. The polarization was inverted via the Wien filters one time during the CREX main measurement to allow an approximately equal amount of data to be taken in each state.

3.2 Main Accelerator

After leaving the injector, the electron beam enters the main accelerator just before the start of the north linear accelerator (linac). The main accelerator consists of two anti-parallel 1.1 GeV linear accelerators, and five arcs that curve the beam between the north and south linac for each pass. Each pass the beam can be accelerated up to 2.2 GeV, passing through a different arc each cycle, resulting in a maximum energy of 12 GeV. A set of RF kicker magnets are located at the exit of the south linac. These serve to separate each hall's beam from the combined set by applying a magnetic kick at a set frequency. This setup allows each hall to request their own energy while sharing the main accelerator loop. For CREX, a single pass, 2.2 GeV beam was required.

Figure 3.5

A diagram showing a simplified layout of the main accelerator including the injector, north and south linacs, arcs, RF separators, and the experimental halls. Figure reproduced from Reference [21].

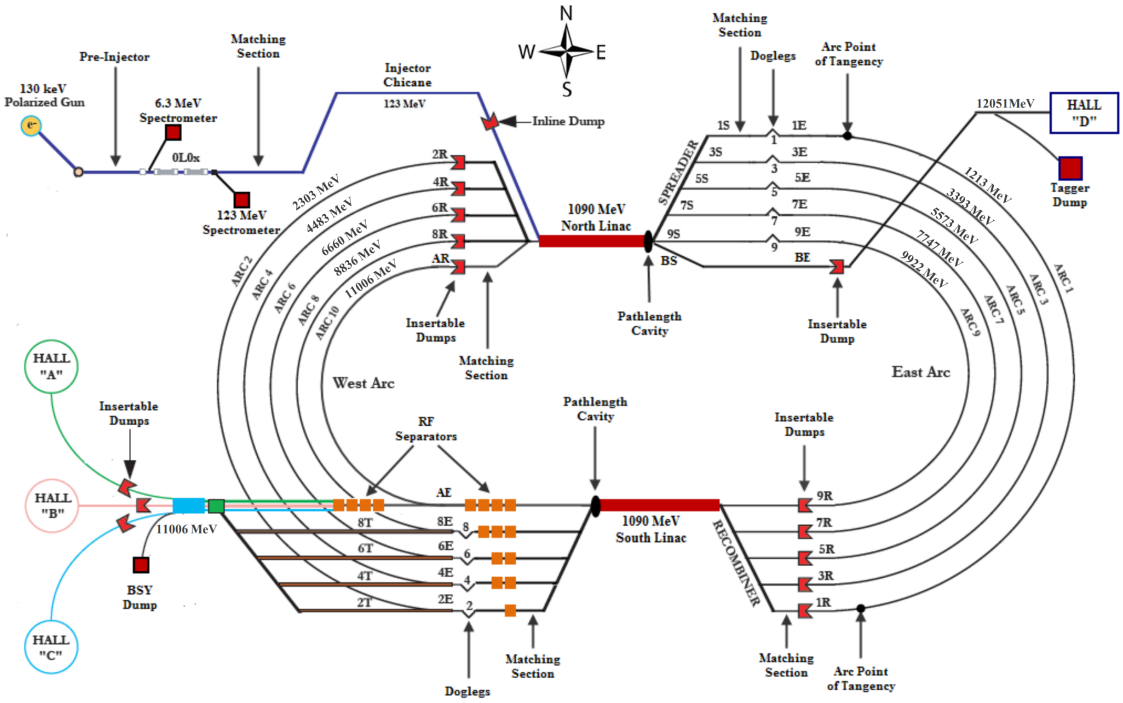

3.3 Beam Monitors

While there are hundreds of devices involved in monitoring the beam at CEBAF, some types provide information more directly relevant to the asymmetry than others. These monitors can be broken into a few main types, and are usually positioned at multiple locations along the beam line where they are most sensitive to what they aim to measure. Multiple hardware types are also often used to provide consistency checks on the same measured value.

3.3.1 Beam Position Monitors

Beam position monitors (BPM's) are placed in key locations throughout the accelerator to help with steering and to provide diagnostic information to subsystems. Due to the geometry of this experiment, having precise a measurement of the horizontal position is extremely important. Since the main detectors are fundamentally measuring how much charge scatters left versus right, any horizontal position changes must be known and well corrected for.

There are a few types of BPM hardware in use that compliment each others' weaknesses and provide cross checks on position measurements. The first type monitor the induced voltage on pickup antennas placed near the beam, shown for a vertical axis in Figure 3.6. While these devices can function with only one pair of wires for a one axis measurement, they usually have two pairs to reduce the uncertainty on the second axis. Since the induced voltage is proportional to the distance from the beam to each wire, using two wires in one of the following combinations

$$y = k\frac{U_{up} - U_{down}}{U_{up} + U_{down}} \quad \text{or} \quad x = k\frac{U_{left} - U_{right}}{U_{left} + U_{right}} \tag{3.1}$$

gives the relative position of the beam on the two wires' axis. Here k is a constant for each wire combination, and U_{X_i} are the voltages measured on the X_i wire. For BPM's located near bends in the accelerator like the arc, the vertical and horizontal axis are often rotated 45 degrees to avoid the extra noise and damage caused by synchrotron radiation.

The second type of BPM hardware are cavity monitors. These monitor the standing waves generated when the beam passes through a cylindrical cavity as shown in Figure 3.7. Pulling the position from zeroth and first order standing waves requires some amount of signal processing, which takes time to compute. This makes the cavity BPM's slower than their simple wire counterpart, but also results in a very precise measurement of the position.

Figure 3.6

A diagram showing a simplified layout of the vertical axis inside a BPM. Figure reproduced from Reference [22].

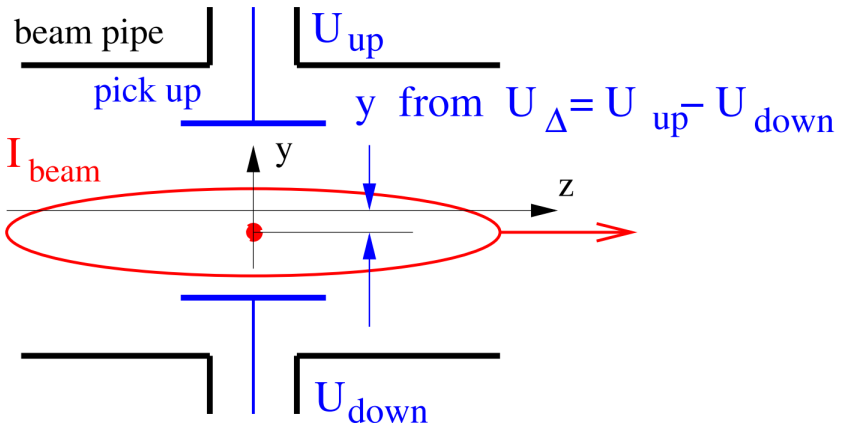

Figure 3.7

A diagram showing a simplified layout of a cavity BPM, as well as the form of the first and second order standing waves used to calculate the position. Figure reproduced from Reference [22].

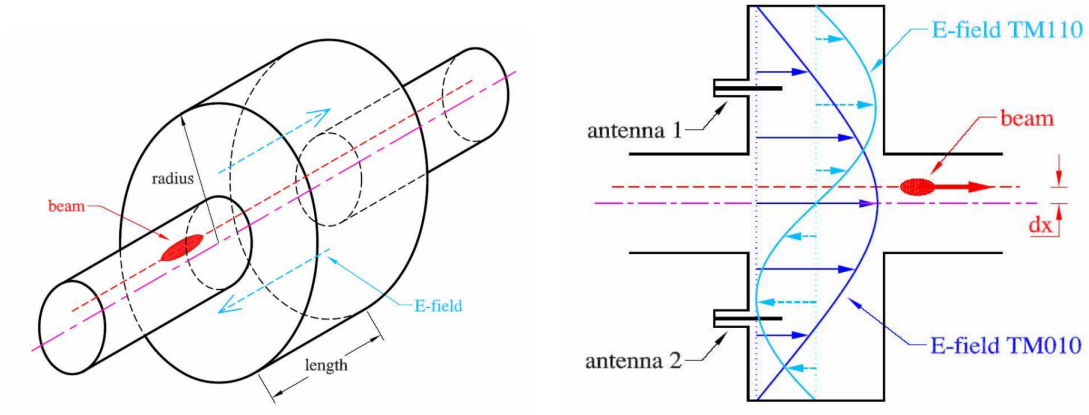

The final kind of BPM hardware used in the accelerator are harps. Harps are sets of thin wires that are physically moved through the beam to check its position. The current deposited in the wires rises and falls as the wires pass through the beam, and the center of the resulting peak corresponds to the center of the beam with respect to the wire's axis. Alternatively, instead of the harp wires being active elements, the wires can function as scattering targets, where the scattered beam is collected by downstream active elements. Combining both active elements are the so called "Super Harps". Harp scans give information about the shape of the beam that isn't easily available using the other methods. However, these measurements are invasive and require a devoted period of beam time to make. For this reason, they are not made often, and are only used for periodic calibrations.

3.3.2 Beam Charge Monitors

While CEBAF does have Faraday cup type devices for measuring beam current at low energy in the injector, the main method used at higher energies like this experiment are cavity monitors. CREX required a constant and accurate current readout, making destructive measurements like Faraday cups infeasible. Cavity monitors, like those shown in Figure 3.7, monitor the standing waves inside a cylindrical cavity. The amplitude of the waves is directly proportional to the current passing through the cavity.

The accelerator also used a parametric current transformer (PCT) called the "Unser" [23]. The Unser is an absolute current monitor that uses magnetic coils to measure the beam current. It is used to periodically calibrate the aforementioned cavity monitors, see the discussion in Section 4.3.3, but it suffers from pedestal drift over time. For this reason the cavity monitors are relied on for the main measurement. The layout of the main BCM's is shown in Figure 3.8.

Figure 3.8

The layout of the Unser, and the upstream and downstream cavity monitors. Figure reproduced from Reference [23].

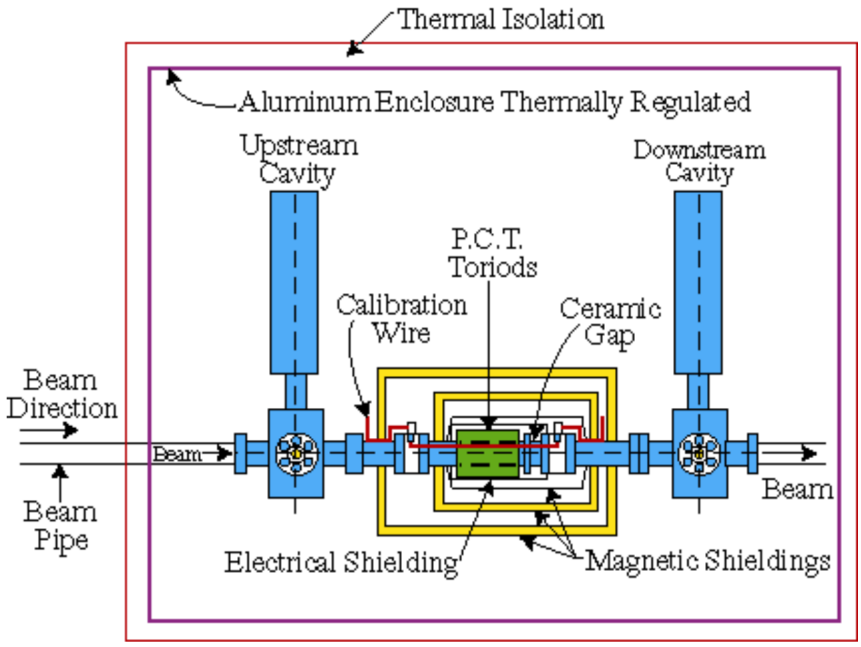

3.3.3 Beam Energy Monitors

The accelerator employs multiple methods of measuring the energy. All of these methods rely on knowing the rate at which electrons curve when passing through a magnetic field. In the case of constant velocity and B field, the radius is given by:

$$r = \frac{mv}{eB} \tag{3.2}$$

The most precise method to measure the energy that's still quick enough to use regularly is using the hall A spectrometer. The magnetic field in the spectrometer dipole is well known, and the main detector acceptance gives a reasonably good idea of the energy even in integrating mode.

Another way the energy was monitored during the experiment is the “Tiefenback” energy. This method measures the position of electrons in the ARC to measure the energy. The most sensitive BPM to this measurement was BPM 12, whose X coordinate aligned with the dispersive region in the arc. This was useful for checking for fluctuations in the energy of the beam in real time. The Tiefenback energy can be checked against the spectrometer’s energy to provide a crosscheck on the beam energy.

The last method to measure the energy is using harp scans. The beam switch yard is set to fully dispersive, and multiple harps are used to measure the beam’s trajectory before and after being bent into the hall as shown in Figure 3.9. The electrons pass through eight dipoles that are connected to the same power supply. A ninth identical dipole, connected to the same power supply, is kept separate from the beam line so a precise measurement of the field can be made for these measurements. This results in a very accurate determination of the field integral and electron trajectories involved in the energy calculation. These measurements are complimentary to the aforementioned measurement using BPM12, but they are invasive so they are only done as a way to calibrate the previously mentioned measurements.

Figure 3.9

The locations of the harps with respect to the eight dipole magnets used to bend the beam into the hall. Figure reproduced from Reference [24].

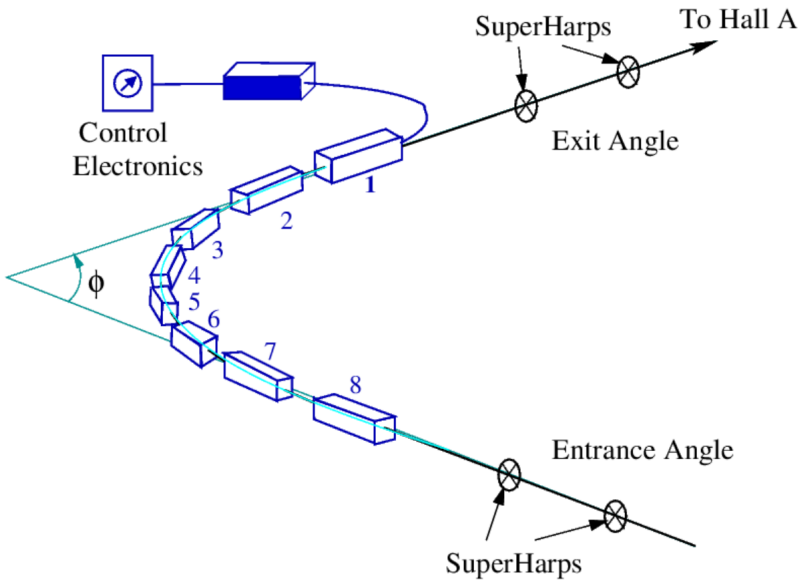

3.4 Polarimetry

As a parity experiment, monitoring polarization is of great importance. There are three polarization monitors that are used to reach the final value needed for analysis. The Mott polarimeter is located in the injector, and is used to measure the polarization of the source, while the Moller and Compton polarimeters provide complimentary measurements in the hall.

3.4.1 Moller Polarimeter

The Moller polarimeter uses Moller scattering of polarized electrons off of a polarized iron target. The iron target is polarized using a set of 3 T Helmholtz coils that result in a ~8% polarization in the foil. The scattered electrons are separated from the beam using a

set of quadrapole magnets, followed by a collimator, before a dipole magnet bends them away from the unscattered beam and into a calorimeter. The energy measured in the calorimeter is then proportional to the scattered electron flux. The layout can be seen in Figure 3.10. For the longitudinal case, the polarization is given by:

$$P_Z^{beam} = \frac{N_+ - N_-}{N_+ + N_-} \cdot \frac{1}{P^{foil} \cdot < A_{ZZ} >} \tag{3.3}$$

Where P_Z^{beam} is the measured beam polarization, $N_\pm$ are the measured scattering rates of the two beam helicity states, P^{foil} is the target polarization, and $< A_{ZZ} >$ is the analyzing power of the process, which is calculated using a Monte-Carlo simulation [25]. While this method gives a precise measurement of the polarization, it is destructive and requires a significant amount of beam time to make an accurate measurement.

The polarization value obtained by the Moller polarimeter before the CREX transverse run period was 86.9 ± 0.78% (0.14% from stat) [26]. These values were obtained using longitudinal polarization from measurements just before the transition to transverse data collection, as the polarimeters are not designed for transverse analysis, and rotating to vertical shouldn't affect the magnitude of the polarization vector.

Figure 3.10

A diagram showing the layout of the Moller polarimeter's YZ (top) plane and XZ (bottom) plane. The red lines show the intended path of scattered electrons entering the calorimeter. Figure reproduced from Reference [25].

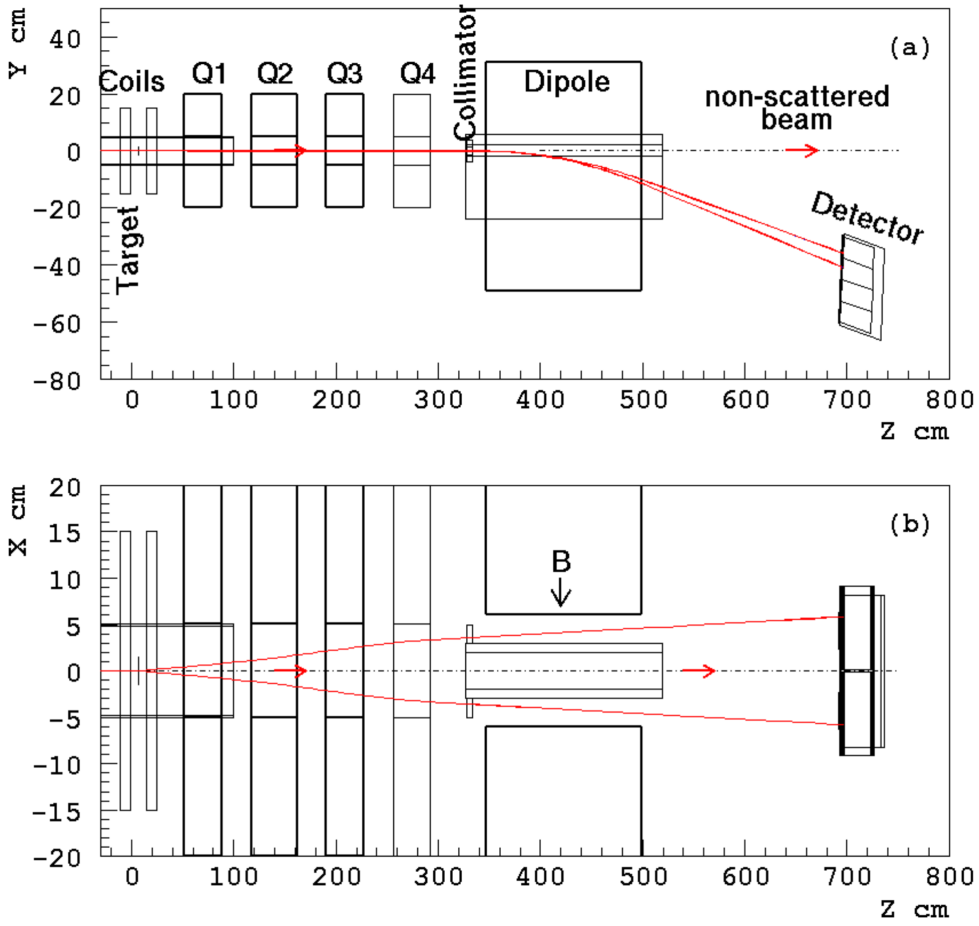

3.4.2 Compton Polarimeter

The Compton polarimeter uses Compton scattering of polarized electrons off a polarized photon target. The beam entering Hall A is diverted from it's path to a parallel target chamber using two dipole magnets shown in Figure 3.11. The chamber is a Fabry-Perot cavity which serves as a high intensity 10 kW photon target. The scattered

electrons, scattered photons, and remaining unscattered beam exit the far end of the cavity. The third dipole separates the outputs; the photons continue undeflected to the photon detector, while the scattered electrons are momentum selected to enter the electron detector. The unscattered electrons enter the fourth dipole and return to the main beam line.

The advantage to the Compton setup is that it can be run non-destructively unlike the Moller alternative. This allows for much more regular polarization measurements. The average polarization value obtained by the Compton polarimeter before and after the CREX transverse run period was 86.7 ± 0.63% (0.10% from stat) [26].

Figure 3.11

A diagram showing the layout of the Compton polarimeter. Figure reproduced from Reference [27].

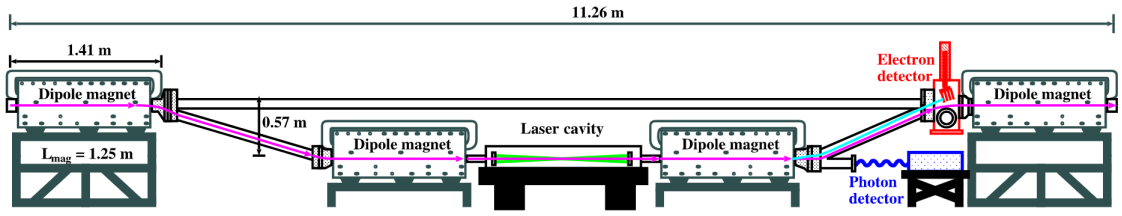

3.4.3 Mott Polarimeter

The Mott polarimeter uses low energy Mott scattering on a gold foil target. Unlike the Compton and Moller polarimeters, it is located in the injector to monitor the beam polarization of the source. The electrons enter the target chamber, scatter off the target, and are collected by four detectors at the back of the chamber, shown in Figure 3.12. The measured polarization is then given by:

$$\mathbf{P} = \frac{1}{S_{eff}(\theta)}[A_{LR}\hat{\mathbf{y}} - A_{UD}\hat{\mathbf{x}}] \tag{3.4}$$

Where **P** is the polarization vector, A_{LR} and A_{UD} are the asymmetries for the horizontally and vertically aligned detector pairs respectively, and $S_{eff}(\theta)$ is the effective Sherman function, which is calculated from the cross section. Like the Moller polarimeter, the Mott is invasive and requires turning off beam to all the halls for a devoted measurement.

Figure 3.12

A diagram showing the layout of the Mott polarimeter (top), and a zoomed in view of one the four detectors (bottom). Figure reproduced from Reference [28].

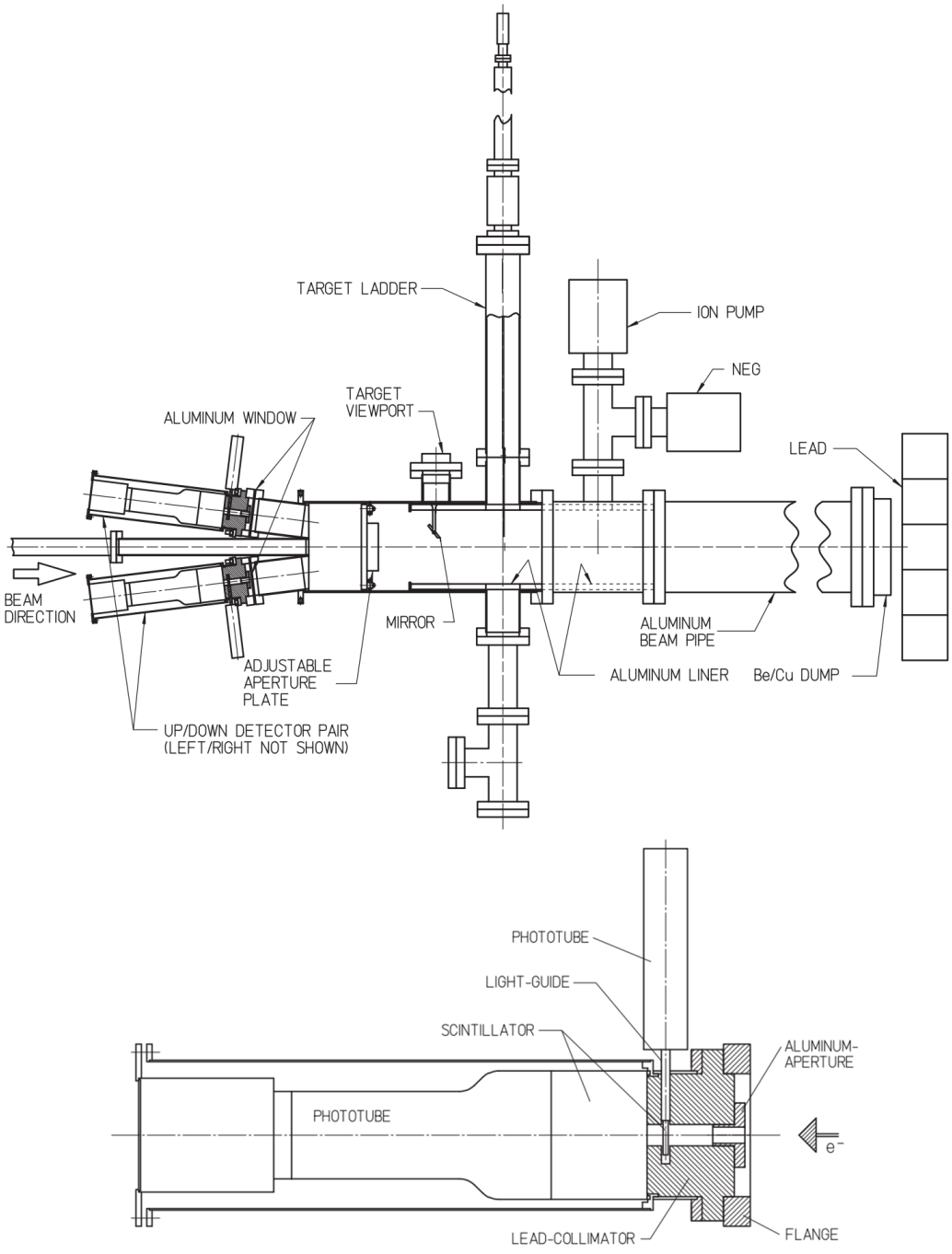

3.5 Target

The PREX and CREX experiments used a shared target chamber with a variety of individual targets for the main measurements as well as calibration. The targets, listed in Table 3.1, were divided between two adjustable ladder arms. The optics ladder contained a set of calibration targets designed to be used at low beam current with water rather than cryogenic cooling. This ladder was angled at a 45 degree angle with respect to the beam line as shown in Figure 3.13. The larger production ladder contained all the foils used for the main data collection. Due to the large amount of heat created by the high current beam, it was cooled cryogenically with helium.

Table 3.1

A table of all the targets on both the production and calibration ladders with their associated thicknesses. Figure reproduced from Reference [29].

Production Ladder	
Carbon Hole	~ 0.1 g/cm^2
(9X) ^{208}Pb/Diamond	0.5 mm
^{208}Pb/Graphite	0.5 mm
^{48}Ca (tilted)	1 ± 0.1 g/cm^2
^{40}Ca	1 ± 0.1 g/cm^2
thick C	0.5 ± 0.1 g/cm^2
Pb/Diamond	0.5 mm
Pb/Graphite	0.5 mm

Optics Ladder	
Carbon Hole	~ 0.1 g/cm^2
Watercell	
thin C foil	0.1 ± 0.05 g/cm^2
thin natural Pb	0.05 ± 0.01 g/cm^2
thin ^{40}Ca	0.05 ± 0.01 g/cm^2

Even with the intensive cooling on the production ladder, the targets degrade when exposed to the high current beam. To help remedy this, the beam is rastered across the surface of the target using a set of magnets. The frequency of the X and Y magnets are set to 25.56 kHz and 24.60 kHz respectively. The 960 Hz phase produces a Lissajous-like pattern whose size is proportional to the magnet field strength. The default raster size was 2x2 mm for CREX. The magnets frequencies were also set such that their cycles aligned

Figure 3.13

A CAD drawing of the entire target chamber, including both ladders and their mechanical supports. Figure reproduced from Reference [30].

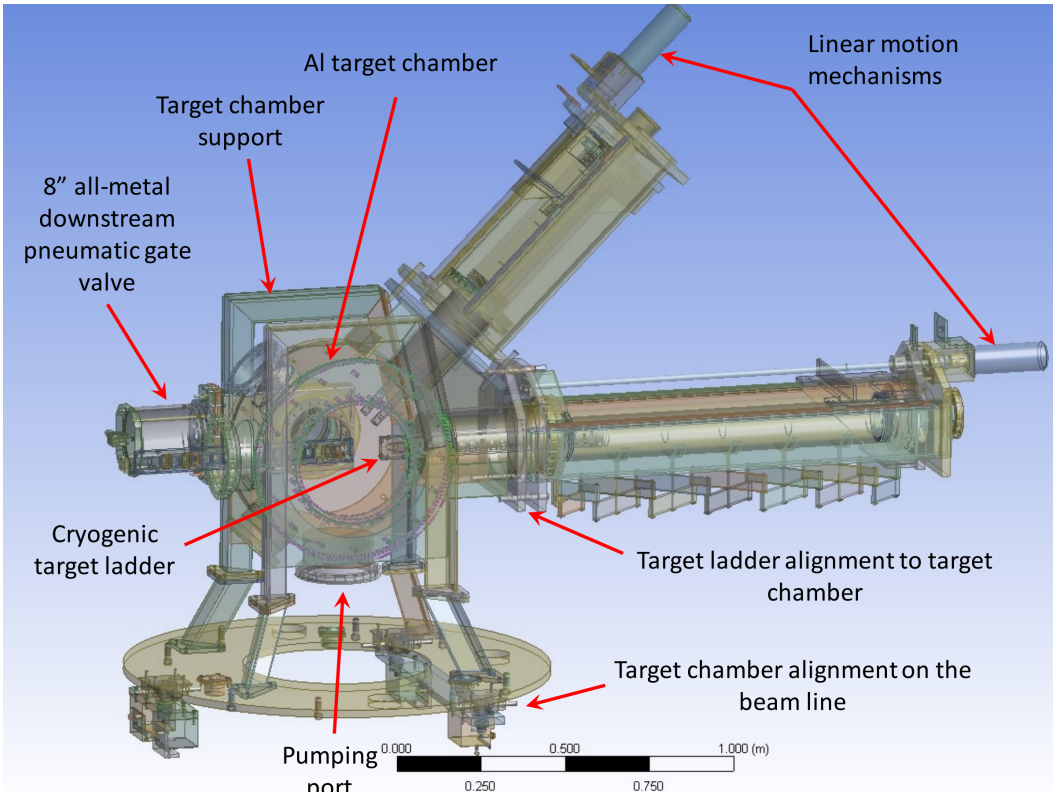

with helicity flips, so that the same pattern was traced in each helicity window. This helps to spread the heat more evenly across the whole target. Additionally, the lead targets were sandwiched between thin diamond windows to help dissipate heat on the surface before it reaches the softer lead. The thickness of the diamond windows was ~0.25 mm, while the thickness of the lead was ~0.55 mm [31]. Despite the effort to reduce the target degradation rate, at 70 μA the lead targets still have a finite lifetime and were constantly monitored for signs of damage. Anticipating this, nine duplicate lead production targets were prepared, seven of which were used in the combined experiments. Some examples of target degradation effects are shown in Figure 3.14. The effects of target damage were

visible in the form of changes in main detector rate, increased asymmetry widths, increased temperatures, and increased radiation rates in the both the hall neutron and ozone detectors.

Figure 3.14

Some of the lead targets in various states of degradation during the experiment. Figure reproduced from Reference [31].

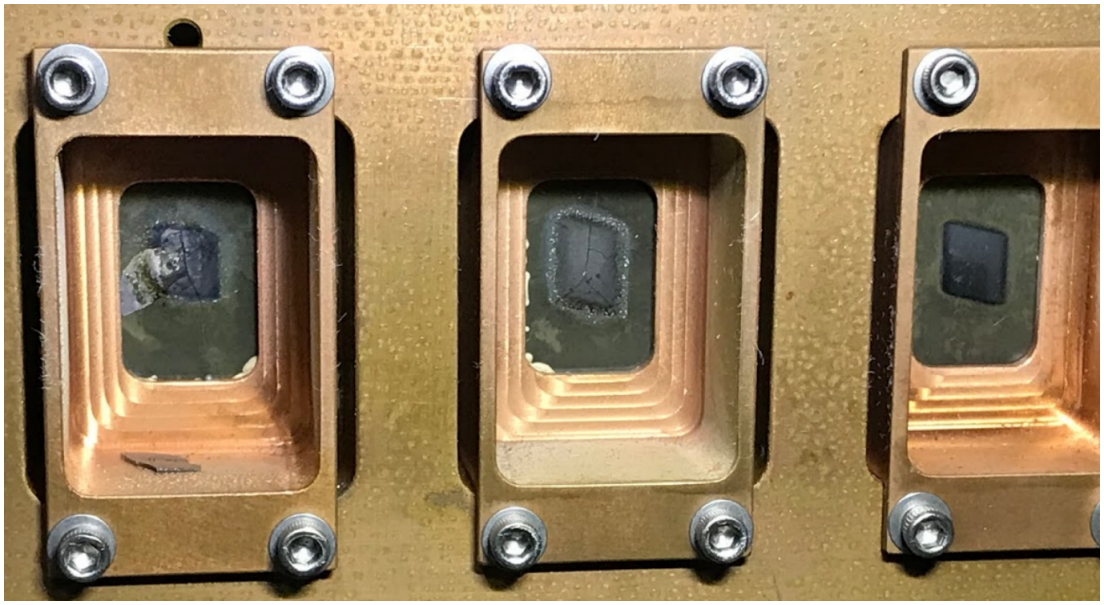

Due to both its cost and better temperature resistance, only one of each calcium target was used, measuring 6.72 mm and 5.76 mm for ^{40}Ca and ^{48}Ca respectively. However, a steering problem in the accelerator seriously damaged the ^{48}Ca target shortly after the transverse run period. a replacement was reassembled by combining it with two backup targets from a previous experiment.The layers of the sandwich had a slightly different purity than the original target, shifting the isotopic purity from 95.99% to 90.04%. The resulting replacement target had a thickness of 5.7 mm, but a correction was required to account for the change in isotopic purity.

The carbon hole target was used for checking the beam position, as well as the size of the raster. By setting the raster magnet currents, then imaging a hole of known size, the actual size of the raster square can be checked. Since the movement of the target ladder is also measured precisely, the carbon hole also helps confirm the beam is centered on the target. An example image of the carbon hole target for two raster sizes is shown in Figure 3.15. The water cell target is used for checking the energy separation of the detectors by simultaneously measuring the elastic scattering peaks of oxygen and hydrogen. The solid carbon foil targets were used to have a measured value for carbon asymmetry to subtract from the lead production targets during the carbon dilution analysis. The thin calcium and natural lead targets were used for safety and basic alignment checks to prevent damage to the production targets.

Figure 3.15

Two runs taken back to back to check two different raster sizes taken from the Hall A online logbook. The circle that appears in both is the empty part of the carbon hole target. The 2D plots are millimeters in x and y, color represents counts, while the 1D plots give millimeters on the x axis and counts on the y axis.

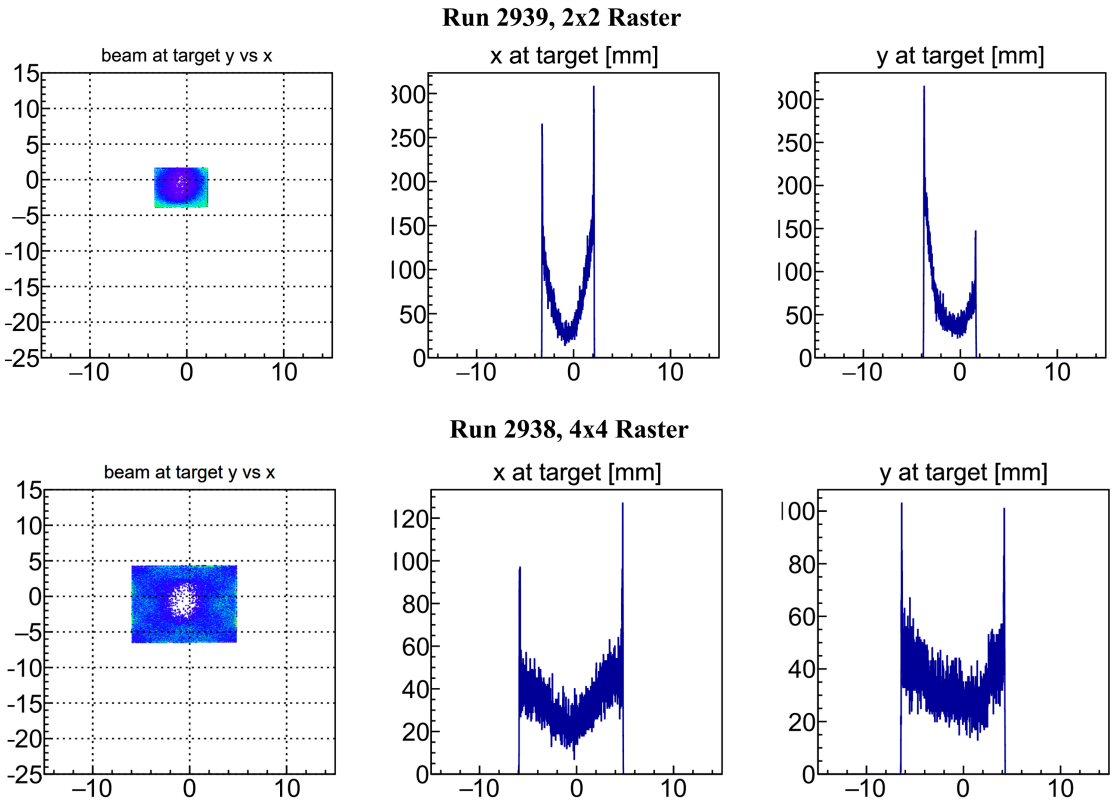

3.6 Sieve

The sieve collimators are thin metal (0.2 in) steel plates with asymmetric patterns of holes drilled in them. The hole layouts are visible in Figure 3.16. The irregular size and spacing of the holes produce a clearly identifiable pattern that can be analyzed in tracking mode to extract scattered electron trajectories. The extracted pattern can be compared to

simulation results to correct for a variety of effects related to the finite acceptance of the detectors.

Figure 3.16

A picture of the two sieve collimators prior to installation. The hole in the center is for the beam dump vacuum pipe.

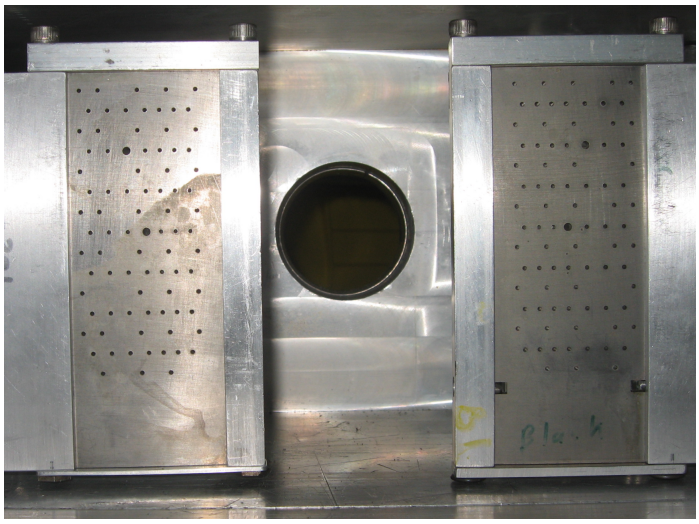

3.7 Septum Magnets

Due to the size of the the Hall A spectrometers, the closest they can be positioned to the beam line gives them a 12.5 degree angular acceptance. To extend this acceptance to smaller angles, such as the 5 degrees required by this experiment, an additional magnet known as the septum is used. The septums are thin dipole magnets placed nearly on top of the traditional Hall A target position, requiring the target to be pushed back upstream. Using anti-parallel fields, they bend scattered electrons in the 5-12 degree angle range away from the beam line to meet the existing spectrometer's acceptance. The center of the beam remains undeflected and passes through the gap in the magnets visible in Figure 3.17.

Figure 3.17

A picture of septum magnets and the beam pipe layout looking downstream of the target. The bare coils (left) are not visible after installation as they are covered by shielding. The vacuum pipes for the beam dump and left and right spectrometer can be seen passing through the shielding before the enter the septum (right) [32].

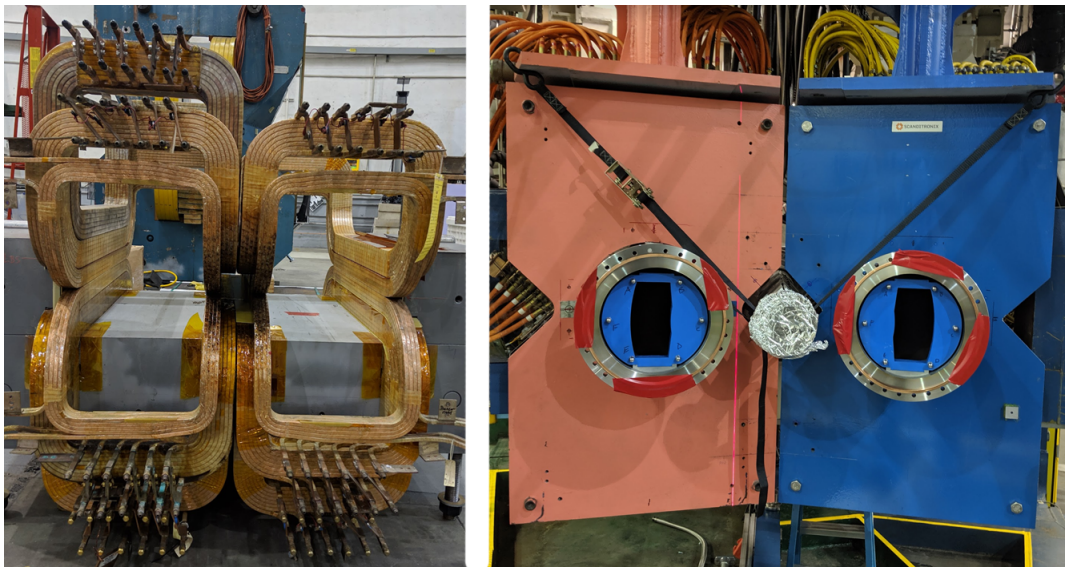

3.8 Hall A Spectrometers

Hall A contains two movable high resolution spectrometers composed of two identical sets of magnets and two similar sets of detectors. For a parity experiment, having both spectrometers on the horizontal plane with a symmetric acceptance allows for a better control of position correlated asymmetries. The standard detector packages of the left and right spectrometer can be seen in Figure 3.18. However, in order to avoid unnecessary radiation damage, much of this package was removed prior to the run, leaving only the vertical drift chambers (VDC) and scintillators S0 and S3. In addition to the remaining VDC's and scintillators, a set of gas electron multiplier (GEM) were installed for low

current tracking, as well as the main and AT quartz bars. The full layout is shown in Figure 3.19.

Two distinct configurations of the aforementioned detectors were used during the experiments; low current tracking mode, and high current integrating or production mode. The goal of tracking mode is to collect information about individual electron trajectories. In this configuration, the two VDC planes provide the electron's trajectory, while the scintillators give timing information for triggering. Both of these detectors saturate at the mega-Hertz count-rate scale, however, so they can not be used at the giga-Hertz count-rate scales needed in the production case. In production mode, the VDC's and scintillators are turned off and only the main detectors are used. When running in integrating mode, the main detectors gain is lowered to prevent saturation.

Figure 3.18

Diagrams of the left and right spectrometer's standard detector packages. Most of the detectors pictured were removed prior to running PREX-II and CREX. Figure reproduced from Reference [33].

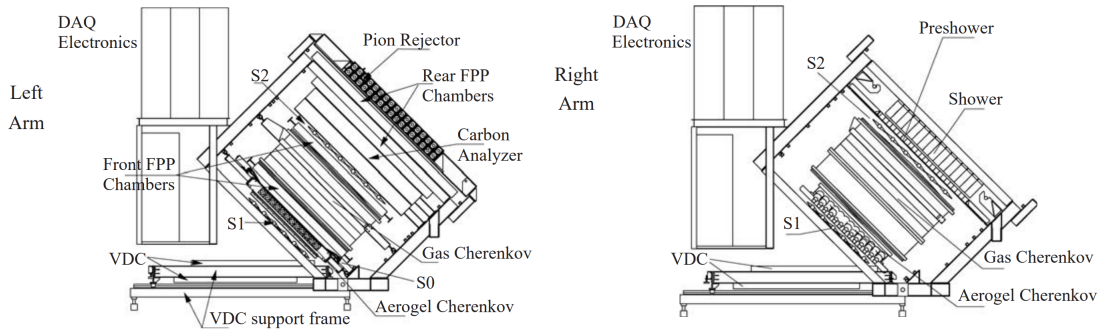

Figure 3.19

A simplified diagram of the layout of the Hall A detector package from target onward. The red tracks represent elastically scattered electrons, which hit the main detector quartz bars. The pink tracks represent the inelastic excited states, which intentionally miss the main detector bars. The vertical drift chambers (VDCs) and gas electron multiplier (GEM) detectors are only used at low beam currents to track the particle trajectories. Figure reproduced from Reference [34].

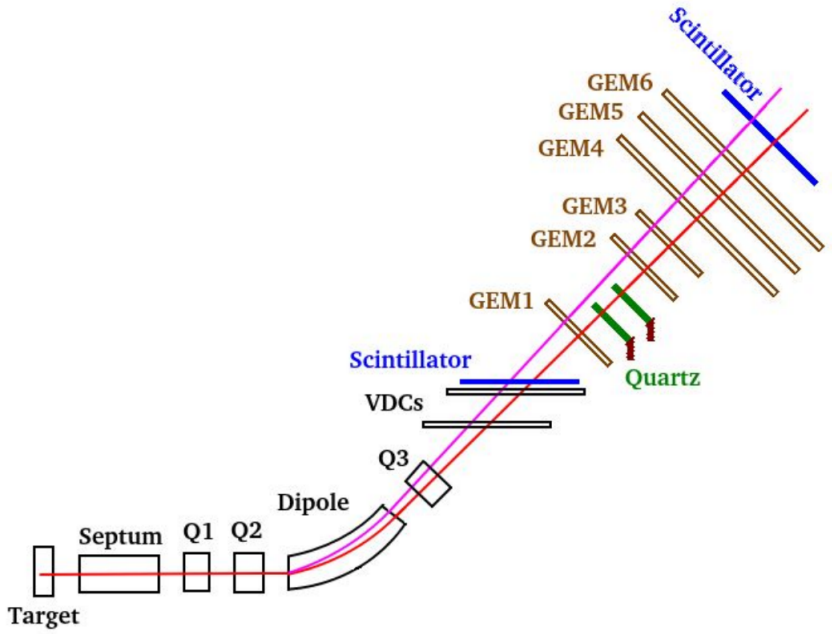

3.8.1 Main Detectors

The main detectors are thin quartz bars wrapped in mylar to prevent light leaks. The quartz bars measure 3.5 x 16 x 0.5 cm. Each spectrometer has two of these bars positioned parallel to each other at different distances from the target, referred to as the upstream and downstream detectors respectively. Thin quartz is used to reduce the amount of light yield per electron so a higher electron flux can be received. The bars can be tilted by a set of

motors at their base, and can be moved horizontally on a set of rails seen in Figure 3.21. The free movement of the detectors allowed them to be adjusted in response to data, ensuring they were properly positioned to avoid the inelastic scattering path. The alignment of the detectors was done with a devoted run during the commissioning of lead and calcium targets. Electrons passing through the quartz undergo Cerenkov radiation, shedding photons in the process. Due to the angle of the emitted photons, they are reflected down the inner walls of the quartz, and are collected in a photomultiplier tube (PMT).

Along with the upstream and downstream bars, each spectrometer included a dedicated transverse asymmetry (A_T) detector of a similar movable thin quartz and PMT design, but measuring 3.5 x 10 x 0.5 cm. The A_T detectors were placed in locations where asymmetries from transversely polarized scattering would be maximized. By placing the detectors above and below the central scattering angle as shown in Figure 3.20, the A_T detectors were sensitive to residual horizontal polarization at the target. This allowed for a constant measure of the false asymmetry resulting from residual transverse polarization.

Significant effort was made to ensure the main detectors maintained a linear response to the electron flux and corresponding light yield. While PMT's become nonlinear at both low and high flux, high flux was the main concern in this case. Prior to the experiment, a GEANT4 simulation was used to predict the light yield for the quartz geometry. Given the required electron counting rate for the experiment, the quartz thickness was chosen to produce a light yield that remained within the PMT's linear range. Additional tests were made to verify the linearity on an LED test stand before the detectors were installed in the hall. The result was a linearity systematic of $\sim 0.1\%$ [36].

Figure 3.20

The distribution of hits in the plane of the A_T detectors for horizontal polarization. The x and y axes are the plane aligned with the surface of the main detector, given in meters, and color indicates the sensitivity to the horizontal transverse asymmetry. The yellow and blue indicate positive and negative contributions, showing areas where the largest sensitivity to the difference exists. The red boxes indicate the positions of the two A_T detectors. Figure reproduced from Reference [35].

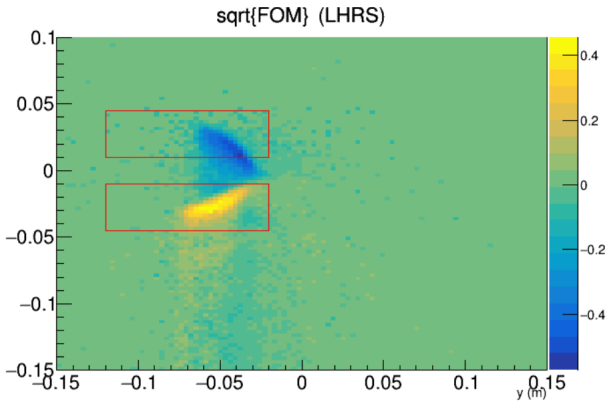

Figure 3.21

A CAD drawing of the main detector mounting and movement system. The main detectors are missing in this image. Figure reproduced from Reference [37].

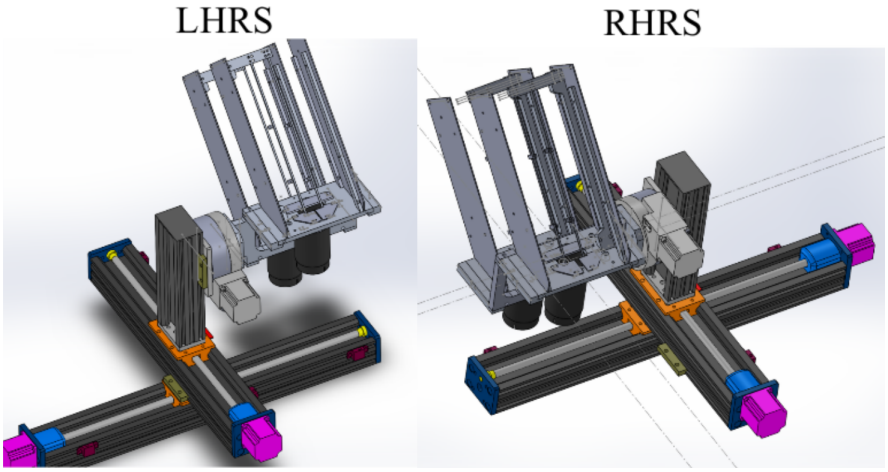

3.9 Small Angle Monitors

The small angle monitors (SAM's) are a set of eight thin quartz detectors arranged in an octagon around the beam dump. They monitor the scattered beam seven meters downstream from the target at an angle of ~0.5 degrees. They are exposed to an extremely large electron flux, making them useful for checking helicity correlated effects on a quick time scale. However, their positions at very small angles also makes them sensitive to a wide variety of beam properties that make them prone to noisy signals. The fluctuations in the beam's trajectory that cause noise in the scattering angle remain roughly the same magnitude across all angles, however, for smaller angles that associated noise represents a much larger relative contribution to the signal.

4 Data Analysis

A lot of focus is given to hardware detector systems in the experimental physics world, for obvious reasons. But due to the power of modern computers, an increasing amount of tools are software driven. The underlying, often very experiment specific, software tools are themselves as complicated as hardware, and benefit from the same physics knowledge. However, due to the accessibility of coding, it is expected that almost everybody in a collaboration is contributing in some way, making it more difficult to weigh an individual's contribution. To this end, I'll try to tabulate my contributions in Appendix B, and keep the main analysis physics focused.

4.1 Storing Asymmetry

There are many ways to conceivably store asymmetry data. It is important to retain and bundle all the information that may be needed for later analysis in a way that is both useful and easy to access. There are actually two different data acquisition (DAQ) systems in use for this experiment. The first is the counting mode DAQ, which uses the full set of scintillators in the spectrometers to collect tracking information at a low beam current. For the main measurements, a higher luminosity is needed. The higher electron flux exceeds the electronics ability to distinguish between individual electrons in time. Instead of counting individual electrons, the tracking detectors are turned off and the main detectors are switched to integrating mode, where they communicate with the integrating DAQ. However, only the integrating DAQ is used for measuring the asymmetry, while the counting mode DAQ is used for various calibration measurements.

The data for each helicity state is segmented into short time windows, called blocks, whose values are retrieved directly from hardware. During each window, a large number of device signals are recorded. This includes various info needed to interpret the signals such as error codes and hardware set points, as well as sub-block sampling of signals. The

data is saved at the end of each run in a large, multi-gigabyte data file which contains an ordered list of all the aforementioned information. This data file is read into the parity analysis engine, known as JAPAN (Just Another Parity Analyzer), which processes the raw data creating a .ROOT (from the ROOT-CERN analysis package) file so that it can be more easily used. More information on JAPAN is given in Appendix A.

In its zeroth analysis pass JAPAN reads the raw data and stores the block-wise raw data into more usable data structures, which are referred to as events. The raw data coming from the hardware is organized by the helicity event, and the sub-blocks are reported within the event structure. Each event corresponds to a set helicity state in which the polarization of the beam should remain nearly the same. At this step, the raw hardware signals are combined with any relevant device set points to make them more easily interpretable, and the sub-block results are averaged. The processing of events in this way results in better readability for analysis while still maintaining a hidden layer of valuable troubleshooting information. The length of event windows varied throughout the experiments, with the production data for PREX-II and CREX was collected at 240 Hz and 120 Hz respectively. In a similar step to the construction of the blocks, events are then grouped into sets called multiplets of eight or four events, called octets or quartets. Rather than simply alternating opposing helicity states, the helicity is flipped in irregular but symmetric patterns as shown in Figure 4.1. At the start of each multiplet, the helicity state pattern is chosen using a pseudo-random algorithm (linear-feedback shift register) based on the 30 preceding multiplets. This complicated randomization of patterns accomplishes two things; the patterns of helicity within the multiplets reduces sensitivity to 60 Hz line noise, and the longer scale randomization of multiplets cancels slower drifting noise. A systematic investigation of different length of the multiplets is given in Appendix B.11. The multiplets are used to calculate helicity based combinations in nearly real time, like the main detector's asymmetry, but for some detectors the yield or difference of states is a

more useful value. Both events and multiplets have their own error flags, but a multiplet with a bad event inside becomes a bad multiplet.

Figure 4.1

Positive and negative helicity events are combined to form patterns with an associated asymmetry.

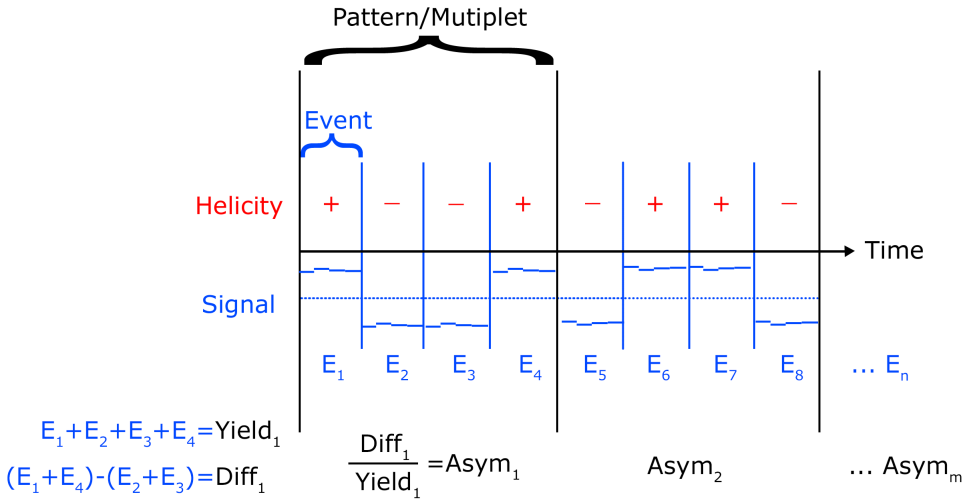

Over longer timescales, the data were segmented into miniruns, runs, and slugs. Miniruns are sets of 8000 good multiplets, which corresponds to ≈ 4.5 minutes of error free data. The choice of 8000 is somewhat arbitrary, miniruns needed just be large enough to compute regression slopes with reasonable errors. An investigation of the length of the integration window was also done. Smaller integration windows, while mostly stable, are easier to bias with periods of unstable data. Larger integration windows, on the other hand, can average out real fluctuations in sensitivities, and are impacted more frequently by the dangling miniruns at the end of runs. No significant changes were noted when sample runs were reprocessed with as few as 2000 multiplets, and as many as 12000. The

uncertainty in the sample slopes varied from ≈ 1.5% to ≈ 6% for the largest versus the smallest window. So the size of miniruns remained 8000 throughout the experiment.

Longer still were runs, which were taken at roughly one hour intervals. Runs are the time scale at which most manual configuration changes happen, as configuration files are run number delimited. The DAQ automatically split the raw data files into part files of 2 GB. The roughly one hour timing helped to keep the number of 2 GB part files per run reasonable, and allowed for reasonably fast monitoring of previous run's data.

The longest regular segmentation was the Slug, which was incremented any time the IHWP state was inverted. The IHWP state was inverted based on the amount of charge accumulated. The amount of charge per slug was chosen such that they lasted about eight hours during production running. Due to the difference beam currents, this was roughly 1.2 C on lead for PREX-II and 2 C on calcium for CREX. By accumulating the same amount of charge per slug, roughly equal statistics were taken on both half wave plate states. Big configuration changes, such as changing targets or changing settings on the Wien magnets, generally coincided with slug number changes, so the similar IHWP statistics applied to all configurations.

4.2 Asymmetry Sign Confirmation

To account for sign dependent systematic effects, the sign of the helicity is artificially inverted in a variety of ways. By taking approximately equal statistics in both sign conventions, the average serves as a null asymmetry check. The final asymmetry measurement takes into account these sign flips and corrects each one individually. The devices considered are the IHWP and Wien whose functionality are discussed in Section 3.1.1. The EPICS readouts for these devices are stored in the JAPAN .ROOT file, so the sign correction is a simple boolean check for each device multiplied by a sign.

This correction results in the entire measurement having a consistent asymmetry sign, but leaves open the question of which sign corresponds to which direction in the hall. To make this check, the polarization needs to be traced back through the accelerator using a few systems. Starting with the Moller polarimeter, which measures the longitudinal polarization asymmetry, PREX found a 'IHWP out' value resulted in a positive asymmetry. This means the polarization is aligned with the momentum. The next check is to compare the Moller DAQ and the parity DAQ to see if they have a matching convention. This was checked by intentionally creating a large charge asymmetry, and seeing if both DAQ's see the same sign. For the final check, transverse data was needed, to take advantage of its left-right asymmetry. The Mott polarimeter was used to confirm the asymmetry at the injector for vertical polarization. For vertical polarization in the hall:

$$Sgn(A) = \vec{S}_e \bullet (\vec{K}_e \times \vec{K'}_e) \tag{4.1}$$

This convention defines the left spectrometer as positive for vertical-up electrons. For PREX's transverse running, the Wien was set to vertical-down, meaning the left spectrometer should see a negative asymmetry. This was used to define the sign convention for the rest of the run.

4.3 Cuts and Corrections

If the data we got directly out of the main detector was the final asymmetry, then graduate students wouldn't have anything to do with their evenings. Alas, there are more than enough corrections required to supply everybody with jobs. There are two main ways these corrections get applied. First, there are short-scale corrections that focus on stability within runs. These corrections are often applied on the initial analysis pass, and are tweaked in subsequent passes. Second, there are corrections that apply to mean values and must be applied across many runs. These corrections often have longer and more complicated analysis whose results get applied at a later time.

4.3.1 Blinder

Since the raw data is passed through many steps of corrections on its way to the final value, the worry exists that unjustified biases may get applied in the intermediate steps. Seeing data for the asymmetry and picking options in the corrections that result in values falling closer to the model is a very hard to behavior to avoid. To stop this, the asymmetries are 'blinded' using a cryptographic technique to hide the asymmetry behind a flat blinding factor that gets added (or subtracted, for the alternate Wien and IHWP states) on to the asymmetry in the first pass of JAPAN. The blinding factor is generated using a key string, chosen before the start of the experiment. An MD5 digest is created from the string, and the digest is converted to an integer. The integer is rescaled using a ±150 ppb or ±900 ppb range for PREX-II and CREX respectively (about ten times the predicted statistical error of the main measurement), and the result is used to blind the asymmetry for each multiplet. Since the blinding factor remains constant, it can be corrected out of the final value once it is known. A checksum is used to check if the blinder is working, but without significant effort on the part of a user to calculate it, the blinding factor is unknown.

4.3.2 Beam Cuts

Beam cuts are applied to the data at the event and multiplet level and trigger error flags when they are failed. Multiplets that contain an error flagged event are still saved, but not used in subsequent asymmetry analysis. This way, the original event numbering is preserved, which is important to identifying the same event across multiple analysis passes. Some error flags are set without explicit tuning from the user. These include the following. The beam trip flag, which triggers once a set low current threshold is reached. The beam modulation flag, which triggers when the beam modulation coils are running. The hardware failure flag, which triggers when there is one of many inconsistencies in

values in the sub-blocks for a device. The blinder flag, which triggers when the blinding factor doesn't match what it should be, as described in Section 4.3.1. And lastly, the helicity flag, which triggers when there is an issue decoding the helicity state.

The remaining cuts rely on parameters that are fine tuned as part of analysis passes. These type of cut's settings are set for specific run ranges using a variety of text parameter files which are read into JAPAN. There is a default file for each type of cut, whose settings are over-written if the run being analyzed falls within an existing parameter file's run range. The type of cut and run ranges are identified using keywords in the file names using the format "cut_identifier.#-#.ext", where the two #'s are the integer run number limits. These cuts are the first defense against unintended or false asymmetries that pass through the hardware design and risk making their way into the main measurement. This section contains a brief summary of each cut type, their logic checks, and how they are used in the analysis engine. For the following sections, E_n will denote the current event's signal being checked by the cut, and n is the current event number.

4.3.2.1 Bad Event Cut

The bad event cut is the arguably the simplest cut, generally used as a last resort by a frustrated user when all other cuts fail to remove obviously bad events. As a metaphorically blunt tool, these cuts were heavily reviewed for alternative solutions. To make it past all the automatic cuts, the errors needed to leave most detector signals unchanged, yet still make events invalid for analysis. Issues with the spectrometer magnets were one of the common reasons, as changes to field strength result in nontrivial changes to the main detector acceptance. Other common reasons included occasional BPM fluctuations that survived regression and showed up in the main detector signal. This cut is defined by a numeric range of the events to be removed. The formal check is:

$$\textbf{if}(\ [[n_{min,1} \leq n]\ \wedge\ [n \leq n_{max,1}]]\ \vee\ [[n_{min,2} \leq n]\ \wedge\ [n \leq n_{max,2}]]\ \vee\ \dots\ ) \qquad (4.2)$$

where $n_{(min,i)}$ and $n_{(max,i)}$ are the range limits, which allow for i separate ranges. The event range is read from parameter files of the format "prex_bad_events.#.map".

4.3.2.2 Stability Cut

The stability cut contains a lot of the most basic options for dealing with beam fluctuations. It can set maximum and minimum values for any device in the list of monitors including BPM's, BCM's, main detectors, and even simple device combinations. This is useful, for example, by automatically removing low beam current that appears after beam trips or large positions that could hit material on the target frame. The cut also has the option to remove events which fall more than a set number of standard deviations from the mean value of that run. However, in general, the standard deviation failing events tend to fail the maximum and minimum cuts and are redundant. These settings are read from a table of device channels and their respective limits. The tables are stored in parameter files of the formats:

"prexCH_beamline_eventcuts.#-#.map"

"prexinj_beamline_eventcuts.#-#.map"

"prex_maindet_eventcuts.#-#.map"

The stability cut also provides the option to apply the set thresholds to a local rolling window of events, known as a ring, the size of which is adjustable in a parameter file of the format "prex_ring_stability.#-#.conf". When an event fails the cut, the precut and postcut settings control how many events before and after the failure are flagged, and the holdoff setting controls how many events to skip before incrementing the ring window. These values are set independently from the ring size, which allows for useful options like using using a large averaging window to cut very short spikes in the data. The formal check is:

$$\textbf{if}(\ [\min > E_n]\ \vee\ [E_n > \max]\ \vee\ [\mathrm{RMS}([E_{n-R} : E_n]) > N]\ ) \tag{4.3}$$

where min and max are the detector value limits, R is the ring size, and N is the RMS cutoff limit. When this check is true, all events in the range [n−precut:n+postcut] are flagged, and no subsequent events are marked as bad until ($n_{new} > n$+holdoff). The stability cut was effective at providing errors when detectors drifted into unacceptable ranges for parity quality beam, but it can struggle to recognize very fast shifts from stability if the signal returns quick enough. A need to recognize these signals prompted the creation of the Burp cut.

4.3.2.3 Burp Cut

The burp cut was designed with similar capabilities to the stability cut, but focused on single event fluctuations rather than ring mean values. Like the stability cut, it uses a ring, but instead of placing limits on the RMS of the ring, the limits are placed on each new events distance from the ring mean. The formal check is:

$$\textbf{if}(\ |E_n - \text{Mean}([E_{n-R} : E_n])| > B\ ) \tag{4.4}$$

where B is the burp threshold. Also like the stability cut, when this check is true, all events in the range [n−precut:n+postcut] are flagged, and no subsequent events are marked bad until ($n_{new} > n$+holdoff). The burp cut uses own values for the ring size, precut, postcut, and holdoff, as it is generally set to much smaller time scales than the stability cut. The ring values are set in a parameter file of the format ”prex.conf”, while the detector thresholds are set in the same mapfiles as the stability cut:

“prexCH_beamline_eventcuts.#-#.map”

“prexinj_beamline_eventcuts.#-#.map”

“prex_maindet_eventcuts.#-#.map”

In practice, the burp cut proved very difficult to use long term. It is easy enough to tweak into cutting specific spikes out of a problem run, but requires fine tuning to avoid triggering on natural statistical jumps. A slight change in the background noise on a

detector could cause a tight burp cut to flag data nonstop. At some point, it makes more sense to manually set bad event ranges rather than spending time tweaking a burp cut that may not work on the next run. For these reasons, the burp cut was only enabled on particularly reliable detectors, and in specific run periods where it was set up for targeted issues. Figure 4.2 shows an example burp cut configured to trim events near current ramps.

Figure 4.2

A test of a burp cut applied to the downstream BCM, configured to remove events between beam current ramps. The y axis is beam current and the x is event number, showing the current changes in time. Events marked in red are removed by the cut.

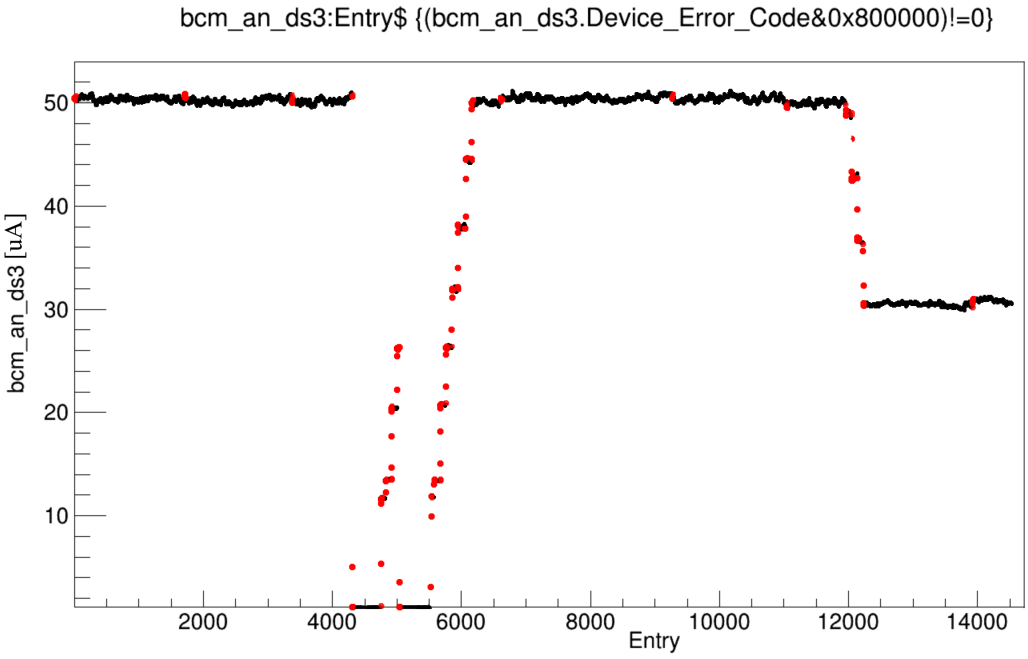

4.3.3 Pedestal Corrections

When any of the various detectors are powered on and primed for some kind of input signal, they each have their own baseline electronic offset. These offsets are called detector pedestals. In the simplest form, the measured signal can be written as a the combination of the pedestal and input:

$$S_{Meas} = S_{In} + S_{Ped} \tag{4.5}$$

Since the pedestals are basic properties of the electronics, they are not helicity dependent. If uncorrected, they would appear in the asymmetry as:

$$A_{Det} = \frac{S_{In,+} - S_{In,-}}{S_{In,+} + S_{In,-} + 2S_{Ped}} \tag{4.6}$$

To compensate for this effect, pedestals are subtracted out of the raw device signals in the first pass of analysis.

To find the pedestal of a device, a current scan can be done in which the beam current is ramped up in regular steps to span the range expected for the detectors. A linear fit then provides the zero current offset for the device. However, this method assumes all the devices are linear, which is not always the case across their whole range. Instead of fitting each detector directly to the current ramp, the following method is used.

First, a modified current ramp is performed, as shown in Figure 4.3. The short periods of beam off function as mini pedestals for each nearby step in the ramp. The Unser signal is then fit to each step, with the local pedestals removed. The Unser is used as the first step because it is linear by design, but it is noisy and suffers from a pedestal that drifts. The on-off current calibration minimizes the effects of the Unser's drift. Next, one BCM is fit to the calibrated Unser using only the beam on portion of the data. Since the Unser has a known linearity, only the current range where the two have a linear relationship is used for the fit, thereby ensuring a cleaner extrapolation of the pedestal. This BCM becomes the

normalizer, used to calibrate the rest of the detectors, as well as serving as the reference for the measured charge asymmetry.

Figure 4.3

A diagram showing the intentional beam current toggling used in an Unser current calibration run. The y axis is again beam current, and the x axis is time. Figure reproduced from Reference [38].

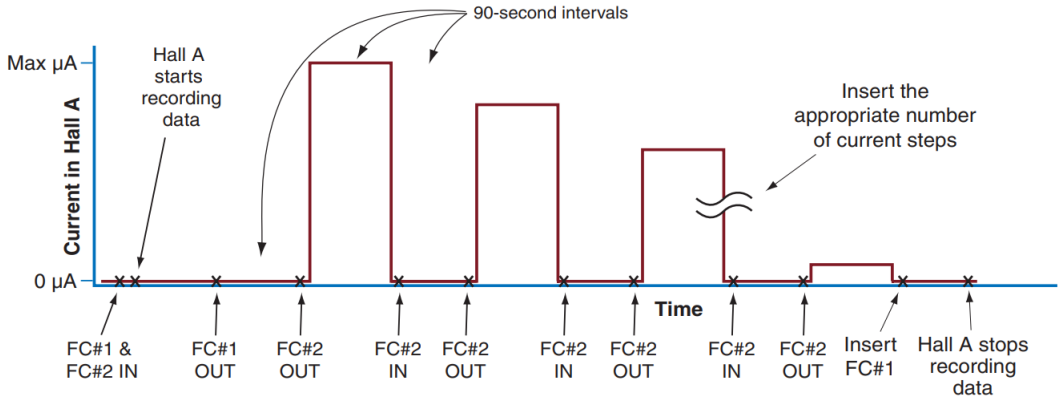

The linear fits also provide the gain of the BCM's, as each device has a unique response to current that can fluctuate over time. Device pedestals also drift over time and can shift in response to configuration changes. To account for this, pedestal calibrations and gains were updated regularly throughout the experiment, the results of which are stored in parameter files of the formats:

"prexCH_beamline_pedestal.#-#.map"

"prexinj_beamline_pedestal.#-#.map"

"prex_maindet_pedestal.#-#.map"

"prex_sam_pedestal.#-#.map".

4.3.4 Beam Corrections

In an ideal world, the experiment would use a infinitely thin beam that did not move or change any of its properties with the changing helicity. However, in practice the beam has a finite size, shape, position, and intensity. All of these properties shift slightly over time, and therefore have the possibility of affecting the measured asymmetry. Since these fluctuations can not be wholly prevented, the next best solution is to correct for their effects.

In general the beam corrections process can be broken down into a few parts. First, choosing a set of detectors which are sensitive to the aforementioned beam properties, but are also minimally correlated to each other. Second, modeling how those detector's sensitivities affect the main detector signal. Finally, using those models to correct out the predicted false asymmetry. In practice, there are multiple ways to implement these steps, and these methods will be discussed in the following sections.

4.3.4.1 Regression

Regression is one method to account for the false asymmetries associated with beam properties. For every minirun, the set of chosen beam monitors are used in a multivariable linear regression. This follows the process described in Reference [39] and the methods for determining the means, variances, and covariances in one pass in Reference [40], but a summary is as follows.

The means, variances, and covariances, are calculated for each monitor using the recursive methods given in Reference [40]. From these, one correlation matrix is formed between all of the independent variables (the beam monitors), and another between the dependent (main detectors) and independent variables. These two correlation matrices are combined to extract the detector slopes for each monitor.

The resulting slope characterizes the main detectors' response to fluctuations at that beam monitor. These slopes are updated each minirun to capture time dependent changes in the accelerator that may influence the response. The stability of the regression slopes is generally good over time, as shown in Figure 4.4. On the second pass of the analysis, a correction is applied to the asymmetry from each beam monitor. The resulting asymmetry is the expected result if the beam had been perfectly centered at each monitor. Figure 4.5 is an example of the single parameter correlation of the detector asymmetry to the position difference, and the extracted slope. In practice the slopes were calculated without graphical tools, this figure came from checks that the ROOT TGraph fits were able to identically reproduce the extracted slopes.

While the regression analysis can be performed on any beam monitor, some devices are more significant to the final asymmetry than others. While one would expect this to produce a stronger and therefore more reliable correction, this is not always the case. If devices are too correlated to each other, the corrections cancel or become redundant and certainty of the final correction is reduced. To avoid this issue, CREX applied regression to combinations of beam monitors designed to minimize the correlation between monitors. These virtual orthogonal devices, made up of weighted combinations of real monitors, are referred to as EvMons. The calculation of the weight factors is done by diagonalizing the covariance matrix of the beam monitors, where the associated eigenvectors become the EvMons [41].

Figure 4.4

The regression slopes (the fourth BPM's X coordinate versus main detector double difference) over time for the CREX lead target. Each point is the mean and uncertainty of a fit for one minirun like the one shown in Figure 4.5. Larger slopes mean position changes at this BPM would cause significant effects to the asymmetry.

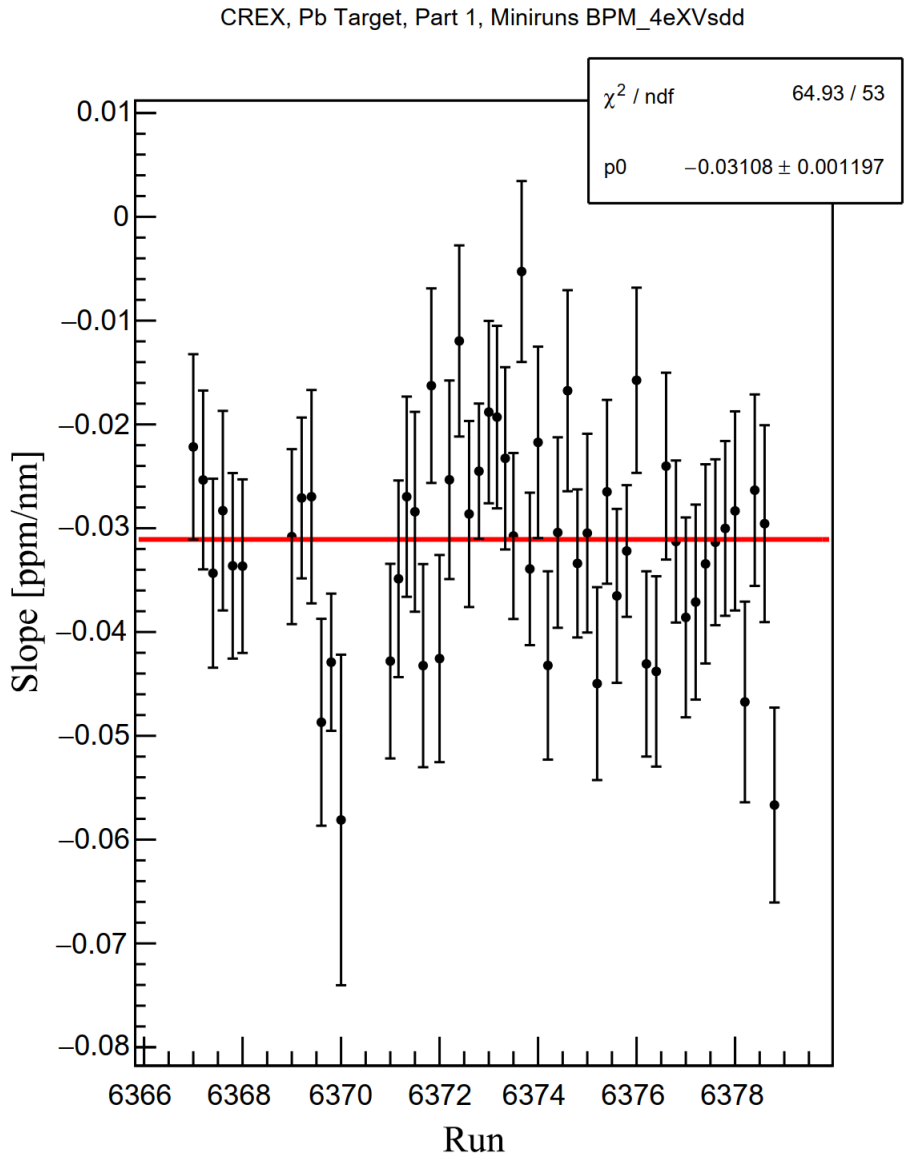

Figure 4.5

The regression slope check for a single minirun. The y values are the beam position's horizontal displacement for each event, and the x values are the main detector asymmetry. Specifically, the BPM4eX (the fourth BPM's X coordinate) slope with respect to the upstream average corresponds to the p1 fit parameter.

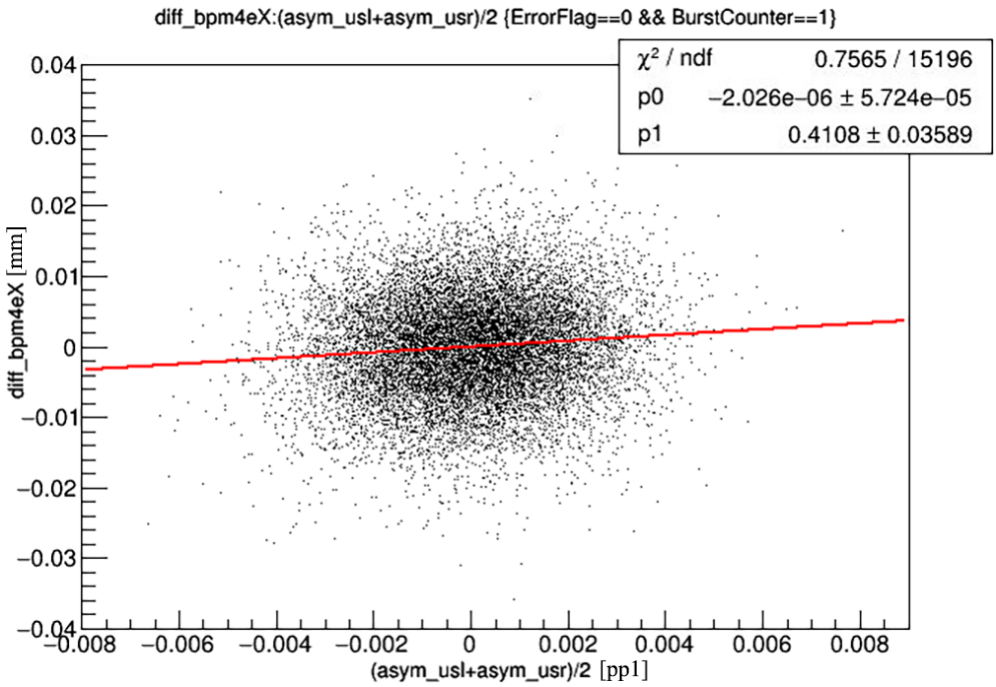

4.3.4.2 Dithering

Dithering, or beam modulation, also aims to find the sensitivity of the main detector to changes in the beam position. However, dithering uses a different set of methods to achieve that result.

Dithering uses devoted sets of air-core magnets which are installed in the beam line to shift the beam's position at 15 Hz. By forcing the beam position to shift a large amount, the fits more reliably cover the whole model space. By using multiple sets of coils positioned at different parts of the beam line, dithering can also better decouple the beam

monitors from each other. The dithering cycles were done in short bursts at about 10 minute intervals throughout the running of the experiment, and the sensitivities were calculated for each cycle. The cycles were then averaged over each slug for later analysis passes.

Calculating the dithering slopes requires additional steps when compared to regression, as the coil signal becomes a key part of the calculation. Rather than just comparing beam monitor signals to the main detector, dithering calculates both the beam monitor and the main detector sensitivities to the coil drive signal. The sensitivities could then be used to calculate a monitor versus main detector slope similar to that of regression. The results of the dithering analysis were saved as .root files which are used as inputs in JAPAN's corrections.

4.4 Uncertainty Analysis

For precision measurements like CREX and PREX, much of the effort to remove uncertainty is designed in. But despite that effort, sources of uncertainty are unavoidable. Great care is placed in understanding the sources we can not remove to make sure reasonable limits are defined on their scope. The transverse asymmetry has largely the same sources of uncertainty as the main experiment. The main difference stems from the fact that the transverse asymmetry is significantly larger in magnitude, allowing some smaller sources of error to be bounded with little additional scrutiny.

4.4.1 Regression Versus Dithering

Because regression and dithering measure what should be the same quantities using different methods, comparing the two can be useful. Differences in the extracted slopes can be treated as a measurement of the systematic uncertainty in the beam corrections. In practice, the two outputs take some additional analysis to compare directly.

The regression and dithering slopes are saved on different time scales. Regression slopes are stored each minirun, while dithering is only stored once per target. To compare them directly, the regression slopes are averaged per target. This doubles as a check of slope stability over time. Regression slopes actually have a high degree of stability per target as shown in Figure 4.6.

Once averaged over the same time scales, we can compare the dithering and regression slopes for matching run periods. While these slopes should ideally match, in practice some of them are much less consistent than others. Despite the apparent stability of slopes over time, dithering and regression come to very different answers for the same run periods. To explain this inconsistency, we look instead at the corrections to the final asymmetry that these slopes provide.

Figure 4.6

The regression slopes (Event monitor 0 virtual monitor versus main detector double difference) over time for the CREX lead target. EvMon0 represented the horizontal position at the target. Each point is the mean and uncertainty of a fit for one minirun like the one in Figure 4.5 The 'p0' parameter can be compared to an equivalent dithering slope. Larger slopes mean position changes at this BPM would cause significant effects to the asymmetry.

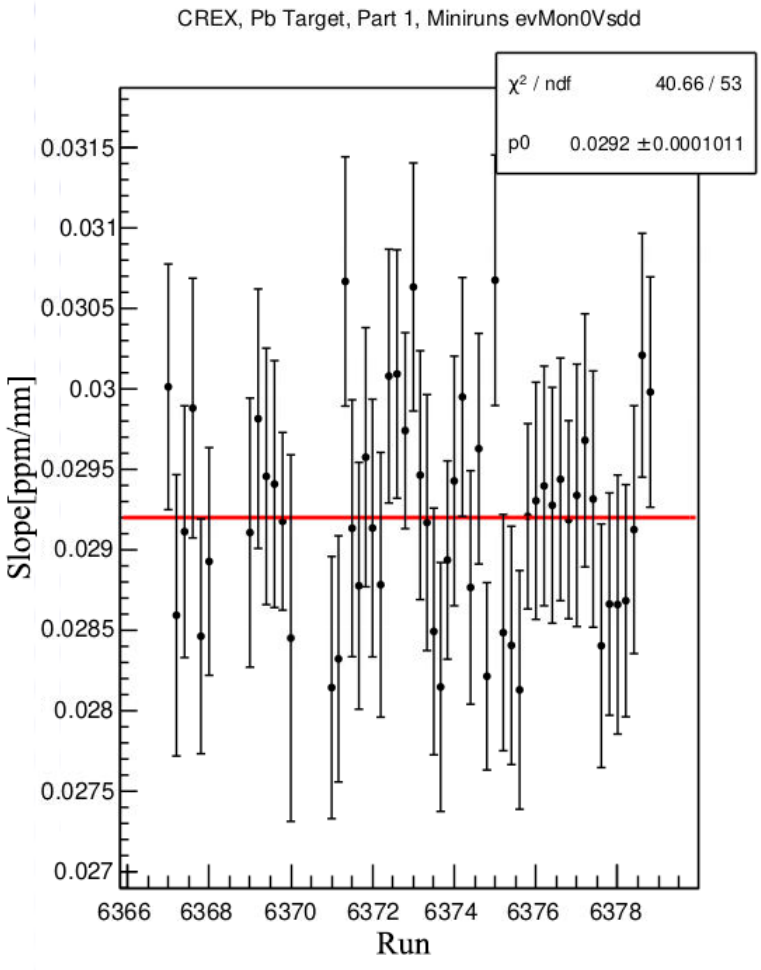

Table 4.1

The direct comparison of dithering and regression slopes for each device during each target run period. While initially alarming, the large discrepancy is explained when the corrections are calculated. The largest corrections, from EvMon0 and EvMon1, represent the sensitivity to horizontal position at the target and the beam energy. EvMon3 is the horizontal angle on target, while EvMon2 and EvMon4 are the vertical position and angle at the target. The large slopes only appear when the corresponding correction is small. Corrections given in ppb.

Target		^{48}Ca, 1	^{40}Ca, 1	^{48}Ca, 2	^{12}C, 1	^{208}Pb	^{48}Ca, 3	^{12}C, 2	^{40}Ca, 2	^{48}Ca, 4
Slope Percent Differences	EvMon0	3.2%	3.2%	3.6%	4.0%	2.3%	3.6%	3.2%	5.8%	4.7%
	EvMon1	4.3%	-2.1%	22.8%	12.6%	-2.2%	-2.7%	3.6%	7.8%	8.3%
	EvMon2	21.6%	3.7%	76.4%	-29.9%	1090.0%	85.3%	73.9%	5.7%	11.0%
	EvMon3	46.5%	43.9%	55.1%	87.4%	139.6%	113.4%	62.8%	88.2%	67.4%
	EvMon4	46.0%	87.6%	69.2%	58.8%	4.3%	31.0%	47.5%	62.7%	73.5%
Slope Corrections	EvMon0	1934	-1765	-1784	823	537	1350	615	538	-1747
	EvMon1	-48	400	404	139	77	140	-94	-303	304
	EvMon2	14	63	8	-81	-0.3	-6	3	-17	-39
	EvMon3	149	20	-6	48	4	-63	-31	35	46
	EvMon4	19	40	10	6	-24	-14	-25	20	12
Correction Percent Differences	EvMon0	2.8%	4.6%	5.0%	3.1%	2.0%	3.8%	4.6%	9.2%	5.9%
	EvMon1	-0.1%	0.7%	-7.9%	1.7%	-0.3%	-0.3%	-0.8%	-7.0%	-1.9%
	EvMon2	0.2%	-0.2%	-0.8%	1.9%	0.1%	-0.7%	0.9%	-0.3%	0.3%
	EvMon3	4.1%	-0.9%	0.4%	6.8%	3.2%	-12.9%	-6.4%	15.6%	-3.3%
	EvMon4	0.5%	-5.0%	-0.8%	0.5%	-0.2%	-0.4%	-3.4%	5.1%	-0.9%

To find the correction to the detector asymmetry from each beam monitor, we multiply the mean value of the helicity-correlated difference of the beam monitor with its slope. A comparison of the regression versus dithering slopes, and the regression versus dithering corrections is shown in Table 4.1. The direct slope comparison fails because when a beam monitor has very small position differences, then it provides very little to the final correction, and its slope means correspondingly little. This effect compensates for the slope disagreements, and results in a more meaningful comparison between regression and dithering corrections. This correlation between slope and correction size can be seen in Figure 4.7.

An inspection of Table 4.1 lead to a process for bounding the systematic error for the disagreement between regression and dithering. A flat five percent of the correction due to each monitor was chosen as bound to match the scale of the disagreement between the two. These five percent corrections for all of the detectors were added in quadrature, and then combined in an average per target, weighted by each run period's RMS. The resulting corrected asymmetries along with the statistical uncertainty is given in Table 4.8. This systematic bound is significantly smaller than the statistical uncertainties, as we have close agreement between regression and dithering.

Figure 4.7

Two sets of slopes for two monitors during the same run period. Each point is one minirun's slope and uncertainty. Larger y values indicate a larger slope, and that the asymmetry is more correlated with the detector. EvMon0 (left) set has a very large average slope, while EvMon2 (right) has a very small slope. EvMon0 and EvMon2 represent the horizontal and vertical positions at the target respectively. Table 4.1 shows the disagreement in slopes for EvMon0 is 2.3% while the disagreement for EvMon2 is 1090%.

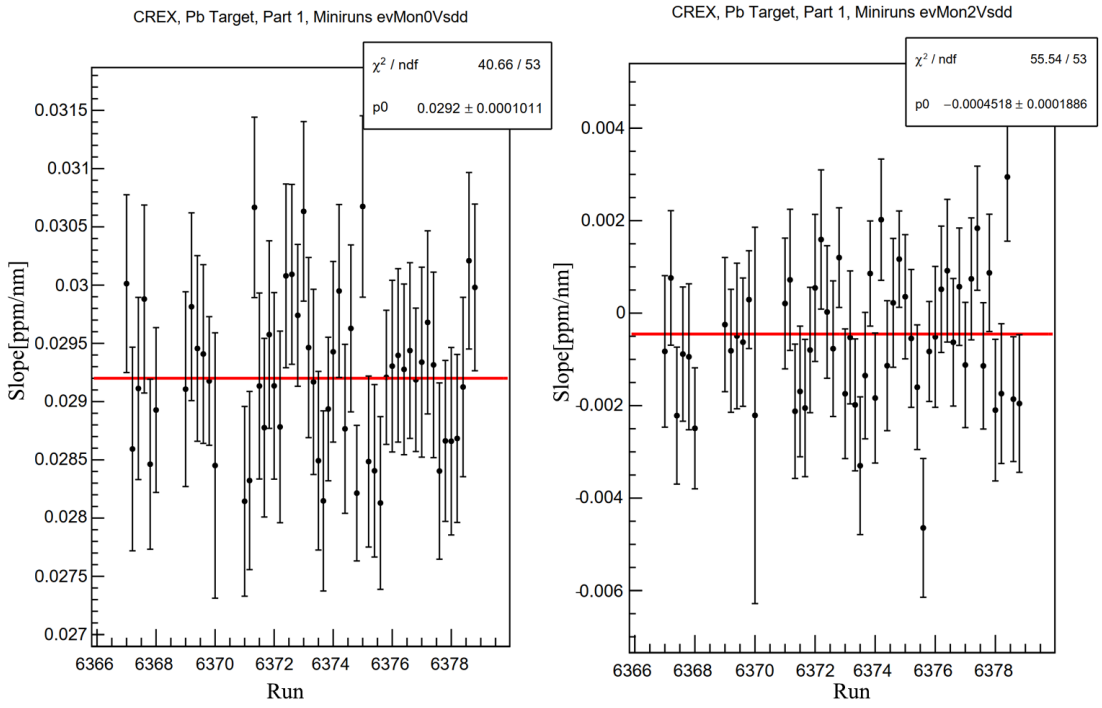

Table 4.8

The asymmetries and error contributions for beam corrections from PREX-II and CREX. $d(A_{Meas})_{Stat}$ are the statistical uncertainties and $\delta(A_{Meas})_{Sys}$ are the contributions to the systematic uncertainties coming from comparison of dithering and regression analysis. Values given in ppb.

Experiment	Target	A_{Meas}	$d(A_{Meas})_{Stat}$	$\delta(A_{Meas,Beam})_{Sys}$
PREX-II	^{12}C	-5494	330	29.4
	^{208}Pb	0.257	129	71.0
	^{40}Ca	-5295	290	42.4
CREX	^{12}C	-8167	880	37.8
	^{208}Pb	-2765	1610	27.8
	^{40}Ca	-8405	926	48.9
	^{48}Ca	-7917	839	86.7

4.5 Respins

Since the final asymmetry measurement is a mean value (sometimes it's nice too, don't worry) taken across all runs, calculating it requires processing all of the data and including corrections from a variety of sources. To minimize calculation time for live data monitoring during the experiment, only the raw values with simple or pre-calculated corrections can be used in the initial passes. Over time, these corrections need to be tweaked and reapplied. However, processing just one run worth of events on a single machine can take as long as an hour. Additionally, with each run containing a few gigabytes of data, opening more than one simultaneously can quickly exceed machine RAM limitations. For these reasons, doing the final calculation for thousands of runs on one machine quickly becomes infeasible.

To solve these issues, an installation of JAPAN was maintained on the Jefferson Lab distributed computing farm. This allowed the analysis of individual runs to be parallelized, reducing the total computation time by a factor of n, where n is the number of compute nodes. With n~200, the computation time is reduced from months to only a few hours. Mean values for runs were also extracted in stored in separate trees, allowing experiment long time scales to be viewed without the aforementioned RAM limitation. These whole-experiment analysis passes were called respins. Testing analyses on small data sets and collecting the results into a central repository before agreeing to run respins allowed the experiment to reduce the total computation time, as well as point to a standard set of checkpoints as we moved toward the final value. Some additional discussion of implementing the respins is included in Section B.8.

4.6 From Raw to Final Asymmetry

The final asymmetry is extracted from the raw value via a set of combinations and iterative corrections, each of which require their own set of analysis. A brief summary of the steps that will be discussed in this section.

In the first pass analysis of JAPAN, the detector signals are combined with their pedestals at the event level, and the multiplets are created. This removes the factor of $2S_{Ped}$ that appears in Equation 4.6, and results in the first sets of multiplets A^i_{Raw}. The error flags are also applied at this step, and any events or multiplets with errors are ignored in all of the subsequent steps. The slopes for regression are calculated in this pass, using only error free values to ensure meaningful sensitivities. Included in this step are detector combinations, specifically the main detector average asymmetries and 'double differences', given by:

$$A^i_{Avg} = \frac{A^i_{LHRS} + A^i_{RHRS}}{2} \quad \text{, and} \quad A^i_{DD} = \frac{A^i_{LHRS} - A^i_{RHRS}}{2} \tag{4.7}$$

The parity violating measurement uses the average to calculate A_{PV}, while the transverse measurement uses the double difference to calculate A_T. This is because the parity violating case is measuring in total rate as a function of spin, while the transverse case is measuring an azimuthal dependence. As this document focuses on A_T, for the rest of the discussion in this section $A^i_{Raw} = A^i_{DD}$. The raw asymmetry averages as well as their statistical errors are given in Table 4.2. A second pass is then used to apply the regression and dithering slopes, to correct the previously built multiplets and combinations. This pass results in the beam corrected asymmetries $A^i_{Meas} = A^i_{Raw} - A^i_{Beam}$, as well as the corrected minirun and run scale values such as the mean, RMS, and error for the corrected asymmetries. The values of A_{Meas} are the same as those discussed in Section 4.4.1. The regression and dithering corrections are saved as separate trees for each time scale, and either outputs can be used for the following steps.

Table 4.2

The raw transverse asymmetry double differences per target and their associated statistical uncertainties. The statistical uncertainties, $d(A_{Raw})_{Stat}$, are the combined errors on the means for all A^i_{Raw} collected on a given target. All values given in ppb.

Target	A_{Raw}	$d(A_{Raw})_{Stat}$
^{12}C	-7614	1040
^{208}Pb	-2414	1741
^{40}Ca	-8363	1198
^{48}Ca	-7784	1075

The corrected miniruns are combined using an error weighted average across matching targets. At this step, the sign corrections from the slow spin controls are applied. The resulting asymmetry average is given by:

$$A_{Meas} = \frac{\sum_m A^m_{Meas} \times \mathrm{Sgn} \times \sigma_m^{-2}}{\sum_m \sigma_m^{-2}} \tag{4.8}$$

Where A^m_{Meas} are regression or dither corrected miniruns, Sgn is a function that applies a sign based on the known settings of the slow controls system, and σ_m are the uncertainties on each minirun. Subsequent corrections apply to these target averaged values. The beam corrected asymmetries and the associated uncertainties are given in Table 4.3. Also included in the table are the main detector linearity systematics, which are also calculated using the values of A_{Meas}.

The calcium 48 and lead targets both contain dilution from other elements at a significant rate. In the case of calcium 48, this comes from isotopic impurities, namely some amount of calcium 40. In the case of lead, this comes from the carbon in the diamond foils. To account for this, each contaminant's asymmetry is subtracted from the main asymmetry, weighted by the its concentration in the target. The result is a corrected

Table 4.3

The beam corrected asymmetries per target and their associated uncertainties. The statistical uncertainties, $d(A_{Meas})_{Stat}$, are the combined RMS for all A^i_{Meas} collected on a given target. These shrink significantly due to the reduction of beam related fluctuations as compared to the values of $d(A_{Raw})_{Stat}$ given in Table 4.2. $\delta(A_{Meas,beam})$ and $\delta(A_{Meas,nonlin})$ are the contributions to the systematic error due to beam corrections and detector non-linearities. The full discussion of $\delta(A_{Meas,beam})$ is given in Section 4.4.1. All values given in ppb.

Target	A_{Meas}	$d(A_{Meas})_{Stat}$	$\delta(A_{Meas,beam})_{Sys}$	$\delta(A_{Meas,nonlin})_{Sys}$
^{12}C	-8167	880	37.8	38
^{208}Pb	-2765	1610	27.8	12
^{40}Ca	-8405	926	48.9	42
^{48}Ca	-7917	839	86.7	39

pure target asymmetry given by:

$$A_{Corr} = \frac{A_{Meas} - \sum_i f_i A_i}{1 - \sum_i f_i} \tag{4.9}$$

Where A_i is the asymmetry of the contaminating source, and f_i is the effective atomic fraction of the source. For calcium, f_i is taken from the assay performed by the lab that produced the target. For lead, f_i is calculated using the known diamond window thickness. The corrections for lead and calcium 48 use the measured asymmetries of carbon and calcium 40 for A_i respectively. The correction to lead is very large, as the carbon asymmetry produced by the diamond foils has a larger strength than the lead. Additionally, the uncertainties in the lead correction are compounded with the uncertainties in the carbon measurement. The values of f_i are given in with the resulting corrections in Table 4.4.

Table 4.4

The dilution factor corrected asymmetries per target and their associated uncertainties. The statistical uncertainties, $d(A_{Corr})_{Stat}$, are now the values of $d(A_{Meas})_{Stat}$ from Table 4.3 weighted by their respective dilution factors and combined in quadrature. The increase in the statistical uncertainty in lead compared to Table 4.3 is due to the combined contributions of the statistical error from lead and carbon. $\delta(A_i)_{Sys}$, $\delta(f_i)_{Sys}$, and δ(Inel.)$_{Sys}$ are the contributions to the systematic error from the uncertainty on the asymmetry used in the dilution calculations, the uncertainty on the atomic fraction, and the uncertainty on the inelastic calculation respectively. Note that these values of $\delta(A_i)_{Sys}$, $\delta(f_i)_{Sys}$, and δ(Inel.)$_{Sys}$ are already scaled by Equation 4.10. All values given in ppb.

Target	f	δ(f)	A_{Corr}	$d(A_{Corr})_{Stat}$	$\delta(A_i)_{Sys}$	$\delta(f_i)_{Sys}$	δ(Inel.)$_{Sys}$
^{12}C	0	0	-8167	880	0	0	76
^{208}Pb	0.6089	0.0609	523	2646	637	391	4
^{40}Ca	0	0	-8405	926	0	0	146
^{48}Ca	0.0907	0.0018	-7873	919	100	1	80

Table 4.4 also includes a systematic contribution that bounds the contribution from inelastic scattering in the target. It needs to be applied in the same form as Equation 4.9, with A_i representing asymmetries due to individual inelastic states, and f_i representing the amount of that state accepted in the main detector. These values are calculated using a GEANT4 simulation of the experimental geometry that provides an estimated rate for the first few excited states at the main detector [35].

The last step combines two corrections to arrive at the final asymmetry:

$$A_n = \frac{A_{Corr}}{P_n < \cos\phi >} \tag{4.10}$$

where P_n is the polarization magnitude as measured by the Compton and Moller polarimeters. The CREX transverse asymmetry measurement used the average of the two

polarimeters result, $P_n = 86.78\% \pm 0.62$. Here $< \cos\phi >$ is a scale factor that accounts for the fact that the left and right spectrometer's acceptance in ϕ aren't exactly aligned to the horizontal, as well as any asymmetric effects related to the finite range of ϕ values covered by the detectors. This quantity is extracted along with $< Q^2 >$ using a combination of sieve tracking data and simulation known as the acceptance function. This function is the relative probability for a particle of given trajectory to make it to the target. When convolved with the cross section and the measured distribution of a variable at the detector, shown below for $< Q^2 >$, it provides a realistically weighted mean value for kinematically dependent variables of uncertainty $< 1\%$ as reported in Reference [42].

$$< Q^2 >= \frac{\int Q^2(\theta)\frac{d\sigma}{d\Omega}\epsilon(\theta)\sin\theta d\theta}{\int \frac{d\sigma}{d\Omega}\epsilon(\theta)\sin\theta d\theta} \tag{4.11}$$

The final values for A_n after the acceptance correction are given in Table 4.5. The partial contributions to the systematic uncertainty are summed in quadrature from the previous steps to get $\delta(A_n)_{Sys}$. The final systematic uncertainty can be written in terms of the variables defined in this section as:

$$\delta(A_n)_{Sys} = \sqrt{\left(\frac{\delta(A_{Beam})}{P_n < \cos\phi >}\right)^2 + \left(\frac{\delta(A_{Nonlin})}{P_n < \cos\phi >}\right)^2 + \delta(A_i)^2 + \delta(f_i)^2 + \delta(P_n)^2 + \delta(Inel.)^2} \tag{4.12}$$

Table 4.5

The acceptance corrected asymmetries per target and their associated uncertainties. The statistical uncertainties, $d(A_n)_{Stat}$, are the values of $d(A_{Corr})_{Stat}$ from Table 4.4 combined in quadrature with the uncertainty in the polarization. $\delta(A_n)_{Sys}$ is defined by equation 4.12. All values given in ppb.

Target	$< \cos\phi >$	A_n	$d(A_n)_{Stat}$	$\delta(A_n)_{Sys}$
^{12}C	0.969	-9715	1049	128
^{208}Pb	0.969	622	3146	748
^{40}Ca	0.970	-9984	1102	184
^{48}Ca	0.970	-9353	1094	187

5 Results and Conclusions

The final transverse asymmetries and their associated uncertainties as measured by CREX are given in Table 5.1. The total uncertainty is a simple quadrature sum of the statistical and systematic results. These values are discussed in the following sections.

Table 5.1

Final transverse asymmetry values measured during CREX and their associated statistical and systematic uncertainties. The total error is the quadrature sum of the statistical and systematic errors. Given in ppm.

Target	$< Q^2 >$(GeV^2)	A_n(ppm)	Stat.(ppm)	Sys.(ppm)	Tot.(ppm)
^{12}C	0.033	-9.7	1.05	0.13	1.05
^{208}Pb	0.031	0.6	3.15	0.75	3.23
^{40}Ca	0.030	-10.0	1.10	0.18	1.11
^{48}Ca	0.030	-9.4	1.09	0.19	1.11

5.1 Comparison to Existing Data

To compare the values listed in Table 5.1 to those of existing experiments, they are plotted as a function of their measured Q. Figure 5.1 shows the CREX values compared to those of PREX and PREX-II compared to their most recent model curves [15]. These are the most directly comparable existing measurements, as they share similar kinematics and uncertainties. We can see immediately the so-called 'PREX problem', namely the large mismatch between the model prediction and experimental result for lead nuclei. The experimental lead points are all consistent with zero, across a range of Q. Despite the dip in predicted A_n and CREX's larger statistical error, the new lead measurement still shows a multiple sigma disagreement.

The under-prediction of calcium and carbon in PREX-II is less significant in the CREX data, and only calcium 40 appears outside of uncertainty range. On the topic of isotopic dependence, CREX measurements show the two isotopes of calcium are consistent within uncertainty. The CREX measurement indicates no dependence of A_n with respect to neutron number. More isotopic measurements are needed to investigate this issue.

Figure 5.1

A snapshot of recent transverse asymmetry measurements including PREX [43], PREX-II, and CREX [42]. The most up to date model calculation curves from Reference [15] are also displayed in matching colors. NOTE: The PREX-II calcium and carbon points have been horizontally shifted slightly as to not cover each other.

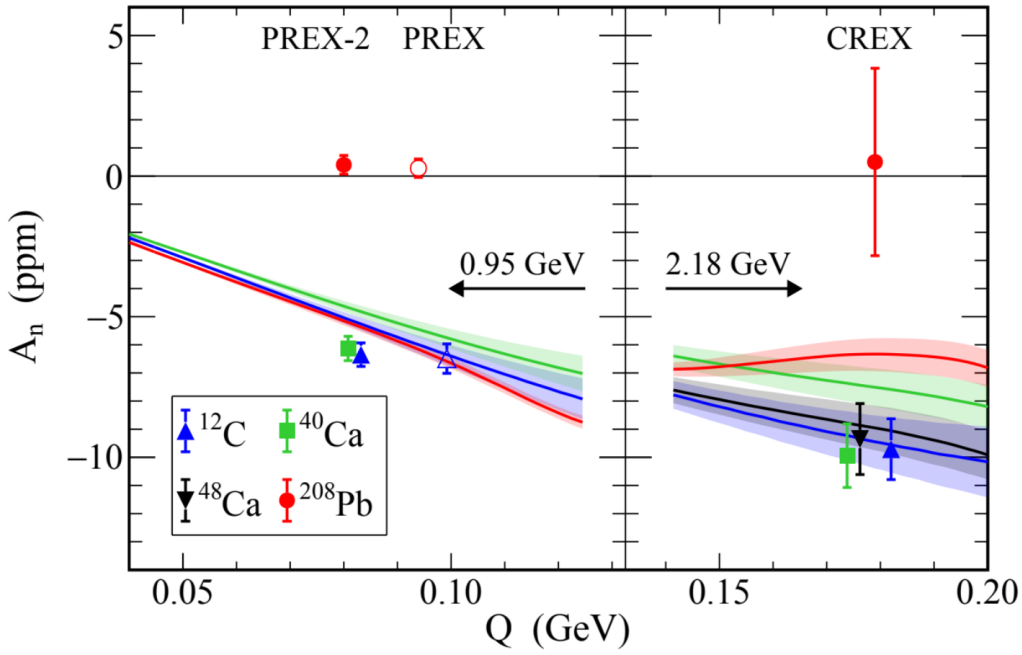

Comparing other transverse asymmetry measurements presents additional issues, as kinematics play a heavy part in model predictions. The functional form of A_n depends non-trivially on the lab beam energy, Q^2, scattering angle, and properties of the nucleus

itself including its mass, charge, and form factor. In Reference [15], Koshchii and Gorchtien have produced model curves for a list of recent experiments at other kinematics including QWEAK [44, 45], MAMI [46, 47], and HAPPEX [43]. While these models provide a basis to compare CREX to other experiments, the authors are clear that the models use an assumption of high beam energy in the Compton scattering inputs which may not be reasonable to extend to all of these kinematics. This is evident in the comparison of data on carbon, shown in Figure 5.2, which is available for a wide range of beam energies. The models have a tendency to underpredict the asymmetry in carbon at lower beam energies, but have correct scaling across Q^2 for higher energy beams. With the exception of lead, these predictions match data for a variety of nuclei (^{4}He, ^{12}C, ^{27}Al, ^{40}Ca, ^{48}Ca, ^{208}Pb) provided $E_b > \approx 1$ GeV. The two additional intermediate mass nuceli (^{28}Al, ^{90}Zr) measured by MAMI [47], are both underpredicted as well, likely due to their lower beam energy.

Figure 5.2

A comparison of carbon transverse asymmetry measurements for QWEAK [45], MAMI [46, 47], PREX [43], PREX-II, and CREX [42] compared to their theoretical predictions from Reference [15]. The QWEAK, CREX, and PREX points are in reasonable agreement with the theory bands, but the MAMI points show significant disagreement.

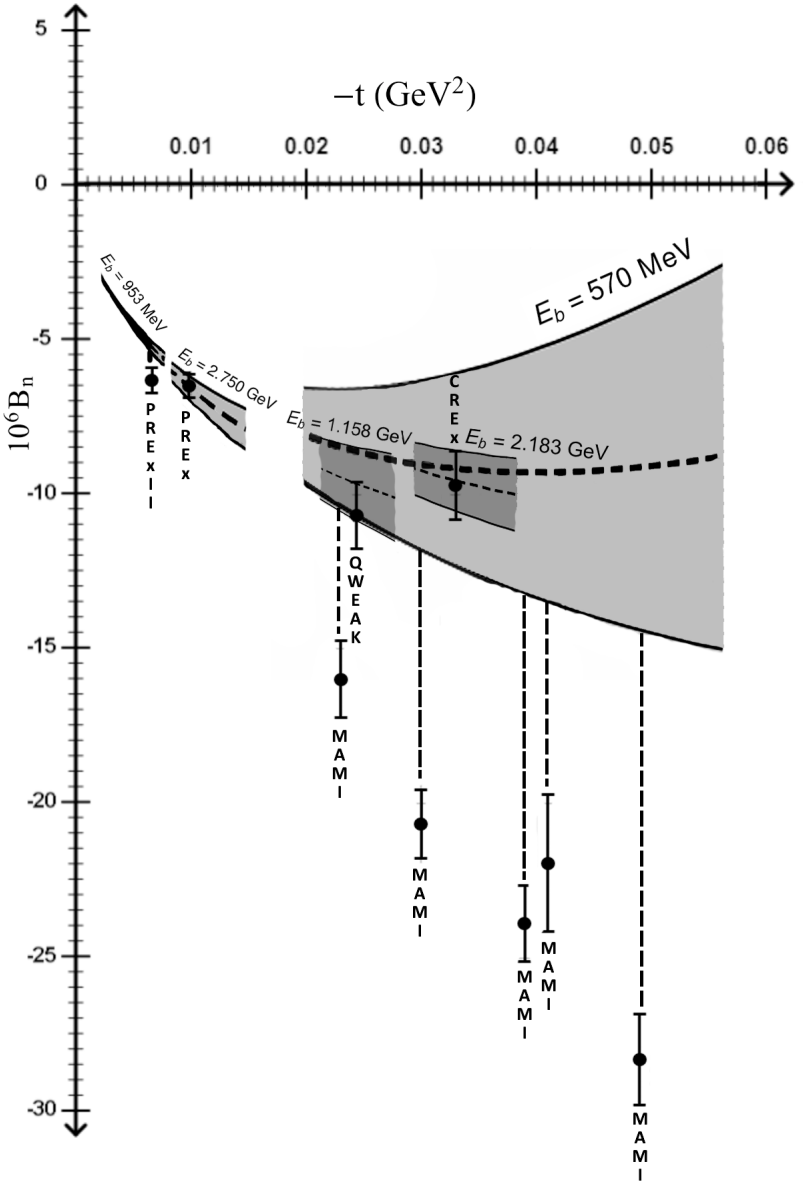

5.2 Implications

The complicated disagreement between models and data seems to boil down to two main concerns. The first is the energy dependence of lower beam energy asymmetries. The second is the aforementioned "PREX problem." A possible solution to the "PREX problem" is suppression due to a vertex correction on the nucleus due to the Feynman diagram shown in Figure 5.3. This process is a first order correction to the two photon exchange process, so it should scale as $\approx Z^2\alpha$.

An estimation of this correction's effects on current models can be made using the form:

$$A_n \approx A_0(Q^2)(1 - CZ^2\alpha) \tag{5.1}$$

Where A_0 is a current model that doesn't include this suppression, and $C \approx 0.02$ is a constant set such that BNSSA data for lead matches predictions, but intermediate nuclei are affected as little as possible. Phenomenologically, this fit does very well. As shown in Table 5.2, it provides nearly no corrections on light nuclei $Z \leq 20$, small corrections that remain consistent with data for $20 \leq Z \leq 50$, and a very large correction for lead at $Z \geq 50$.

Table 5.2

The suppression of heavy nuclei due to the vertex correction inspired equation 5.1.

Target	αZ^2 Correction
^{12}C	1%
^{27}Al	2%
^{28}Si	3%
^{40}Ca	6%
^{48}Ca	6%
^{90}Zr	25%
^{208}Pb	98%

Figure 5.3

The Feynman diagram for a radiative correction in which the nucleus exchanges a photon with itself during a two photon exchange scattering event.

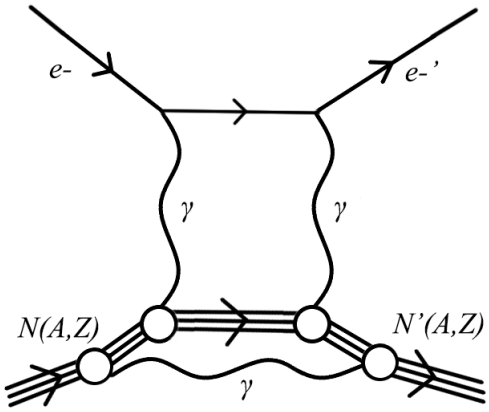

5.3 Beam Energy Scaling of A_n

The issue of modeling the transverse asymmetries at lower energy is clear in the 0.57 GeV beam energy data from MAMI, shown in Figure 5.4. Across all three nuclei, the asymmetry is underpredicted. It is possible this is an effect of MAMI's larger scattering angle, but this discussion will focus on energy for reasons that will be discussed in this section. Interestingly, PREX-II at 0.95 GeV also found the models underpredicted carbon, and calcium 40, shown in Figure 5.5. Since the models provide a good prediction for carbon asymmetries at beam energies > 1 GeV at a variety of Q^2, it suggests that the energy is a factor in suppressing it. Quoting the paper by Koshchii *et al.* [15]:

"We note that our framework has been designed for high-energy electron scattering; apart from lacking contributions from the nuclear range, it operates with a phenomenological t-dependence motivated by the high-energy Compton scattering data. While the high energy measurement on ^{4}He by the HAPPEX collaboration at 2.75 GeV is well described, and so is a somewhat lower one on ^{12}C at 1.063 GeV, the

Figure 5.4

All MAMI data for carbon [46], silicon, and zirconium [47] compared to their most recent model curves. Figure reproduced from Reference [15].

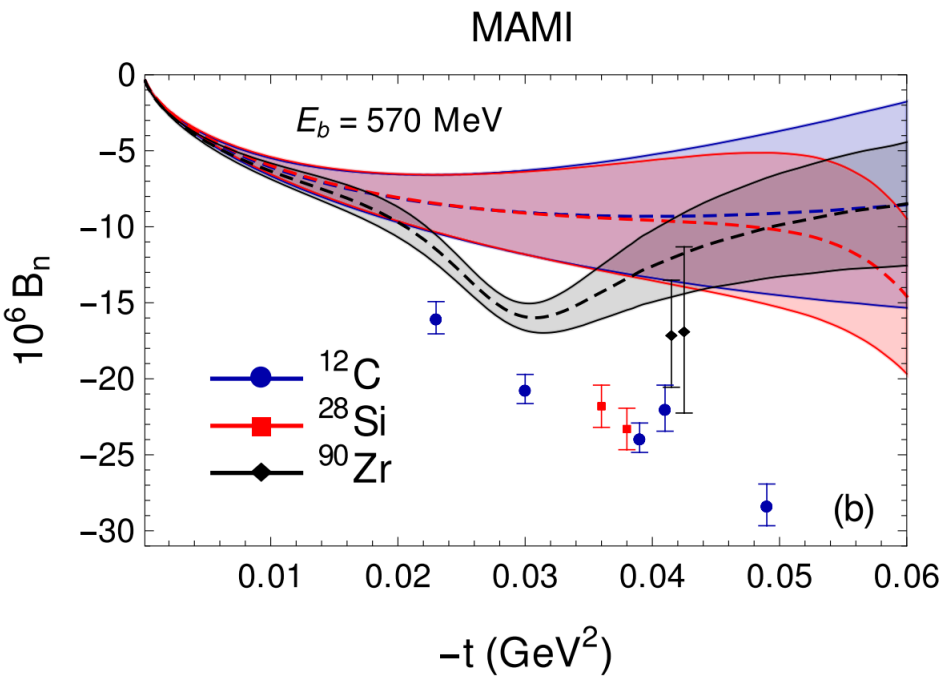

agreement at lower MAMI energies is worse even for light and intermediate nuclei. This fact indicates that the t-dependence of the Compton cross section in the resonance region is likely not to follow the exponential fall-off as deduced from high-energy data." [15]

The suspicion lies in the B parameter of the Compton form factor given by $g(Q^2) = exp(\frac{-Bt}{2})$, where $t = Q^2$. This factor is obtained in Koshchii *et al.* [15] by fitting high energy ($E_\gamma = 3,5$ GeV) Compton scattering data that exists for ^{4}Be, ^{12}C, ^{27}Al, ^{49}Ti, ^{64}Cu, ^{109}Ag, and ^{197}Au [48]. The Compton scattering data used for the fits is shown in Figure 5.6. The extracted values for B are given in Table 5.3. To use these fits in the models, an assumption is made in Koshchii et al. that the missing nuclei (^{4}He, ^{28}Si, ^{40}Ca,

Figure 5.5

PREX-II [42] data for carbon, calcium, and lead compared to their most recent model curves [15].

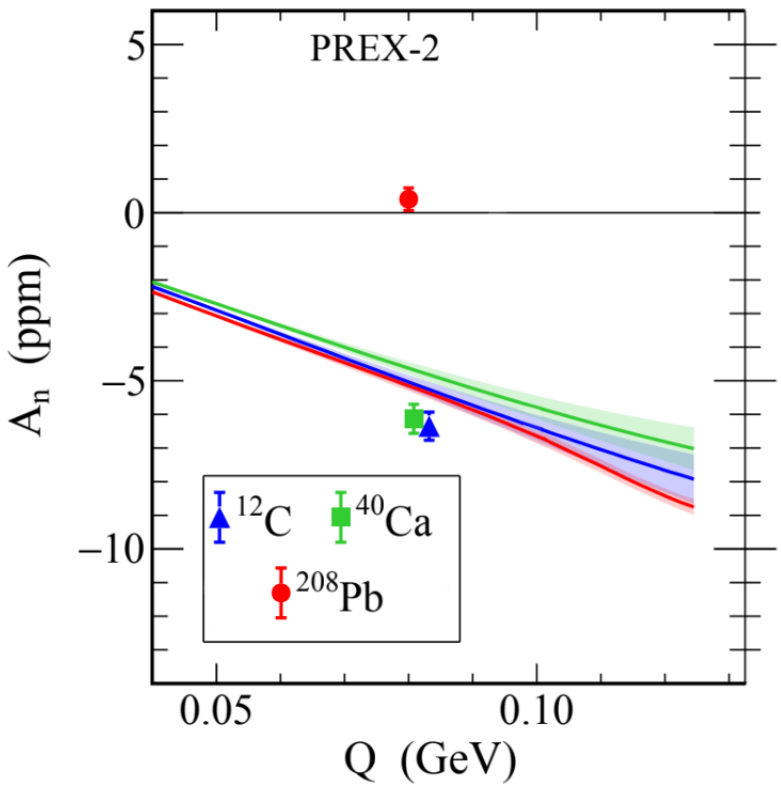

^{48}Ca, ^{90}Zr, and ^{208}Pb) will have similar factors of B as a function of A or Z (B(^{27}Al)≈B(^{28}Si)). And also that B is a constant in E_γ. Given the fact that B changes as a function of A and(or) Z and E_γ in the table, this seems like a questionable assumption.

To remedy both these issues, I propose two modifications to the fits. The first is simple; instead of assuming B changes very little in Z and using near-by elemental values, we interpolate B values across Z using a fit. In particular, since there is no obvious ansatz about the functional form, linear and quadratic fits of B(Z) were investigated. The

Figure 5.6

Cross sections as a function of t for Compton scattering on ^{4}Be, ^{12}C, ^{27}Al, ^{49}Ti, ^{64}Cu, ^{109}Ag, *and* ^{197}Au *given for* E_γ *of 3 and 5 GeV. Figure Reproduced from Reference [48].*

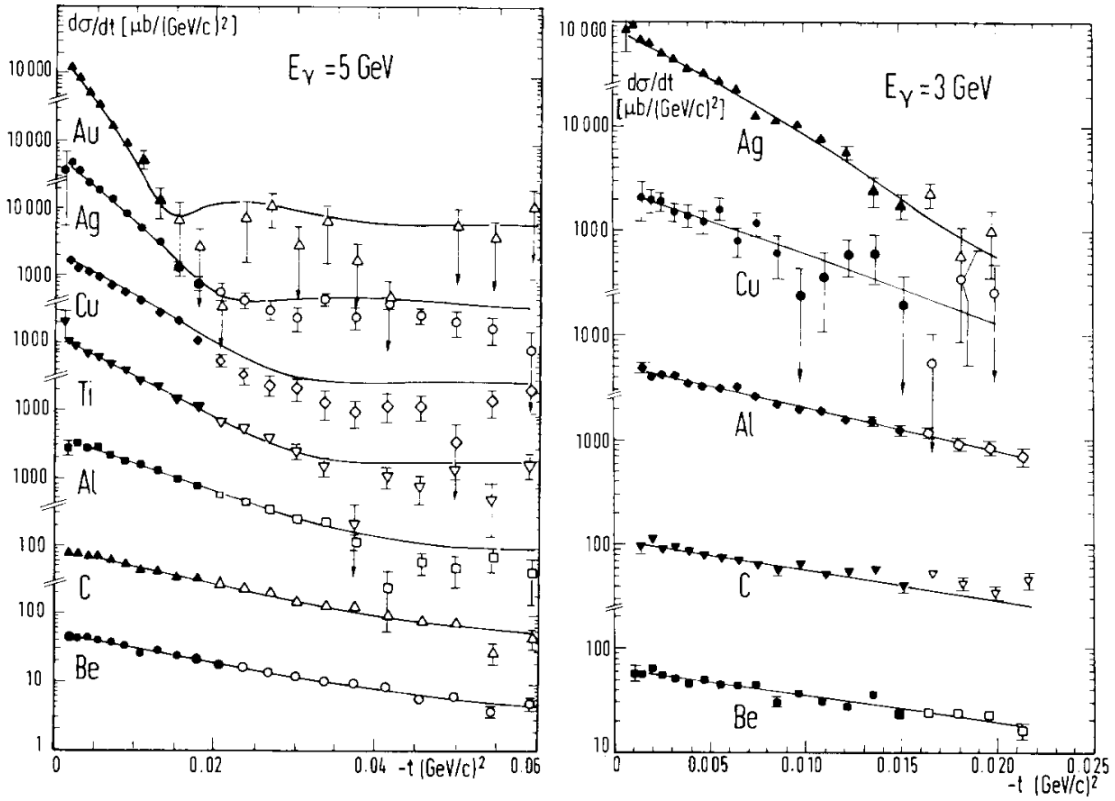

interpolation fits are shown in Figure 5.7. While the quadratic Z fits do a better job describing the existing B values, the linear fit showed slightly better performance minimizing residuals when used in combination with the corrections discussed later in this section. Despite the appeal of a linear form, the quadratic form of B(Z) was used to remain in closer agreement with the errors on Koshkii's B fits. Additionally, fits of B(A/Z) were also checked. While B(A/Z) does a better job describing the difference between the isotopes of calcium, but it was rejected due to the fact that despite its complexity it provided very little correction. The change to B(Z) compared the values used by Koshchii

Table 5.3

Values of B extracted by Koshchii et al. from fitting the functional form "$\alpha \exp(\frac{-Bt}{2}) + \sigma$" on ^{4}Be, ^{12}C, ^{27}Al, ^{49}Ti, ^{64}Cu, ^{109}Ag, and ^{197}Au given for $\omega = E_\gamma$ of 3 and 5 GeV. Table reproduced from Reference [15].

Target	$\omega \approx$ 3GeV B [GeV^{-}2]	ω =5GeV B [GeV^{-}2]
^{4}He	10.0±3.6	–
^{12}C	7.2±2.5	10.0±2.1
^{27}Al	12.1±2.1	8.1±1.9
^{49}Ti	–	18.6±2.1
^{64}Cu	16.5±13.8	14.6±2.3
^{109}Ag	26.4±3.5	26.0±2.7
^{197}Au	–	56.7±8.2

[15] can be significant on nuclei that fall in between the available Compton scattering data, as shown in Table 5.4.

The second modification is adding an energy dependence to $g(Q^2)$. The existing 3 and 5 GeV data provides very little insight to this. Considering again Table 5.3, the central values of B can increase or decrease with lower energy depending on the nuclei, and the error bars are large enough that any shift could be considered within uncertainty. Instead, we search for a functional form, $g'(Q^2, E_\gamma)$, that describes the measured asymmetries, but converges back to the existing fits to Compton data at the energies they were measured. More formally:

$$\lim_{E_\gamma \to 5GeV} \Big(g'(Q^2, E_\gamma) \Big) = g(Q^2) \tag{5.2}$$

To that end, I suggest a g' of the form:

$$g'(Q^2, E_\gamma) = \exp\left(\frac{-tB(Z)}{2} \Big(1 - \frac{B't}{Z} \Big(\frac{1}{E_\gamma^3} - \frac{1}{5^3} \Big) \Big) \right) \tag{5.3}$$

Figure 5.7

Compton scattering B values from Koschii at $E_\gamma = 5$ GeV [15] fit with respect to Z.

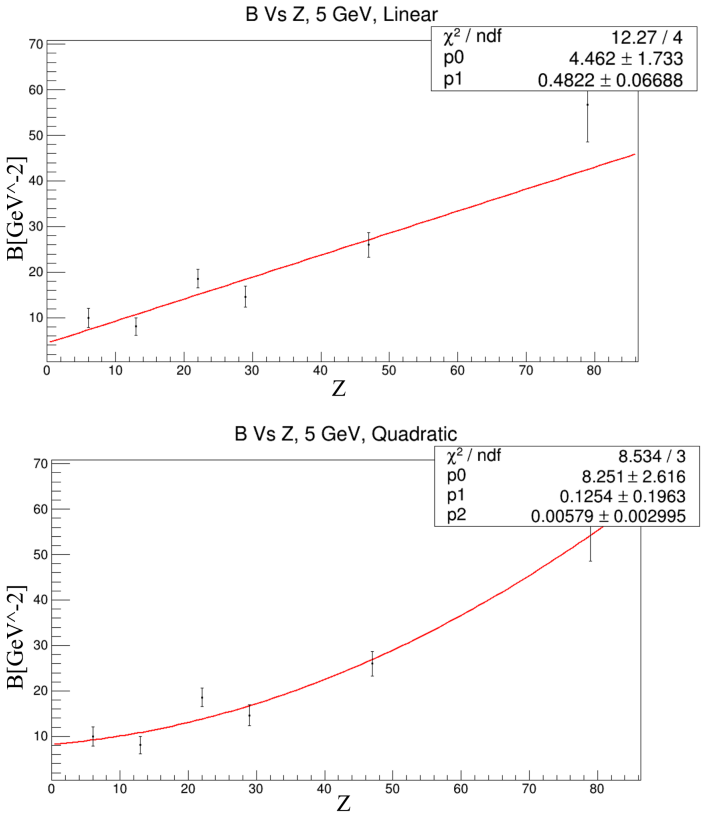

Where $B' \approx 7.2$ GeV is an additional constant fit to MAMI's carbon data, and E_γ is the energy of the photon, which is given in Koshchii's paper as $\omega = \frac{(p_1+q_1)^2-M^2}{2M}$.

The choice of the complicated term $\left(1 - \frac{B't}{Z}\left(\frac{1}{E_\gamma^3} - \frac{1}{5^3}\right)\right)$ serves a number of purposes. Importantly, the difference $\left(\frac{1}{E_\gamma^3} - \frac{1}{5^3}\right)$ forces the desired convergence back to the Compton scattering at $E_\gamma = 5$ GeV to maintain agreement with the original fits to data. The choice of $\approx \frac{t^2}{E_\gamma^3}$ scaling is strange, and difficult to justify. It is motivated largely by two factors. First, the energy scaling needs to collapse very quickly when $E_b < 1$ GeV in order to both enhance the 0.57 GeV points from MAMI, while leaving the 1.1 GeV points from PREX nearly unaffected. Second, the scaling of MAMI's carbon points show a difficult linear

Table 5.4

Values of B extracted by Koshchii et al. from fitting the functional form "$\alpha \exp(\frac{-Bt}{2}) + \sigma$" to Compton data [15]. The second two columns, highlighted in grey, are the results of this section's interpolated form. Without interpolation, nuclei are assigned B from existing nuclei. Interpolation provides an alternative estimate.

Target	$\omega \approx$ 3GeV B [GeV$^-$2]	ω =5GeV B [GeV$^-$2]	B=4.46+0.48Z B(Z) [GeV$^-$2]	B=8.22+0.125Z+0.006Z^2 B(Z^2) [GeV$^-$2]
^{4}He	10.0±3.6	–	5.4	8.5
^{12}C	7.2±2.5	10.0±2.1	7.4	9.2
^{27}Al	12.1±2.1	8.1±1.9	10.7	10.8
^{28}Si	12.1±2.1	8.1±1.9	11.2	11.1
^{40}Ca	–	18.6±2.1	14.1	13.0
^{48}Ca	–	18.6±2.1	14.1	13.0
^{49}Ti	–	18.6±2.1	15.1	13.8
^{64}Cu	16.5±13.8	14.6±2.3	18.5	16.7
^{90}Zr	26.4±3.5	26.0±2.7	23.8	22.5
^{109}Ag	26.4±3.5	26.0±2.7	27.1	26.9
^{197}Au	–	56.7±8.2	42.6	54.3
^{208}Pb	–	56.7±8.2	44.0	57.4

behavior in Q^2 that makes them very hard to fit. The $\approx \frac{t^2}{E_\gamma^3}$ scaling provides both this transition to a linear form at low energy, and suppresses it fast enough to agree with higher energy data. Alternative scalings of the forms $\frac{t^2}{E_\gamma^4}$, $\frac{t}{E_\gamma}$, $\frac{t}{E_\gamma^2}$, and $\frac{t}{E_\gamma^3}$ were also attempted, but none provided as close of a minimization as the $\frac{t^2}{E_\gamma^3}$.

To fit the constant B', the A_T model predictions from Koschii for each nuclei at its experimentally measured Q^2 were collected. The model predictions had their existing $g(Q^2)$ removed, and replaced by the $g'(Q^2, E_\gamma)$ of Equation 5.3 using a simple factor of g'/g. The αZ^2 suppression was applied, then the residuals of each point with respect to the

experimentally measured values were calculated. The value of B' was used to minimize the sum of the error weighted residuals, where the errors were a quadrature sum of the model uncertainty, and experimental uncertainty.

This form is purely phenomenological, but it does a better job describing data across the board. In fact, when combined with the $(1 - CZ^2\alpha)$ suppression discussed in Section 5.1, every measured nuclei falls with $Z \geq 6$ falls within 2σ of model predictions, which can be seen clearly in the residuals in Figure 5.8. The corrections and minimizations for each step are shown in Figure 5.5. While Equation 5.3 supplies some significant corrections in the energy range of available BNSSA measurements, it converges back to Compton scattering measurements fast enough to be nearly immeasurable at $E_\gamma = 3$ GeV. This can be seen in the scaling of effective B values given at different values of E_γ in Table 5.6.

Figure 5.8

All electron-nucelus BNSSA residuals when compared to model predictions by Koschhii, compared to the same data using Equation 5.3 to add energy dependence.

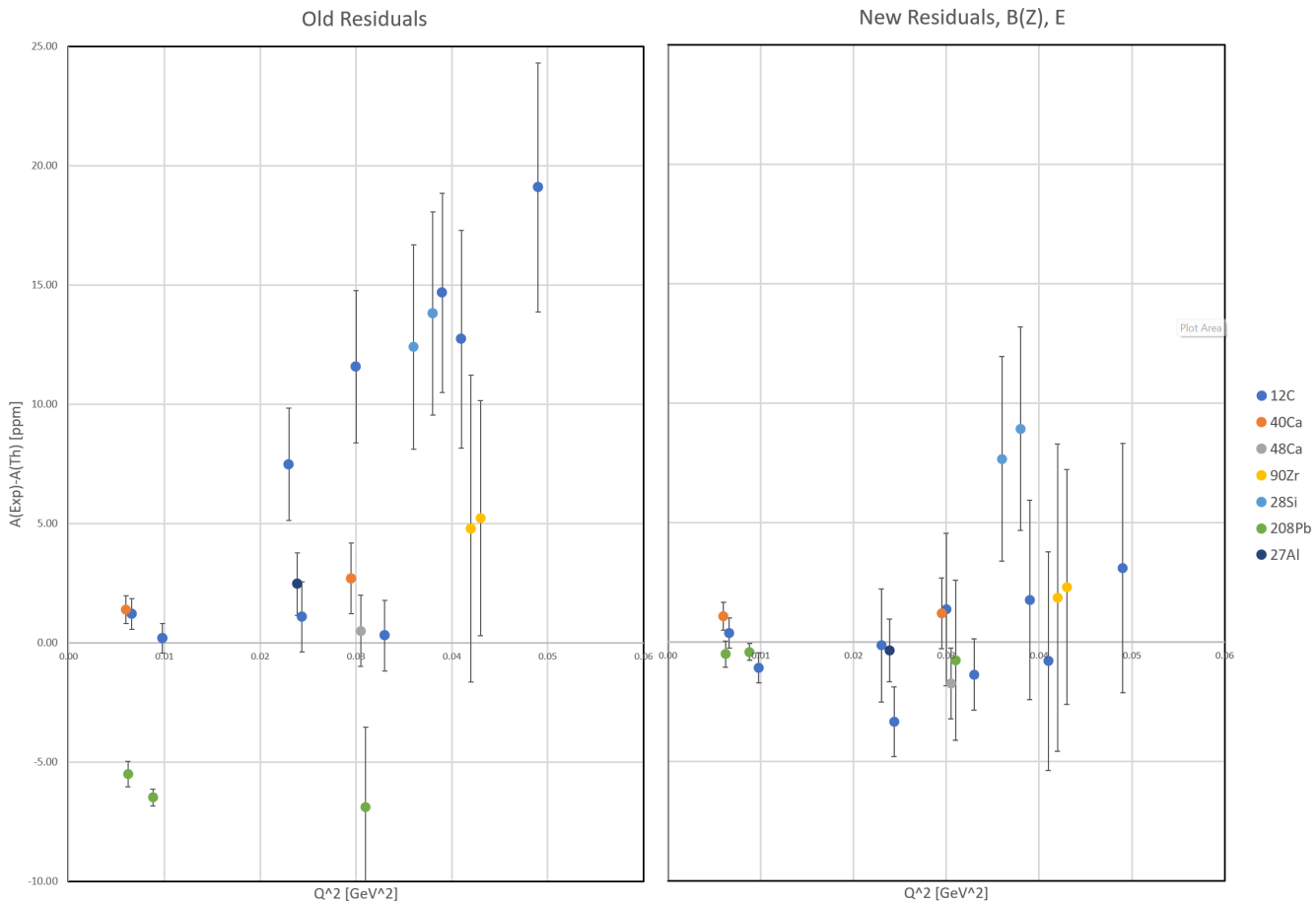

Table 5.5

The size of corrections compared to $A_{n,th}$ predicted by Koshchii et al. [15], using the methods described in the section above. The fit minimizations (error weighted sum of residuals) are given in the last row, showing our ability to describe the data increasing in each step.

Experiment	Target	$A_{n,Th}$	$\delta(B(Z^2))$	$\delta(\alpha Z^2)$	$\delta(E_\gamma)$	$A_{n,Fits}$	$A_{n,Exp}$
PREX	^{12}C	-6.3	-0.03	0.03	-1.28	-7.57	-6.49
QWEAK	^{12}C	-9.6	-0.10	0.05	-4.37	-14.02	-10.68
PREX-II	^{12}C	-5.1	-0.01	0.03	-0.84	-5.93	-6.30
MAMI	^{12}C	-8.5	-0.08	0.05	-7.60	-16.13	-15.98
MAMI	^{12}C	-9.1	-0.11	0.05	-10.15	-19.32	-20.67
MAMI	^{12}C	-9.2	-0.15	0.05	-12.82	-22.12	-23.88
MAMI	^{12}C	-9.2	-0.16	0.05	-13.43	-22.74	-21.93
MAMI	^{12}C	-9.2	-0.19	0.05	-15.87	-25.20	-28.30
CREX	^{12}C	-9.4	-0.13	0.05	-1.59	-11.07	-9.70
PREX	^{208}Pb	-6.2	0.02	6.07	-0.03	-0.14	0.28
PREX-II	^{208}Pb	-5.1	0.01	4.99	-0.02	-0.11	0.40
CREX	^{208}Pb	-6.3	0.07	6.11	-0.05	-0.16	0.60
QWEAK	^{27}Al	-9.7	0.31	0.23	-3.37	-12.53	-12.16
MAMI	^{28}Si	-9.4	0.50	0.25	-5.49	-14.14	-21.81
MAMI	^{28}Si	-9.5	0.53	0.26	-5.66	-14.37	-23.30
PREX-II	^{40}Ca	-4.7	-0.08	0.28	-0.52	-5.02	-6.10
CREX	^{40}Ca	-7.3	-0.62	0.46	-1.34	-8.81	-10.00
CREX	^{48}Ca	-8.9	-0.79	0.57	-2.01	-11.14	-9.40
MAMI	^{90}Zr	-12	-1.03	3.04	-4.95	-14.93	-16.79
MAMI	^{90}Zr	-11.8	-1.03	3.00	-4.90	-14.73	-17.03
Minimization	–	23.21	23.12	10.11	5.09	5.09	0.0

Table 5.6

Effective values of B given at each point's Q^2, E, and Z showing the fast convergence when E is increased.

Experiment	Target	Koschii B	B(Z^2)	B($E_{\gamma=Ex}$)	B($E_{\gamma=3Gev}$)	B($E_{\gamma=5Gev}$)
PREX	^{12}C	10.0	9.18	8.61	9.17	9.18
QWEAK	^{12}C	10.0	9.18	8.71	9.17	9.18
PREX-II	^{12}C	10.0	9.18	8.47	9.17	9.18
MAMI	^{12}C	10.0	9.18	8.34	9.17	9.18
MAMI	^{12}C	10.0	9.18	8.42	9.17	9.18
MAMI	^{12}C	10.0	9.18	8.50	9.17	9.18
MAMI	^{12}C	10.0	9.18	8.52	9.17	9.18
MAMI	^{12}C	10.0	9.18	8.56	9.17	9.18
CREX	^{12}C	10.0	9.18	9.03	9.17	9.18
PREX	^{208}Pb	56.7	57.43	57.31	57.43	57.43
PREX-II	^{208}Pb	56.7	57.43	57.29	57.43	57.43
CREX	^{208}Pb	56.7	57.43	57.37	57.43	57.43
QWEAK	^{27}Al	8.1	10.82	10.49	10.82	10.82
MAMI	^{28}Si	8.1	11.11	10.76	11.10	11.11
MAMI	^{28}Si	8.1	11.11	10.78	11.10	11.11
PREX-II	^{40}Ca	18.6	13.04	12.65	13.04	13.04
CREX	^{40}Ca	18.6	13.04	12.92	13.04	13.04
CREX	^{48}Ca	18.6	13.04	12.90	13.04	13.04
MAMI	^{90}Zr	26.4	22.50	22.38	22.49	22.49
MAMI	^{90}Zr	26.4	22.50	22.38	22.49	22.49

5.4 Future Experiments

High intensity electron beam facilities such as CEBAF and MAMI are some of the few places that can support the difficult requirements of parity based scattering measurements. Currently the future of experiments in Jefferson Lab Hall A is dominated by electron

scattering off light nuclei. This includes polarization transfer measurements, like those discussed in Section 2.2.3, to extract the form factor of the neutrons. It is unlikely that these experiments will achieve the sensitivity in which the beam normal single spin asymmetry corrections will be necessary, but it is something that should be considered. Further into the future, experiments like MOLLER will need reliable models or asymmetry measurements on materials such as aluminum to account for scattering that takes place on the cell windows. Looking further still, a few authors have proposed using positrons to measure two photon effects directly using equipment at Jefferson Lab [49].

MAMI, on the other hand, has planned additional transverse measurements on carbon that could provide more useful information regarding the energy scaling of A_n [47]. Arguably more important, MAMI has also proposed a program to directly measure Compton scattering data, which could help to remedy the uncertainty in the existing models significantly [15].

Despite the attempts to close the gaps between light and heavy nuclei, there are still wide gaps in the available data across the nuclear chart in both the transverse and longitudinal cases. The zero A_T of the 'PREX problem' is now confirmed with a high degree of certainty, however nuclei with Z<20 show little, if any, of the same suppression. Due to the difference in kinematics, including energies and angles, MAMI's measurements on intermediate nuclei are difficult to compare directly to those of PREX(II) and CREX. Additional transverse asymmetry measurements on more nuclei at forward angles would provide valuable information to constrain the rate of suppression for heavy nuclei.

References

[1] E. Rutherford. The scattering of alpha and beta particles by matter and the structure of the atom. *Phil. Mag. Ser. 6*, 21:669–688, 1911.

[2] K. A. Aniol et al. Parity violating electroweak asymmetry in polarized-e p scattering. *Phys. Rev. C*, 69:065501, 2004.

[3] D. Androić et al. Precision measurement of the weak charge of the proton. *Nature*, 557(7704):207–211, 2018.

[4] F. Halzen and Alan D. Martin. *Quarks and Leptons: An Introductory Course In Modern Particle Physics*. Wiley, 1984.

[5] Mark Thomson. *Modern Particle Physics*. Cambridge University Press, 2013.

[6] M Thiel, C Sfienti, J Piekarewicz, C J Horowitz, and M Vanderhaeghen. Neutron skins of atomic nuclei: per aspera ad astra. *Journal Phys. G*, 46(9):093003, Aug 2019.

[7] Jonathan Wexler. *Measurement of the Parity Violating Asymmetry in Elastic Electron Scattering off ^{208}Pb*. PhD thesis, University of Massachusetts, 2014.

[8] L. C. Maximon and J. A. Tjon. Radiative Corrections to Electron-Proton Scattering. *Phys. Rev. C*, 62:054320, Oct 2000.

[9] P. A. M. Guichon and M. Vanderhaeghen. How to reconcile the rosenbluth and the polarization transfer methods in the measurement of the proton form factors. *Phys. Rev. Lett.*, 91:142303, Oct 2003.

[10] A. De Rújula, J.M. Kaplan, and E. de Rafael. Elastic scattering of electrons from polarized protons and inelastic electron scattering experiments. *Nucl. Phys. B*, 35(2):365–389, 1971.

[11] Andrei V. Afanasev and N.P. Merenkov. Collinear photon exchange in the beam normal polarization asymmetry of elastic electron–proton scattering. *Phys. Lett. B*, 599(1):48–54, 2004.

[12] Mikhail Gorchtein. Doubly virtual compton scattering and the beam normal spin asymmetry. *Phys. Rev. C*, 73:035213, Mar 2006.

[13] E. D. Cooper and C. J. Horowitz. Vector analyzing power in elastic electron-nucleus scattering. *Phys. Rev. C*, 72:034602, Sep 2005.

[14] M. Gorchtein and C. J. Horowitz. Analyzing power in elastic scattering of electrons off a spin-0 target. *Phys. Rev. C*, 77:044606, Apr 2008.

[15] Oleksandr Koshchii, Mikhail Gorchtein, Xavier Roca-Maza, and Hubert Spiesberger. Beam-normal single-spin asymmetry in elastic scattering of electrons from a spin-0 nucleus. *Phys. Rev. C*, 103:064316, Jun 2021.

[16] A. Freyberger, F. E. Hannon, A. S. Hofler, A. Hutton, and R. Kazimi. Upgrading the CEBAF Injector with a New Booster, Higher Voltage Gun, and Higher Final Energy. *Conf. Proc. C*, 1205201:1945–1947, 2012.

[17] P. A. Adderley et al. Two Wien Filter Spin Flipper. *Conf. Proc. C*, 110328:862–864, 2011.

[18] Reza Kazimi. Simultaneous Four-hall Operation for 12 GeV CEBAF. In *4th International Particle Accelerator Conference*, page THPFI091, 2013.

[19] Rupesh Silwal. *Probing the Strangeness Content of the Proton and the Neutron Radius of 208Pb using Parity-Violating Electron Scattering*. PhD thesis, Department of Physics, University of Virginia, Virginia U., 2012.

[20] Caryn Palatchi. Injector setup and ihwp in/out polarization difference. Technical report, PREX/CREX internal document 418-v1, Oct 2019.

[21] Michael Spata. Early Commissioning Experience and Future Plans for the 12 GeV Continuous Electron Beam Accelerator Facility. In *27th International Linear Accelerator Conference*, page MOIOB01, 2014.

[22] P. Forck, P. Kowina, and D. Liakin. CERN Accelerator School, beam diagnostics, Dourdan, France, 28 May - 6 June 2008. In D. Brandt, editor, *CERN Yellow Reports: School Proceedings*, page 187, 2009.

[23] J. Denard, A. Saha, and G. Lavessiere. High Accuracy Beam Current Monitor System for CEBAF's Experimental Hall A. *Conf. Proc. C*, 0106181:2326–2328, 2001.

[24] Kiadtisak Saenboonruang. *Measurement of the Neutron Radius of ^{208}Pb Through Parity Violation in Electron Scattering*. PhD thesis, Department of Physics, University of Virginia, Virginia U., 5 2013.

[25] Hall A Møller Polarimeter, Feb 2019.

[26] Dustin McNutly. At analysis update (final results). Technical report, PREX/CREX internal document 505-v2, Aug 2021.

[27] J.A. Magee et al. A novel comparison of møller and compton electron-beam polarimeters. *Phys. Lett. B*, 766:339–344, 2017.

[28] J. M. Grames, C. K. Sinclair, M. Poelker, X. Roca-Maza, M. L. Stutzman, R. Suleiman, Md. A. Mamun, M. McHugh, D. Moser, J. Hansknecht, B. Moffit, and T. J. Gay. High precision 5 mev mott polarimeter. *Phys. Rev. C*, 102:015501, Jul 2020.

[29] Kent Paschke. PREX/CREX design document. Technical report, PREX/CREX internal document 2-v3, May 2017.

[30] *PREX2-CREX Target*. Jefferson Lab, Feb 2018.

[31] Cameron Clarke. High luminosity lead-208 targets for the prex-2 experiment. Technical report, PREX/CREX internal document 470-v2, Oct 2020.

[32] Ciprian Gal. Hall A septum magnet. PREX/CREX internal communication, May 2019.

[33] J. Alcorn et. al. Basic instrumentation for hall A at jefferson lab. *Nucl. Instrum. Meth. A*, 522(3):294–346, 2004.

[34] Chandan Ghosh. Experience with GEM detectors during the PREX-2 Physics run. In *APS Division of Nuclear Physics Meeting Abstracts*, volume 2020 of *APS Meeting Abstracts*, page SK.006, January 2020.

[35] Ryan Richards. *Measurements of the Beam Normal Asymmetry using Polarized Elastic Electron Scattering off Various Spin-0 Nuclei at 1 GeV*. PhD thesis, Stony Brook University, Dec 2021.

[36] Devi Adhikari. *Neutron Skin Measurement of 208Pb Using Parity-Violating Electron Scattering*. PhD thesis, Idaho State University, Aug 2021.

[37] Dustin McNutly. Main detectors for PREX-II/CREX, Jul 2018.

[38] Trent Allison. JLab Operations Procedure: Hall A BCM Linearity Procedure, Feb 2014.

[39] Philip R. Bevington and D. Keith Robinson. *Data reduction and error analysis for the Physical Sciences*. McGraw-Hill, 2010.

[40] Philippe Pierre Pebay. Formulas for robust, one-pass parallel computation of covariances and arbitrary-order statistical moments. *OSTI*, 9 2008.

[41] Cameron Clarke. *Measurement of Parity Violating Asymmetry in Elastic Electron Scattering off 48Ca*. PhD thesis, Stony Brook University, 12 2021.

[42] D. Adhikari and et al. New measurements of the beam-normal single spin asymmetry in elastic electron scattering over a range of spin-0 nuclei. *Phys. Rev. Lett.*, 128:142501, Apr 2022.

[43] S. Abrahamyan and et al. New measurements of the transverse beam asymmetry for elastic electron scattering from selected nuclei. *Phys. Rev. Lett.*, 109(19), Nov 2012.

[44] Dinayadura Buddhini Waidyawansa. *A 3% Measurement of the Beam Normal Single Spin Asymmetry in Forward Angle Elastic Electron-Proton Scattering using the Qweak Setup*. PhD thesis, Ohio University, Aug 2013.

[45] D. Androić et al. Measurement of the Beam-Normal Single-Spin Asymmetry for Elastic Electron Scattering from ^{12}C and ^{27}Al. *Phys. Rev. C*, 104:014606, 2021.

[46] A. Esser and et al. First measurement of the Q^2 dependence of the beam-normal single spin asymmetry for elastic scattering off carbon. *Phys. Rev. Lett.*, 121:022503, Jul 2018.

[47] A. Esser et al. Beam-normal single spin asymmetry in elastic electron scattering off 28si and 90zr. *Phys. Lett. B*, 808:135664, 2020.

[48] L. Criegee, G. Franke, A. Giese, T. Khal, G. Poelz, U. Timm, H. Werner, and W. Zimmermann. Small Angle Photon Scattering on Complex Nuclei. *Nucl. Phys. B*, 121:38–44, 1977.

[49] G. N. Grauvogel, T. Kutz, and A. Schmidt. Target-normal single spin asymmetries measured with positrons. *Eur. Phys. J. A*, 57(6):213, 2021.

Appendix A: Just Another Parity Analyzer

The collaboration maintained a software package that was named JAPAN (Just Another Parity Analyzer). This was the main analysis tool, serving as a jumping off point for the majority of the analysis given in this document. Its main job was to serve as a framework for core steps of analyses, collecting all the litany of calculations, variables, and macros, and applying them to the data in a analysis ”passes”. To undertake this job it was written in a modular way, with calculations written into individual data handlers that take their own configuration files. This gave the engine versatility, allowing for analyses to be added in a standard way, and allowing for easy access to common variables. Using this format, JAPAN was able to efficiently order the data handlers and reduce the likelihood of individual calculations making bad assumptions regarding their order in the process.

JAPAN was written in C++, and uses ROOT-CERN (root), a data analysis framework for nuclear and particle physics. Root contains a large set standard data analysis tools, as well as its own set of programming language interpreters. This allowed individuals to write macros for complicated calculations in their language of choice, and easily include them in the final analysis. Each analysis pass produced its own set of .root files which contain ”trees” of information that can be accessed in a live root session to make plots or test simple calculations on. To account for calculations that require information such as run-long means as input values, JAPAN was able to run multiple passes in succession, referencing its own output files each time. While this could be done as many times as needed, only two passes were required for the final output.

JAPAN was also responsible for producing a significant portion of the information available in the live data monitors via a graphical user interface tool called PAnGUIn (Parity Analyzer Graphic User Interface). PAnGUIn plots the data from a special rootfile made by JAPAN that’s updated incrementally so the data quality can be spot checked very rapidly.

JAPAN was transitioned from the previous Hall A parity analysis software called PAn (Parity Analyzer), and it will likely be built upon for future Jefferson Lab parity experiments. Lastly, To prevent the headaches associated with many people contributing to the same software, JAPAN was version controlled with a GitHub repository which can be viewed at: https://github.com/JeffersonLab/japan

Appendix B: Personal Contributions

This chapter will serve as a list of everything I personally did, with quick summaries of how it related to the experiment.

B.1 Current Monitor Sync

The beam current monitors were surveyed after a sync issue was discovered that delayed the cavity signals. To do this, a clean beam trip was chosen, and the sub block signals for every current monitoring device were compared. A clean beam trip should be nearly instantaneous, and appear in at most one sub block. Figure B.1 shows the disagreement between a cavity and the analog downstream BCM. After an additional investigation of the time delayed BCM's it was discovered that a hardware setting was enforcing additional signal processing on the cavities, resulting a delayed and smoothed signal.

Figure B.1

Current readback from cavity4(black) compared to the analog downstream(red) showing the time delayed response to the trip. The y axis is in hardware units, and an offset has been applied to cavity signal to bring it to the same level as the digital BCM.

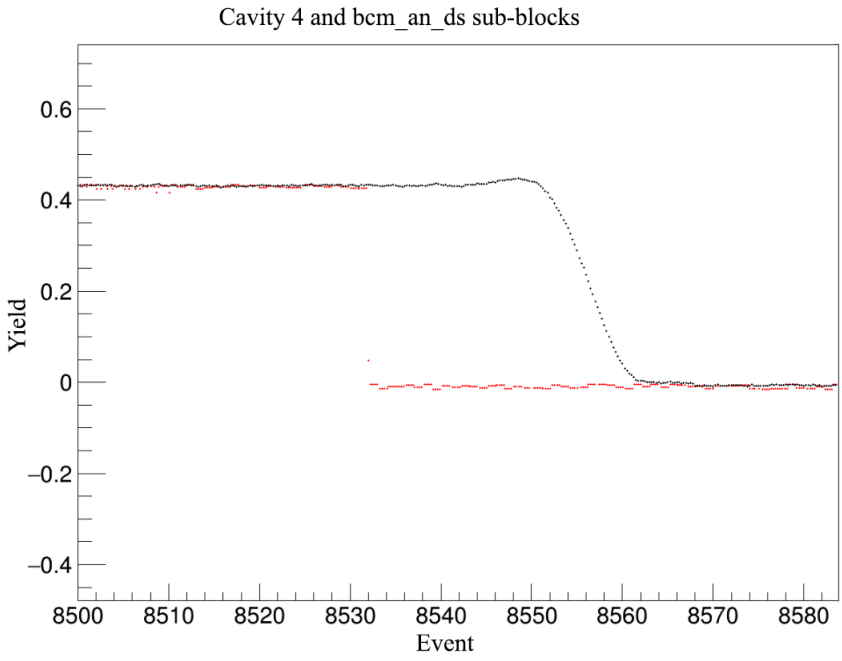

B.2 Epics Variable Map

Nearly every system in the accelerator regularly publishes their readbacks to Experimental Physics and Industrial Control System (EPICS). The time resolution of this system is very coarse, so it is mostly used to record values that change on slow time scales. Hardware set points and the slow spin controls are some examples. Before the start of PREX-II, a list of the current EPICS variables needed to be compiled and verified. There is no central repository for variables, as they can change (often without any record) any time a system is worked on.

To set this up, a number of old experiment's DAQ startup scripts were mined for their lists of EPICS variables. These lists were combined, resulting in ~2000 unique variables. These variables were then checked via a command line query to the live EPICS system to see if they were still active, and see what data type they returned. The list of active variables was then distributed to system experts to decide which were still relevant, and to add missing descriptions where needed. The final list of ~500 variables and types was used in the DAQ startup script for PREX and CREX. The list was also exported into a map file that JAPAN uses to build a tree that contains each run's EPICS information.

B.3 PostPAN Regression Vs JAPAN Regression

PostPAN was a library of scripts originally designed to perform analysis on the outputs of PAn, the predecessor to JAPAN. It was designed to do a lot of the analysis steps for PAn that eventually got included in JAPAN, resulting in some redundancy. Since PostPAN was the preferred analysis tool for some users, particularly the Lagrange analysis, a check was needed to make sure it was agreeing with JAPAN on intermediate steps. While comparing the regression slopes of the two methods it was noted that while the slopes agreed, the associated uncertainties did not. After an investigation into code, it was discovered that PostPAN was using the RMS of the dependent variable before regression to calculate an uncertainty, while JAPAN was using the RMS of the dependent variable after regression.

B.4 Pedestal Verification

As discussed in section 4.3.3, the pedestals were set in map files and used by JAPAN. Any time a new current calibration was done, or any electronics relevant change was made to detector, it usually required a corresponding map file to reflect the change. Some examples of these electronic changes included tweaks to high voltage settings, replacing power supplies, running in single spectrometer modes, and compensations for target degradation.

As one could imagine, this resulted in a lot of map files, some of which were created quickly during data collection. There were a number of steps that needed verification:

• Checking to make sure pedestal changes were correctly reflected in the JAPAN rootfiles for a variety of detectors. This meant calculating the pedestals from data for each run, and comparing it to the values in the map file. If JAPAN had an error in how it was applying the pedestals it would be visible here. Additionally, if a run was processed before a new mapfile was created, this check will find that discrepancy so the runs can be reprocessed. This was actually quite common, as calibration runs needed to be analyzed to extract pedestals, and often a few runs would take place before a mapfile was ready for the period.

• Checking to make sure a mapfile was created for each calibration or configuration change.

• Checking to make sure data in the mapfiles matched the calibrations.

These checks had to be automated to cover thousands of runs. The script read through the mapfile directory, recreated the way JAPAN chose mapfiles, processed the text in the mapfiles for pedestals, opened each run to sample its data for the reverse calculation check, and combined the information across all the runs. The resulting plots of the type shown in Figure B.2 were used to make sure all the calibrations were included used as intended.

Figure B.2

Fluctuations in the pedestal of SAM2 across the experiment. The units on the y axis are just the hardware yield. Each change corresponded to a new mapfile, and the period of noise was due to a change in normalizing bcm.

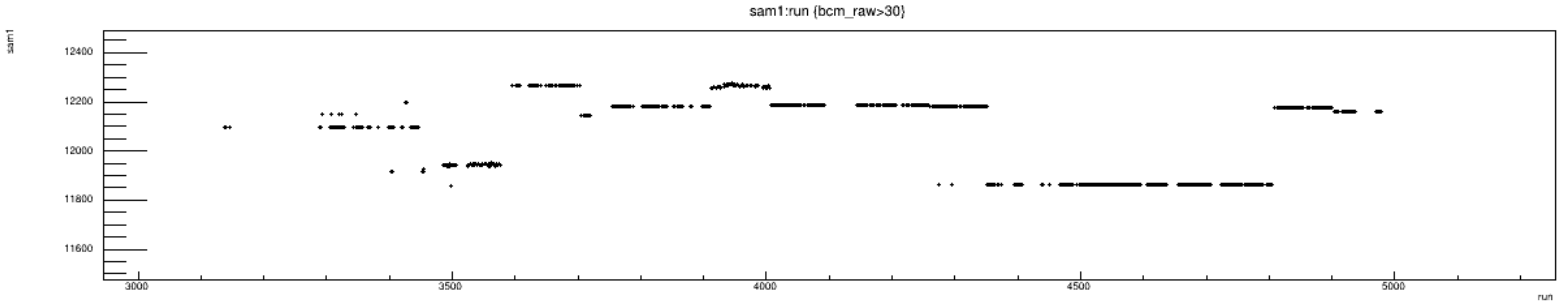

B.5 GUI Additions

For ease of use, some of the live tools for the experiment used custom GUI's (Graphic User Interface) instead of command line tools. One of these tools was named 'Green Monster'. It was a python based GUI that contained tools for working with the Compton polarimeter. I made a set of additions for for controlling and reading the live states and settings for devices on the laser table for use during PITA scans. Reading the device values could be done using the EPICS system, but setting the values required sending commands to the control boards, which took an investigation of deprecated scripts to find. Contributions were also made to the charge feedback GUI's, both to fix readback issues during run, and enable restarting charge feedback without restarting the GUI.

B.6 Recalculation of Main Asymmetries

The main way the final raw asymmetry was extracted from JAPAN's rootfiles was via PostPAN, and a tool called the aggregator. Both of these tools had methods to combine and reduce the numerous run-wise outputs of JAPAN into singular rootfiles that represent longer time scales. A few students also maintained their own scripts for doing the same calculations. The previously mentioned pedestal calculation scripts proved easy to modify for this task. They required modification to include a large number of new variables, and better memory management to handle the larger volume of data near the end of the experiment. This also included writing separate tools to pull information from the run list database. The work was used as a confirmation of results from the preferred PostPAN and aggregator outputs.

B.7 Shift and Analysis Coordinator Work

I took a significant number of shifts in the experiment. This included 36 operator shifts, and 21+29 analysis shifts for PREX-II and CREX respectively. The analysis shifts were

devoted data quality monitoring positions, where the duty was ensuring that the live data remained reasonable throughout the shift. In addition, I did a week as an analysis coordinator (WAC). This job entailed reviewing every run taken during that week period, checking for issues in the data, and applying whatever fixes were needed to bring them up to standard. A lot of work I did at this time was attempting to automate all the scripts used to produce the slug and daily summary plots to reduce the workload for future WAC's. The "EZ_WAC.sh" script was used through until the end of the experiment.

B.8 Respin Setup

Standing up the secondary JAPAN install to access the lab's batch computing system (the farm), as discussed in Section 4.5, took a lot of work. The farm doesn't have access to the same file systems as the aDAQ computers where the existing JAPAN install was located, so importing it was not a simple copy and paste. The first issue was reviewing file pathing for every script, as a lot of the analysis scripts were written for use on the aDAQ machines and weren't designed for use in a different directory structure. This lead to the second issue, tracking down and importing the packages that weren't part of the JAPAN repository. At this point, JAPAN was tested to make sure it reproduced the same analysis on single runs in a live session as it did on the aDAQ machines.

After setting up the new install, creating the batch computing scripts was also nontrivial. All the analysis steps were made to run automatically, and this required a rewrite of a number of scripts used to organize files so that they could run in parallel without interfering with eachother. Nodes on the farm also lacked access to additional storage locations, and had to make requests to cache-in files that they needed to run. This caching step actually accounted for the majority of run time of the respins.

B.9 Respin Output Comparison

After each respin, the results of individual analyses were obviously reviewed by the people who made them. But the combined effects of all changes required a run by run comparison of inputs and outputs. The previously mentioned pedestal checking scripts were also well suited for this task. The main values of interest in this analysis were the total count differences between respins. Reviewing the data generally resulted in a gain of events, as more careful ways of dealing with problem data made more events usable. The total change in events from the first respin was $\approx 3.7\%$. The results were also broken down into a variety of time windows including minirun, run, and slug wise differences, as shown in Figure B.3, to make it easier to identify what parts of the experiment gained and lost the most data.

A variety of detector signals were also checked, including the main detector asymmetries on each target, charge asymmetries, and position differences. The same comparisons were also repeated separately for the transverse runs. The reduction in noise for detectors is visible by both inspection, and the change in fit parameter uncertainties, shown for the main detector in Figure B.4. The remaining outliers were subject to an additional investigations before the next respin.

Figure B.3

Differences in counts shown as with different time resolutions. The vertical axis is given in counted multiplets, while the horizontals are given in run number or slug number(miniruns are plotted as a function of run). Miniruns look especially noisy, as many runs gained enough events to require the creation of additional miniruns. This resulted in many miniruns having a difference greater than the size of a whole minirun.

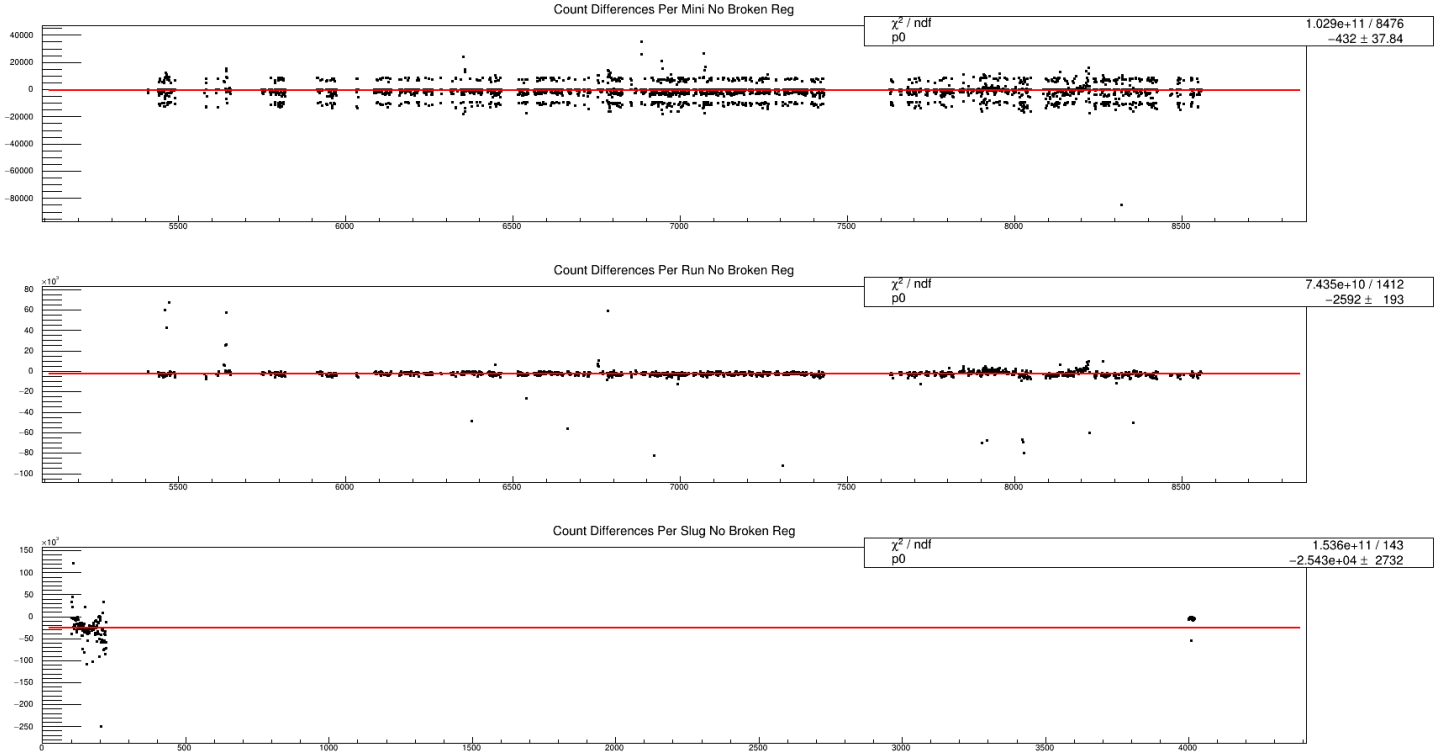

Figure B.4

Differences in main detector asymmetries shown as with different time resolutions. The noise reduction is obvious, despite the inclusion of previously removed data.

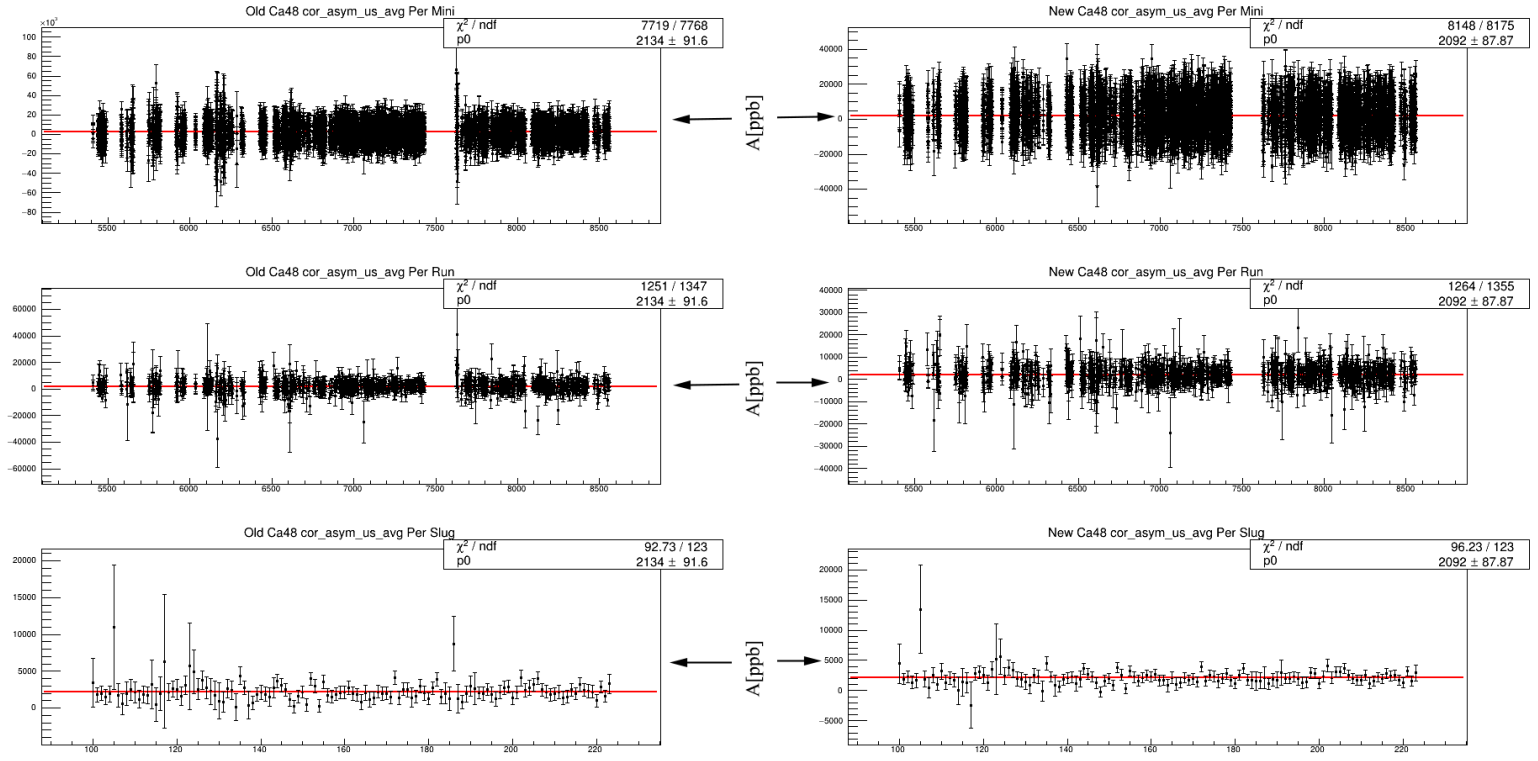

B.10 Monitor Slope Correlations

To verify the ability of the EvMon devices to effectively reduce the monitor cross correlations, a systematic check was made of the distribution of slopes for the BPM's and EvMon's. Figures B.5 and B.6 show the correlation of device slopes on lead for the BPM's and EvMon's respectively. In the BPM case, the appearance of strong correlations in the off diagonal plots indicates detectors whose corrections are becoming redundant. While some small residual correlation may exist in the EvMon's, the difference between the two sets of devices is obvious. These checks were made for all targets, but the results were consistent and don't require further discussion.

Figure B.5

These plots show the BPM versus main detector asymmetry slopes for each BPM. Each plot checks how the slopes from one BPM correlate with another. The diagonal elements correlate the BPM slopes with themselves and are therefore perfectly correlated.

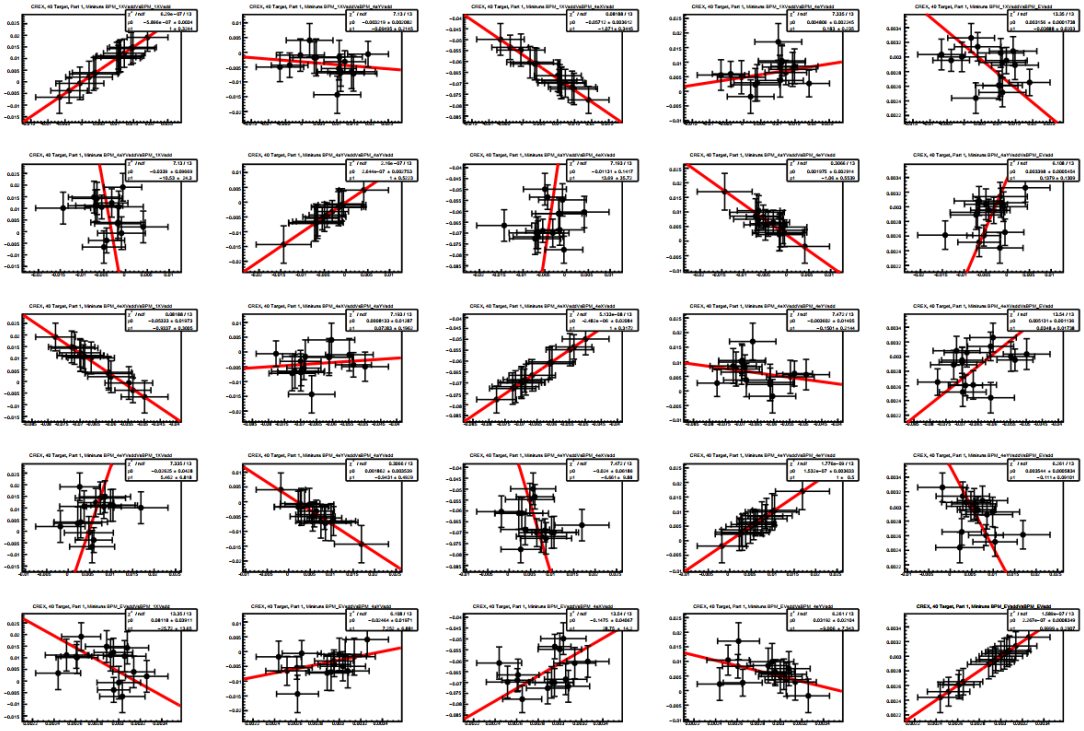

Figure B.6

These plots show the EvMon versus main detector asymmetry slopes for each EvMon. Each plot checks how the slopes from one EvMon correlate with another. The diagonal elements correlate the EvMon slopes with themselves and are therefore perfectly correlated.

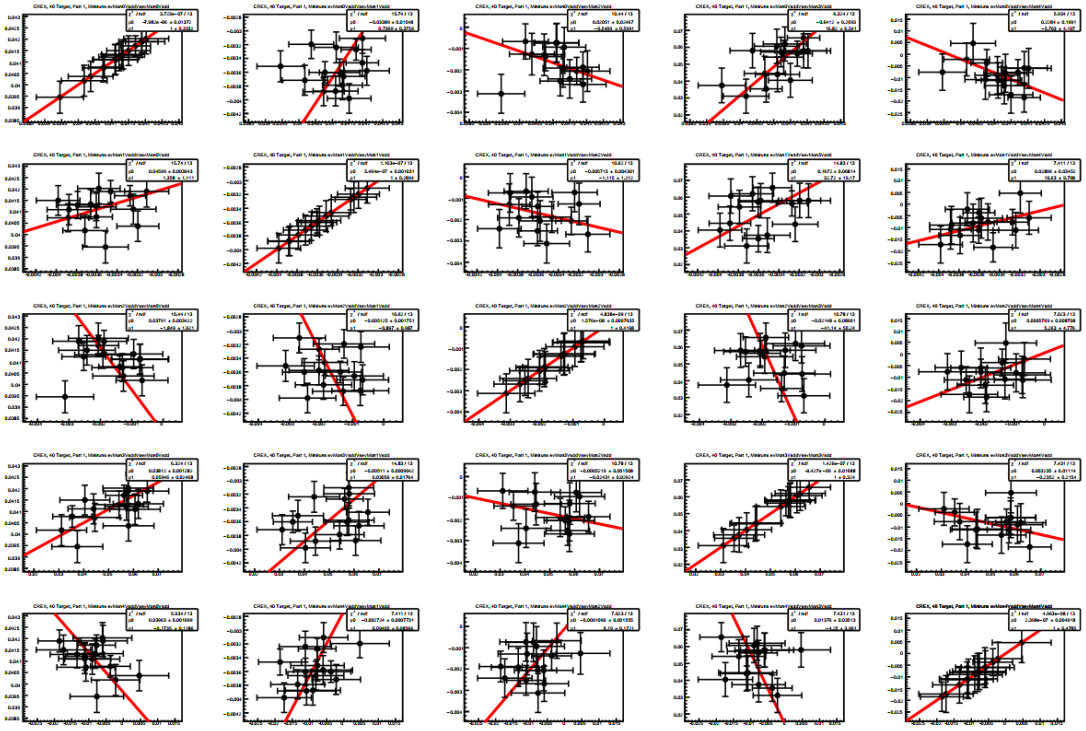

B.11 Multiplet Sizes

While the size of the multiplets shouldn't make a statistically significant difference in the final measured asymmetry, and the randomized helicity patterns should prevent false asymmetries on the multiplet time scale from biasing the measurement, the possibility still existed that some sort of unknown helicity correlated false asymmetry was hidden in the choice of a four event multiplet. It was decided that a numerical check should be made to verify that other choices of multiplet sizes behaved statistics dictated they should. To this end, a set of five runs were used to check if modifying the number of events included in multiplets made any unusual changes to the results.

A script was written to recalculate the main detector mean and RMS starting at a multiplet size of two, and ending with a multiplet size of sixty four in increments of two. The results of which are plotted in Figure B.7. The mean value of the asymmetry fluctuates, but is well within the statistical uncertainty, and the RMS shrinks as the larger multiplet windows tend to result in multiplets whose asymmetries agree more often. This is the expected $\frac{1}{\sqrt{N}}$ scaling of asymmetry width.

Figure B.7

Two example histograms showing the two extremes: multiplets of two, and multiplets of sixty four. These histograms were produced for every increment of two, and showed nothing of note. The means and RMS also behave in a consistent way.

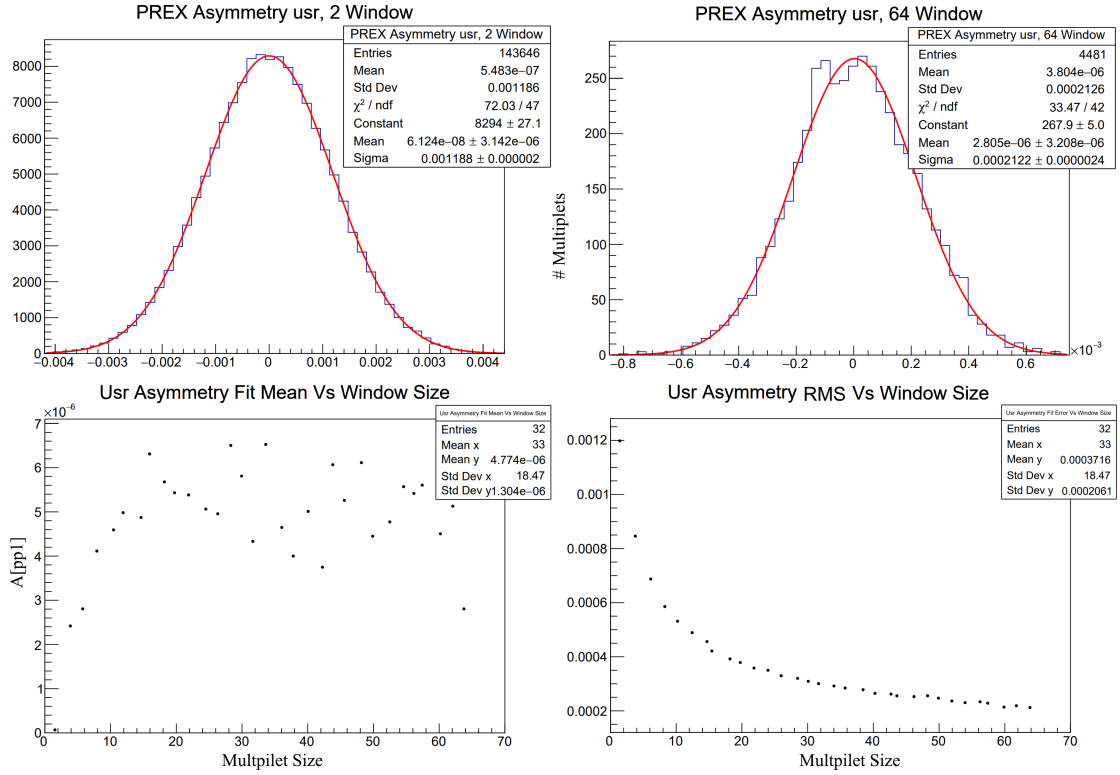

B.12 Previously Discussed

Finally, a summary of contributions that were covered in earlier parts of the paper. Implementing, testing, and tweaking the settings in the burp cuts, whose functionality was discussed in Section 4.3.2.3. Investigating the size and stability of regression slopes, discussed in section 4.1. Extracting the regression versus dithering systematic limits, discussed in Section 4.4.1. The investigation of the absolute asymmetry sign, discussed in

Section 4.2. The making of energy scaling fits forms, and the analysis of their impacts, discussed in Section 5.3.

Appendix C: Document Release Information

Document release information for reuse of figures.

American Physical Society
Reuse and Permissions License

28-Mar-2022

This license agreement between the American Physical Society ("APS") and Robert Radloff ("You") consists of your license details and the terms and conditions provided by the American Physical Society and SciPris.

Licensed Content Information

License Number:	**RNP/22/MAR/051953**
License date:	28-Mar-2022
DOI:	10.1103/PhysRevC.62.054320
Title:	Radiative corrections to electron-proton scattering
Author:	L. C. Maximon and J. A. Tjon
Publication:	Physical Review C
Publisher:	American Physical Society
Cost:	USD $ 0.00

Request Details

Does your reuse require significant modifications: No

Specify intended distribution locations:	United States
Reuse Category:	Reuse in a thesis/dissertation
Requestor Type:	Student
Items for Reuse:	Figures/Tables
Number of Figure/Tables:	1
Figure/Tables Details:	Fig 1
Format for Reuse:	Electronic

Information about New Publication:

University/Publisher:	Ohio University
Title of dissertation/thesis:	CREx Transverse Asymmetry Measurements
Author(s):	Robert w Radloff
Expected completion date:	Apr. 2022

License Requestor Information

Name:	Robert Radloff
Affiliation:	Individual
Email Id:	rr521111@ohio.edu
Country:	United States

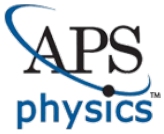

American Physical Society
Reuse and Permissions License

TERMS AND CONDITIONS

The American Physical Society (APS) is pleased to grant the Requestor of this license a non-exclusive, non-transferable permission, limited to Electronic format, provided all criteria outlined below are followed.

1. You must also obtain permission from at least one of the lead authors for each separate work, if you haven't done so already. The author's name and affiliation can be found on the first page of the published Article.
2. For electronic format permissions, Requestor agrees to provide a hyperlink from the reprinted APS material using the source material's DOI on the web page where the work appears. The hyperlink should use the standard DOI resolution URL, http://dx.doi.org/{DOI}. The hyperlink may be embedded in the copyright credit line.
3. For print format permissions, Requestor agrees to print the required copyright credit line on the first page where the material appears: "Reprinted (abstract/excerpt/figure) with permission from [(FULL REFERENCE CITATION) as follows: Author's Names, APS Journal Title, Volume Number, Page Number and Year of Publication.] Copyright (YEAR) by the American Physical Society."
4. Permission granted in this license is for a one-time use and does not include permission for any future editions, updates, databases, formats or other matters. Permission must be sought for any additional use.
5. Use of the material does not and must not imply any endorsement by APS.
6. APS does not imply, purport or intend to grant permission to reuse materials to which it does not hold copyright. It is the requestor's sole responsibility to ensure the licensed material is original to APS and does not contain the copyright of another entity, and that the copyright notice of the figure, photograph, cover or table does not indicate it was reprinted by APS with permission from another source.
7. The permission granted herein is personal to the Requestor for the use specified and is not transferable or assignable without express written permission of APS. This license may not be amended except in writing by APS.
8. You may not alter, edit or modify the material in any manner.
9. You may translate the materials only when translation rights have been granted.
10. APS is not responsible for any errors or omissions due to translation.
11. You may not use the material for promotional, sales, advertising or marketing purposes.
12. The foregoing license shall not take effect unless and until APS or its agent, Aptara, receives payment in full in accordance with Aptara Billing and Payment Terms and Conditions, which are incorporated herein by reference.
13. Should the terms of this license be violated at any time, APS or Aptara may revoke the license with no refund to you and seek relief to the fullest extent of the laws of the USA. Official written notice will be made using the contact information provided with the permission request. Failure to receive such notice will not nullify revocation of the permission.
14. APS reserves all rights not specifically granted herein.
15. This document, including the Aptara Billing and Payment Terms and Conditions, shall be the entire agreement between the parties relating to the subject matter hereof.

ELSEVIER LICENSE
TERMS AND CONDITIONS

Mar 28, 2022

This Agreement between 500 Richland Avenue ("You") and Elsevier ("Elsevier") consists of your license details and the terms and conditions provided by Elsevier and Copyright Clearance Center.

License Number	5277860567323
License date	Mar 28, 2022
Licensed Content Publisher	Elsevier
Licensed Content Publication	Nuclear Instruments and Methods in Physics Research Section A: Accelerators, Spectrometers, Detectors and Associated Equipment
Licensed Content Title	Basic instrumentation for Hall A at Jefferson Lab
Licensed Content Author	J. Alcorn,B.D. Anderson,K.A. Aniol,J.R.M. Annand,L. Auerbach,J. Arrington,T. Averett,F.T. Baker,M. Baylac,E.J. Beise,J. Berthot,P.Y. Bertin,W. Bertozzi,L. Bimbot,T. Black,W.U. Boeglin,D.V. Boykin,E.J. Brash,V. Breton,H. Breuer,P. Brindza,D. Brown et al.
Licensed Content Date	Apr 21, 2004
Licensed Content Volume	522
Licensed Content Issue	3
Licensed Content Pages	53
Start Page	294

End Page	346
Type of Use	reuse in a thesis/dissertation
Portion	figures/tables/illustrations
Number of figures/tables/illustrations	1
Format	electronic
Are you the author of this Elsevier article?	No
Will you be translating?	No
Title	CREx Transverse Asymmetry Measurements
Institution name	Ohio University
Expected presentation date	Apr 2022
Portions	Figure 8
Requestor Location	500 Richland Avenue 500 Richland Avenue ATHENS, OH 45701 United States Attn: 500 Richland Avenue
Publisher Tax ID	98-0397604
Total	0.00 USD

Terms and Conditions

INTRODUCTION

1. The publisher for this copyrighted material is Elsevier. By clicking "accept" in connection with completing this licensing transaction, you agree that the following terms and conditions apply to this transaction (along with the Billing and Payment terms and conditions established by Copyright Clearance Center, Inc. ("CCC"), at the time that you opened your Rightslink account and that are available at any time at http://myaccount.copyright.com).

GENERAL TERMS

2. Elsevier hereby grants you permission to reproduce the aforementioned material subject to the terms and conditions indicated.

3. Acknowledgement: If any part of the material to be used (for example, figures) has appeared in our publication with credit or acknowledgement to another source, permission must also be sought from that source. If such permission is not obtained then that material may not be included in your publication/copies. Suitable acknowledgement to the source must be made, either as a footnote or in a reference list at the end of your publication, as follows:

"Reprinted from Publication title, Vol /edition number, Author(s), Title of article / title of chapter, Pages No., Copyright (Year), with permission from Elsevier [OR APPLICABLE SOCIETY COPYRIGHT OWNER]." Also Lancet special credit - "Reprinted from The Lancet, Vol. number, Author(s), Title of article, Pages No., Copyright (Year), with permission from Elsevier."

4. Reproduction of this material is confined to the purpose and/or media for which permission is hereby given.

5. Altering/Modifying Material: Not Permitted. However figures and illustrations may be altered/adapted minimally to serve your work. Any other abbreviations, additions, deletions and/or any other alterations shall be made only with prior written authorization of Elsevier Ltd. (Please contact Elsevier's permissions helpdesk here). No modifications can be made to any Lancet figures/tables and they must be reproduced in full.

6. If the permission fee for the requested use of our material is waived in this instance, please be advised that your future requests for Elsevier materials may attract a fee.

7. Reservation of Rights: Publisher reserves all rights not specifically granted in the combination of (i) the license details provided by you and accepted in the course of this licensing transaction, (ii) these terms and conditions and (iii) CCC's Billing and Payment terms and conditions.

8. License Contingent Upon Payment: While you may exercise the rights licensed immediately upon issuance of the license at the end of the licensing process for the transaction, provided that you have disclosed complete and accurate details of your proposed use, no license is finally effective unless and until full payment is received from you (either by publisher or by CCC) as provided in CCC's Billing and Payment terms and conditions. If full payment is not received on a timely basis, then any license preliminarily granted shall be deemed automatically revoked and shall be void as if never granted. Further, in the event that you breach any of these terms and conditions or any of CCC's Billing and Payment terms and conditions, the license is automatically revoked and shall be void as if never granted. Use of materials as described in a revoked license, as well as any use of the materials beyond the scope of an unrevoked license, may constitute copyright infringement

and publisher reserves the right to take any and all action to protect its copyright in the materials.

9. Warranties: Publisher makes no representations or warranties with respect to the licensed material.

10. Indemnity: You hereby indemnify and agree to hold harmless publisher and CCC, and their respective officers, directors, employees and agents, from and against any and all claims arising out of your use of the licensed material other than as specifically authorized pursuant to this license.

11. No Transfer of License: This license is personal to you and may not be sublicensed, assigned, or transferred by you to any other person without publisher's written permission.

12. No Amendment Except in Writing: This license may not be amended except in a writing signed by both parties (or, in the case of publisher, by CCC on publisher's behalf).

13. Objection to Contrary Terms: Publisher hereby objects to any terms contained in any purchase order, acknowledgment, check endorsement or other writing prepared by you, which terms are inconsistent with these terms and conditions or CCC's Billing and Payment terms and conditions. These terms and conditions, together with CCC's Billing and Payment terms and conditions (which are incorporated herein), comprise the entire agreement between you and publisher (and CCC) concerning this licensing transaction. In the event of any conflict between your obligations established by these terms and conditions and those established by CCC's Billing and Payment terms and conditions, these terms and conditions shall control.

14. Revocation: Elsevier or Copyright Clearance Center may deny the permissions described in this License at their sole discretion, for any reason or no reason, with a full refund payable to you. Notice of such denial will be made using the contact information provided by you. Failure to receive such notice will not alter or invalidate the denial. In no event will Elsevier or Copyright Clearance Center be responsible or liable for any costs, expenses or damage incurred by you as a result of a denial of your permission request, other than a refund of the amount(s) paid by you to Elsevier and/or Copyright Clearance Center for denied permissions.

LIMITED LICENSE

The following terms and conditions apply only to specific license types:

15. **Translation**: This permission is granted for non-exclusive world **English** rights only unless your license was granted for translation rights. If you licensed translation rights you may only translate this content into the languages you requested. A professional translator must perform all translations and reproduce the content word for word preserving the integrity of the article.

16. **Posting licensed content on any Website**: The following terms and conditions apply as follows: Licensing material from an Elsevier journal: All content posted to the web site must maintain the copyright information line on the bottom of each image; A hyper-text must be included to the Homepage of the journal from which you are licensing at http://www.sciencedirect.com/science/journal/xxxxx or the Elsevier homepage for books at http://www.elsevier.com; Central Storage: This license does not include permission for a scanned version of the material to be stored in a central repository such as that provided by Heron/XanEdu.

Licensing material from an Elsevier book: A hyper-text link must be included to the Elsevier homepage at http://www.elsevier.com . All content posted to the web site must maintain the copyright information line on the bottom of each image.

Posting licensed content on Electronic reserve: In addition to the above the following clauses are applicable: The web site must be password-protected and made available only to bona fide students registered on a relevant course. This permission is granted for 1 year only. You may obtain a new license for future website posting.

17. **For journal authors:** the following clauses are applicable in addition to the above:

Preprints:

A preprint is an author's own write-up of research results and analysis, it has not been peer-reviewed, nor has it had any other value added to it by a publisher (such as formatting, copyright, technical enhancement etc.).

Authors can share their preprints anywhere at any time. Preprints should not be added to or enhanced in any way in order to appear more like, or to substitute for, the final versions of articles however authors can update their preprints on arXiv or RePEc with their Accepted Author Manuscript (see below).

If accepted for publication, we encourage authors to link from the preprint to their formal publication via its DOI. Millions of researchers have access to the formal publications on ScienceDirect, and so links will help users to find, access, cite and use the best available version. Please note that Cell Press, The Lancet and some society-owned have different preprint policies. Information on these policies is available on the journal homepage.

Accepted Author Manuscripts: An accepted author manuscript is the manuscript of an article that has been accepted for publication and which typically includes author-incorporated changes suggested during submission, peer review and editor-author communications.

Authors can share their accepted author manuscript:

- immediately
  - via their non-commercial person homepage or blog
  - by updating a preprint in arXiv or RePEc with the accepted manuscript
  - via their research institute or institutional repository for internal institutional uses or as part of an invitation-only research collaboration work-group
  - directly by providing copies to their students or to research collaborators for their personal use
  - for private scholarly sharing as part of an invitation-only work group on commercial sites with which Elsevier has an agreement
- After the embargo period
  - via non-commercial hosting platforms such as their institutional repository
  - via commercial sites with which Elsevier has an agreement

In all cases accepted manuscripts should:

- link to the formal publication via its DOI
- bear a CC-BY-NC-ND license - this is easy to do
- if aggregated with other manuscripts, for example in a repository or other site, be shared in alignment with our hosting policy not be added to or enhanced in any way to

appear more like, or to substitute for, the published journal article.

Published journal article (JPA): A published journal article (PJA) is the definitive final record of published research that appears or will appear in the journal and embodies all value-adding publishing activities including peer review co-ordination, copy-editing, formatting, (if relevant) pagination and online enrichment.

Policies for sharing publishing journal articles differ for subscription and gold open access articles:

Subscription Articles: If you are an author, please share a link to your article rather than the full-text. Millions of researchers have access to the formal publications on ScienceDirect, and so links will help your users to find, access, cite, and use the best available version.

Theses and dissertations which contain embedded PJAs as part of the formal submission can be posted publicly by the awarding institution with DOI links back to the formal publications on ScienceDirect.

If you are affiliated with a library that subscribes to ScienceDirect you have additional private sharing rights for others' research accessed under that agreement. This includes use for classroom teaching and internal training at the institution (including use in course packs and courseware programs), and inclusion of the article for grant funding purposes.

Gold Open Access Articles: May be shared according to the author-selected end-user license and should contain a CrossMark logo, the end user license, and a DOI link to the formal publication on ScienceDirect.

Please refer to Elsevier's posting policy for further information.

18. **For book authors** the following clauses are applicable in addition to the above: Authors are permitted to place a brief summary of their work online only. You are not allowed to download and post the published electronic version of your chapter, nor may you scan the printed edition to create an electronic version. **Posting to a repository:** Authors are permitted to post a summary of their chapter only in their institution's repository.

19. **Thesis/Dissertation**: If your license is for use in a thesis/dissertation your thesis may be submitted to your institution in either print or electronic form. Should your thesis be published commercially, please reapply for permission. These requirements include permission for the Library and Archives of Canada to supply single copies, on demand, of the complete thesis and include permission for Proquest/UMI to supply single copies, on demand, of the complete thesis. Should your thesis be published commercially, please reapply for permission. Theses and dissertations which contain embedded PJAs as part of the formal submission can be posted publicly by the awarding institution with DOI links back to the formal publications on ScienceDirect.

Elsevier Open Access Terms and Conditions

You can publish open access with Elsevier in hundreds of open access journals or in nearly 2000 established subscription journals that support open access publishing. Permitted third party re-use of these open access articles is defined by the author's choice of Creative Commons user license. See our open access license policy for more information.

Terms & Conditions applicable to all Open Access articles published with Elsevier:

Any reuse of the article must not represent the author as endorsing the adaptation of the article nor should the article be modified in such a way as to damage the author's honour or reputation. If any changes have been made, such changes must be clearly indicated.

The author(s) must be appropriately credited and we ask that you include the end user license and a DOI link to the formal publication on ScienceDirect.

If any part of the material to be used (for example, figures) has appeared in our publication with credit or acknowledgement to another source it is the responsibility of the user to ensure their reuse complies with the terms and conditions determined by the rights holder.

Additional Terms & Conditions applicable to each Creative Commons user license:

CC BY: The CC-BY license allows users to copy, to create extracts, abstracts and new works from the Article, to alter and revise the Article and to make commercial use of the Article (including reuse and/or resale of the Article by commercial entities), provided the user gives appropriate credit (with a link to the formal publication through the relevant DOI), provides a link to the license, indicates if changes were made and the licensor is not represented as endorsing the use made of the work. The full details of the license are available at http://creativecommons.org/licenses/by/4.0.

CC BY NC SA: The CC BY-NC-SA license allows users to copy, to create extracts, abstracts and new works from the Article, to alter and revise the Article, provided this is not done for commercial purposes, and that the user gives appropriate credit (with a link to the formal publication through the relevant DOI), provides a link to the license, indicates if changes were made and the licensor is not represented as endorsing the use made of the work. Further, any new works must be made available on the same conditions. The full details of the license are available at http://creativecommons.org/licenses/by-nc-sa/4.0.

CC BY NC ND: The CC BY-NC-ND license allows users to copy and distribute the Article, provided this is not done for commercial purposes and further does not permit distribution of the Article if it is changed or edited in any way, and provided the user gives appropriate credit (with a link to the formal publication through the relevant DOI), provides a link to the license, and that the licensor is not represented as endorsing the use made of the work. The full details of the license are available at http://creativecommons.org/licenses/by-nc-nd/4.0. Any commercial reuse of Open Access articles published with a CC BY NC SA or CC BY NC ND license requires permission from Elsevier and will be subject to a fee.

Commercial reuse includes:

- Associating advertising with the full text of the Article
- Charging fees for document delivery or access
- Article aggregation
- Systematic distribution via e-mail lists or share buttons

Posting or linking by commercial companies for use by customers of those companies.

20. **Other Conditions**:

v1.10

Questions? customercare@copyright.com or +1-855-239-3415 (toll free in the US) or +1-978-646-2777.

American Physical Society
Reuse and Permissions License

28-Mar-2022

This license agreement between the American Physical Society ("APS") and Robert Radloff ("You") consists of your license details and the terms and conditions provided by the American Physical Society and SciPris.

Licensed Content Information

License Number:	**RNP/22/MAR/051963**
License date:	28-Mar-2022
DOI:	10.1103/PhysRevC.103.064316
Title:	Beam-normal single-spin asymmetry in elastic scattering of electrons from a spin-0 nucleus
Author:	Oleksandr Koshchii et al.
Publication:	Physical Review C
Publisher:	American Physical Society
Cost:	USD $ 0.00

Request Details

Does your reuse require significant modifications: No

Specify intended distribution locations:	United States
Reuse Category:	Reuse in a thesis/dissertation
Requestor Type:	Student
Items for Reuse:	Figures/Tables
Number of Figure/Tables:	2
Figure/Tables Details:	table 1, figure 5
Format for Reuse:	Electronic

Information about New Publication:

University/Publisher:	Ohio University
Title of dissertation/thesis:	crex transverse asymmetry measurements
Author(s):	Robert w Radloff
Expected completion date:	Apr. 2022

License Requestor Information

Name:	Robert Radloff
Affiliation:	Individual
Email Id:	rr521111@ohio.edu
Country:	United States

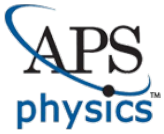

American Physical Society
Reuse and Permissions License

TERMS AND CONDITIONS

The American Physical Society (APS) is pleased to grant the Requestor of this license a non-exclusive, non-transferable permission, limited to Electronic format, provided all criteria outlined below are followed.

1. You must also obtain permission from at least one of the lead authors for each separate work, if you haven't done so already. The author's name and affiliation can be found on the first page of the published Article.
2. For electronic format permissions, Requestor agrees to provide a hyperlink from the reprinted APS material using the source material's DOI on the web page where the work appears. The hyperlink should use the standard DOI resolution URL, http://dx.doi.org/{DOI}. The hyperlink may be embedded in the copyright credit line.
3. For print format permissions, Requestor agrees to print the required copyright credit line on the first page where the material appears: "Reprinted (abstract/excerpt/figure) with permission from [(FULL REFERENCE CITATION) as follows: Author's Names, APS Journal Title, Volume Number, Page Number and Year of Publication.] Copyright (YEAR) by the American Physical Society."
4. Permission granted in this license is for a one-time use and does not include permission for any future editions, updates, databases, formats or other matters. Permission must be sought for any additional use.
5. Use of the material does not and must not imply any endorsement by APS.
6. APS does not imply, purport or intend to grant permission to reuse materials to which it does not hold copyright. It is the requestor's sole responsibility to ensure the licensed material is original to APS and does not contain the copyright of another entity, and that the copyright notice of the figure, photograph, cover or table does not indicate it was reprinted by APS with permission from another source.
7. The permission granted herein is personal to the Requestor for the use specified and is not transferable or assignable without express written permission of APS. This license may not be amended except in writing by APS.
8. You may not alter, edit or modify the material in any manner.
9. You may translate the materials only when translation rights have been granted.
10. APS is not responsible for any errors or omissions due to translation.
11. You may not use the material for promotional, sales, advertising or marketing purposes.
12. The foregoing license shall not take effect unless and until APS or its agent, Aptara, receives payment in full in accordance with Aptara Billing and Payment Terms and Conditions, which are incorporated herein by reference.
13. Should the terms of this license be violated at any time, APS or Aptara may revoke the license with no refund to you and seek relief to the fullest extent of the laws of the USA. Official written notice will be made using the contact information provided with the permission request. Failure to receive such notice will not nullify revocation of the permission.
14. APS reserves all rights not specifically granted herein.
15. This document, including the Aptara Billing and Payment Terms and Conditions, shall be the entire agreement between the parties relating to the subject matter hereof.

ELSEVIER LICENSE
TERMS AND CONDITIONS

Mar 28, 2022

This Agreement between 500 Richland Avenue ("You") and Elsevier ("Elsevier") consists of your license details and the terms and conditions provided by Elsevier and Copyright Clearance Center.

License Number	5277980006130
License date	Mar 28, 2022
Licensed Content Publisher	Elsevier
Licensed Content Publication	Nuclear Physics B
Licensed Content Title	Small-angle photon scattering on complex nuclei
Licensed Content Author	L. Criegee,G. Franke,A. Giese,Th. Kahl,G. Poelz,U. Timm,H. Werner,W. Zimmermann
Licensed Content Date	Mar 28, 1977
Licensed Content Volume	121
Licensed Content Issue	1
Licensed Content Pages	7
Start Page	38
End Page	44
Type of Use	reuse in a thesis/dissertation

Portion	figures/tables/illustrations
Number of figures/tables/illustrations	1
Format	electronic
Are you the author of this Elsevier article?	No
Will you be translating?	No
Title	CREx Transverse Asymmetry Measurements
Institution name	Ohio University
Expected presentation date	Apr 2022
Portions	figure 2
Requestor Location	500 Richland Avenue 500 Richland Avenue ATHENS, OH 45701 United States Attn: 500 Richland Avenue
Publisher Tax ID	98-0397604
Total	0.00 USD

Terms and Conditions

INTRODUCTION

1. The publisher for this copyrighted material is Elsevier. By clicking "accept" in connection with completing this licensing transaction, you agree that the following terms and conditions apply to this transaction (along with the Billing and Payment terms and conditions

established by Copyright Clearance Center, Inc. ("CCC"), at the time that you opened your Rightslink account and that are available at any time at http://myaccount.copyright.com).

GENERAL TERMS

2. Elsevier hereby grants you permission to reproduce the aforementioned material subject to the terms and conditions indicated.

3. Acknowledgement: If any part of the material to be used (for example, figures) has appeared in our publication with credit or acknowledgement to another source, permission must also be sought from that source. If such permission is not obtained then that material may not be included in your publication/copies. Suitable acknowledgement to the source must be made, either as a footnote or in a reference list at the end of your publication, as follows:

"Reprinted from Publication title, Vol /edition number, Author(s), Title of article / title of chapter, Pages No., Copyright (Year), with permission from Elsevier [OR APPLICABLE SOCIETY COPYRIGHT OWNER]." Also Lancet special credit - "Reprinted from The Lancet, Vol. number, Author(s), Title of article, Pages No., Copyright (Year), with permission from Elsevier."

4. Reproduction of this material is confined to the purpose and/or media for which permission is hereby given.

5. Altering/Modifying Material: Not Permitted. However figures and illustrations may be altered/adapted minimally to serve your work. Any other abbreviations, additions, deletions and/or any other alterations shall be made only with prior written authorization of Elsevier Ltd. (Please contact Elsevier's permissions helpdesk here). No modifications can be made to any Lancet figures/tables and they must be reproduced in full.

6. If the permission fee for the requested use of our material is waived in this instance, please be advised that your future requests for Elsevier materials may attract a fee.

7. Reservation of Rights: Publisher reserves all rights not specifically granted in the combination of (i) the license details provided by you and accepted in the course of this licensing transaction, (ii) these terms and conditions and (iii) CCC's Billing and Payment terms and conditions.

8. License Contingent Upon Payment: While you may exercise the rights licensed immediately upon issuance of the license at the end of the licensing process for the transaction, provided that you have disclosed complete and accurate details of your proposed use, no license is finally effective unless and until full payment is received from you (either by publisher or by CCC) as provided in CCC's Billing and Payment terms and conditions. If full payment is not received on a timely basis, then any license preliminarily granted shall be deemed automatically revoked and shall be void as if never granted. Further, in the event that you breach any of these terms and conditions or any of CCC's Billing and Payment terms and conditions, the license is automatically revoked and shall be void as if never granted. Use of materials as described in a revoked license, as well as any use of the materials beyond the scope of an unrevoked license, may constitute copyright infringement and publisher reserves the right to take any and all action to protect its copyright in the materials.

9. Warranties: Publisher makes no representations or warranties with respect to the licensed material.

10. Indemnity: You hereby indemnify and agree to hold harmless publisher and CCC, and their respective officers, directors, employees and agents, from and against any and all claims arising out of your use of the licensed material other than as specifically authorized pursuant to this license.

11. No Transfer of License: This license is personal to you and may not be sublicensed, assigned, or transferred by you to any other person without publisher's written permission.

12. No Amendment Except in Writing: This license may not be amended except in a writing signed by both parties (or, in the case of publisher, by CCC on publisher's behalf).

13. Objection to Contrary Terms: Publisher hereby objects to any terms contained in any purchase order, acknowledgment, check endorsement or other writing prepared by you, which terms are inconsistent with these terms and conditions or CCC's Billing and Payment terms and conditions. These terms and conditions, together with CCC's Billing and Payment terms and conditions (which are incorporated herein), comprise the entire agreement between you and publisher (and CCC) concerning this licensing transaction. In the event of any conflict between your obligations established by these terms and conditions and those established by CCC's Billing and Payment terms and conditions, these terms and conditions shall control.

14. Revocation: Elsevier or Copyright Clearance Center may deny the permissions described in this License at their sole discretion, for any reason or no reason, with a full refund payable to you. Notice of such denial will be made using the contact information provided by you. Failure to receive such notice will not alter or invalidate the denial. In no event will Elsevier or Copyright Clearance Center be responsible or liable for any costs, expenses or damage incurred by you as a result of a denial of your permission request, other than a refund of the amount(s) paid by you to Elsevier and/or Copyright Clearance Center for denied permissions.

LIMITED LICENSE

The following terms and conditions apply only to specific license types:

15. **Translation**: This permission is granted for non-exclusive world **English** rights only unless your license was granted for translation rights. If you licensed translation rights you may only translate this content into the languages you requested. A professional translator must perform all translations and reproduce the content word for word preserving the integrity of the article.

16. **Posting licensed content on any Website**: The following terms and conditions apply as follows: Licensing material from an Elsevier journal: All content posted to the web site must maintain the copyright information line on the bottom of each image; A hyper-text must be included to the Homepage of the journal from which you are licensing at http://www.sciencedirect.com/science/journal/xxxxx or the Elsevier homepage for books at http://www.elsevier.com; Central Storage: This license does not include permission for a scanned version of the material to be stored in a central repository such as that provided by Heron/XanEdu.

Licensing material from an Elsevier book: A hyper-text link must be included to the Elsevier homepage at http://www.elsevier.com . All content posted to the web site must maintain the copyright information line on the bottom of each image.

Posting licensed content on Electronic reserve: In addition to the above the following

clauses are applicable: The web site must be password-protected and made available only to bona fide students registered on a relevant course. This permission is granted for 1 year only. You may obtain a new license for future website posting.

17. **For journal authors:** the following clauses are applicable in addition to the above:

Preprints:

A preprint is an author's own write-up of research results and analysis, it has not been peer-reviewed, nor has it had any other value added to it by a publisher (such as formatting, copyright, technical enhancement etc.).

Authors can share their preprints anywhere at any time. Preprints should not be added to or enhanced in any way in order to appear more like, or to substitute for, the final versions of articles however authors can update their preprints on arXiv or RePEc with their Accepted Author Manuscript (see below).

If accepted for publication, we encourage authors to link from the preprint to their formal publication via its DOI. Millions of researchers have access to the formal publications on ScienceDirect, and so links will help users to find, access, cite and use the best available version. Please note that Cell Press, The Lancet and some society-owned have different preprint policies. Information on these policies is available on the journal homepage.

Accepted Author Manuscripts: An accepted author manuscript is the manuscript of an article that has been accepted for publication and which typically includes author-incorporated changes suggested during submission, peer review and editor-author communications.

Authors can share their accepted author manuscript:

- immediately
    - via their non-commercial person homepage or blog
    - by updating a preprint in arXiv or RePEc with the accepted manuscript
    - via their research institute or institutional repository for internal institutional uses or as part of an invitation-only research collaboration work-group
    - directly by providing copies to their students or to research collaborators for their personal use
    - for private scholarly sharing as part of an invitation-only work group on commercial sites with which Elsevier has an agreement
- After the embargo period
    - via non-commercial hosting platforms such as their institutional repository
    - via commercial sites with which Elsevier has an agreement

In all cases accepted manuscripts should:

- link to the formal publication via its DOI
- bear a CC-BY-NC-ND license - this is easy to do
- if aggregated with other manuscripts, for example in a repository or other site, be shared in alignment with our hosting policy not be added to or enhanced in any way to appear more like, or to substitute for, the published journal article.

Published journal article (JPA): A published journal article (PJA) is the definitive final record of published research that appears or will appear in the journal and embodies all value-adding publishing activities including peer review co-ordination, copy-editing, formatting, (if relevant) pagination and online enrichment.

Policies for sharing publishing journal articles differ for subscription and gold open access articles:

Subscription Articles: If you are an author, please share a link to your article rather than the full-text. Millions of researchers have access to the formal publications on ScienceDirect, and so links will help your users to find, access, cite, and use the best available version.

Theses and dissertations which contain embedded PJAs as part of the formal submission can be posted publicly by the awarding institution with DOI links back to the formal publications on ScienceDirect.

If you are affiliated with a library that subscribes to ScienceDirect you have additional private sharing rights for others' research accessed under that agreement. This includes use for classroom teaching and internal training at the institution (including use in course packs and courseware programs), and inclusion of the article for grant funding purposes.

Gold Open Access Articles: May be shared according to the author-selected end-user license and should contain a CrossMark logo, the end user license, and a DOI link to the formal publication on ScienceDirect.

Please refer to Elsevier's posting policy for further information.

18. **For book authors** the following clauses are applicable in addition to the above: Authors are permitted to place a brief summary of their work online only. You are not allowed to download and post the published electronic version of your chapter, nor may you scan the printed edition to create an electronic version. **Posting to a repository:** Authors are permitted to post a summary of their chapter only in their institution's repository.

19. **Thesis/Dissertation**: If your license is for use in a thesis/dissertation your thesis may be submitted to your institution in either print or electronic form. Should your thesis be published commercially, please reapply for permission. These requirements include permission for the Library and Archives of Canada to supply single copies, on demand, of the complete thesis and include permission for Proquest/UMI to supply single copies, on demand, of the complete thesis. Should your thesis be published commercially, please reapply for permission. Theses and dissertations which contain embedded PJAs as part of the formal submission can be posted publicly by the awarding institution with DOI links back to the formal publications on ScienceDirect.

Elsevier Open Access Terms and Conditions

You can publish open access with Elsevier in hundreds of open access journals or in nearly 2000 established subscription journals that support open access publishing. Permitted third party re-use of these open access articles is defined by the author's choice of Creative Commons user license. See our open access license policy for more information.

Terms & Conditions applicable to all Open Access articles published with Elsevier:

Any reuse of the article must not represent the author as endorsing the adaptation of the article nor should the article be modified in such a way as to damage the author's honour or reputation. If any changes have been made, such changes must be clearly indicated.

The author(s) must be appropriately credited and we ask that you include the end user license and a DOI link to the formal publication on ScienceDirect.

If any part of the material to be used (for example, figures) has appeared in our publication with credit or acknowledgement to another source it is the responsibility of the user to ensure their reuse complies with the terms and conditions determined by the rights holder.

Additional Terms & Conditions applicable to each Creative Commons user license:

CC BY: The CC-BY license allows users to copy, to create extracts, abstracts and new works from the Article, to alter and revise the Article and to make commercial use of the Article (including reuse and/or resale of the Article by commercial entities), provided the user gives appropriate credit (with a link to the formal publication through the relevant DOI), provides a link to the license, indicates if changes were made and the licensor is not represented as endorsing the use made of the work. The full details of the license are available at http://creativecommons.org/licenses/by/4.0.

CC BY NC SA: The CC BY-NC-SA license allows users to copy, to create extracts, abstracts and new works from the Article, to alter and revise the Article, provided this is not done for commercial purposes, and that the user gives appropriate credit (with a link to the formal publication through the relevant DOI), provides a link to the license, indicates if changes were made and the licensor is not represented as endorsing the use made of the work. Further, any new works must be made available on the same conditions. The full details of the license are available at http://creativecommons.org/licenses/by-nc-sa/4.0.

CC BY NC ND: The CC BY-NC-ND license allows users to copy and distribute the Article, provided this is not done for commercial purposes and further does not permit distribution of the Article if it is changed or edited in any way, and provided the user gives appropriate credit (with a link to the formal publication through the relevant DOI), provides a link to the license, and that the licensor is not represented as endorsing the use made of the work. The full details of the license are available at http://creativecommons.org/licenses/by-nc-nd/4.0. Any commercial reuse of Open Access articles published with a CC BY NC SA or CC BY NC ND license requires permission from Elsevier and will be subject to a fee.

Commercial reuse includes:

- Associating advertising with the full text of the Article
- Charging fees for document delivery or access
- Article aggregation
- Systematic distribution via e-mail lists or share buttons

Posting or linking by commercial companies for use by customers of those companies.

20. **Other Conditions**:

v1.10

Questions? customercare@copyright.com or +1-855-239-3415 (toll free in the US) or +1-978-646-2777.

American Physical Society
Reuse and Permissions License

23-Apr-2022

This license agreement between the American Physical Society ("APS") and Robert Radloff ("You") consists of your license details and the terms and conditions provided by the American Physical Society and SciPris.

Licensed Content Information

License Number:	**RNP/22/APR/052891**
License date:	23-Apr-2022
DOI:	10.1103/PhysRevC.102.015501
Title:	High precision 5 MeV Mott polarimeter
Author:	J. M. Grames et al.
Publication:	Physical Review C
Publisher:	American Physical Society
Cost:	USD $ 0.00

Request Details

Does your reuse require significant modifications: No

Specify intended distribution locations:	Worldwide
Reuse Category:	Reuse in a thesis/dissertation
Requestor Type:	Student
Items for Reuse:	Figures/Tables
Number of Figure/Tables:	2
Figure/Tables Details:	mott polarimeter diagrams
Format for Reuse:	Electronic

Information about New Publication:

University/Publisher:	Ohio University
Title of dissertation/thesis:	CREx transverse asymmetry Measurements
Author(s):	Robert Radloff
Expected completion date:	Apr. 2022

License Requestor Information

Name:	Robert Radloff
Affiliation:	Individual
Email Id:	rr521111@ohio.edu
Country:	United States

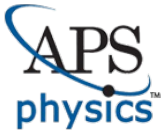

American Physical Society
Reuse and Permissions License

TERMS AND CONDITIONS

The American Physical Society (APS) is pleased to grant the Requestor of this license a non-exclusive, non-transferable permission, limited to Electronic format, provided all criteria outlined below are followed.

1. You must also obtain permission from at least one of the lead authors for each separate work, if you haven't done so already. The author's name and affiliation can be found on the first page of the published Article.
2. For electronic format permissions, Requestor agrees to provide a hyperlink from the reprinted APS material using the source material's DOI on the web page where the work appears. The hyperlink should use the standard DOI resolution URL, http://dx.doi.org/{DOI}. The hyperlink may be embedded in the copyright credit line.
3. For print format permissions, Requestor agrees to print the required copyright credit line on the first page where the material appears: "Reprinted (abstract/excerpt/figure) with permission from [(FULL REFERENCE CITATION) as follows: Author's Names, APS Journal Title, Volume Number, Page Number and Year of Publication.] Copyright (YEAR) by the American Physical Society."
4. Permission granted in this license is for a one-time use and does not include permission for any future editions, updates, databases, formats or other matters. Permission must be sought for any additional use.
5. Use of the material does not and must not imply any endorsement by APS.
6. APS does not imply, purport or intend to grant permission to reuse materials to which it does not hold copyright. It is the requestor's sole responsibility to ensure the licensed material is original to APS and does not contain the copyright of another entity, and that the copyright notice of the figure, photograph, cover or table does not indicate it was reprinted by APS with permission from another source.
7. The permission granted herein is personal to the Requestor for the use specified and is not transferable or assignable without express written permission of APS. This license may not be amended except in writing by APS.
8. You may not alter, edit or modify the material in any manner.
9. You may translate the materials only when translation rights have been granted.
10. APS is not responsible for any errors or omissions due to translation.
11. You may not use the material for promotional, sales, advertising or marketing purposes.
12. The foregoing license shall not take effect unless and until APS or its agent, Aptara, receives payment in full in accordance with Aptara Billing and Payment Terms and Conditions, which are incorporated herein by reference.
13. Should the terms of this license be violated at any time, APS or Aptara may revoke the license with no refund to you and seek relief to the fullest extent of the laws of the USA. Official written notice will be made using the contact information provided with the permission request. Failure to receive such notice will not nullify revocation of the permission.
14. APS reserves all rights not specifically granted herein.
15. This document, including the Aptara Billing and Payment Terms and Conditions, shall be the entire agreement between the parties relating to the subject matter hereof.

CCC Marketplace™

This is a License Agreement between Robert Radloff ("User") and Copyright Clearance Center, Inc. ("CCC") on behalf of the Rightsholder identified in the order details below. The license consists of the order details, the CCC Terms and Conditions below, and any Rightsholder Terms and Conditions which are included below.

All payments must be made in full to CCC in accordance with the CCC Terms and Conditions below.

Order Date	23-Apr-2022	**Type of Use**	Republish in a thesis/dissertation
Order License ID	1214169-1		
ISSN	0954-3899	**Publisher**	IOP Publishing
		Portion	Image/photo/illustration

LICENSED CONTENT

Publication Title	Journal of Physics G	**Country**	United Kingdom of Great Britain and Northern Ireland
Author/Editor	Institute of Physics (Great Britain)	**Rightsholder**	IOP Publishing, Ltd
Date	01/01/1989	**Publication Type**	Journal
Language	English		

REQUEST DETAILS

Portion Type	Image/photo/illustration	**Distribution**	Worldwide
Number of images / photos / illustrations	1	**Translation**	Original language of publication
Format (select all that apply)	Electronic	**Copies for the disabled?**	No
		Minor editing privileges?	No
Who will republish the content?	Academic institution	**Incidental promotional use?**	No
Duration of Use	Life of current edition	**Currency**	USD
Lifetime Unit Quantity	Up to 499		
Rights Requested	Main product		

NEW WORK DETAILS

Title	Crex transverse asymmetry measurements	**Institution name**	Ohio University
		Expected presentation date	2022-04-23
Instructor name	Paul King		

ADDITIONAL DETAILS

Order reference number	N/A	**The requesting person / organization to appear on the license**	Robert Radloff

REUSE CONTENT DETAILS

Title, description or numeric reference of the portion(s)	journal of physics g	**Title of the article/chapter the portion is from**	Neutron skins of atomic nuclei: per aspera ad astra
Editor of portion(s)	na	**Author of portion(s)**	Institute of Physics (Great Britain)
Volume of serial or monograph	na	**Issue, if republishing an article from a serial**	N/A
Page or page range of portion	093003	**Publication date of portion**	1989-01-01

RIGHTSHOLDER TERMS AND CONDITIONS

These special terms and conditions are in addition to the standard terms and conditions for CCC's Republication Service and, together with those standard terms and conditions, govern the use of the Works. As the User you will make all reasonable efforts to contact the author(s) of the article which the Work is to be reused from, to seek consent for your intended use. Contacting one author who is acting expressly as authorised agent for their co-author(s) is acceptable. User will reproduce the following wording prominently alongside the Work: the source of the Work, including author, article title, title of journal, volume number, issue number (if relevant), page range (or first page if this is the only information available) and date of first publication; and a link back to the article (via DOI); and if practicable, and IN ALL CASES for new works published under any of the Creative Commons licences, the words "© IOP Publishing. Reproduced with permission. All rights reserved" Without the express permission of the author(s) and the Rightsholder of the article from which the Work is to be reused, User shall not use it in any way which, in the opinion of the Rightsholder, could: (i) distort or alter the author(s)' original intention(s) and meaning; (ii) be prejudicial to the honour or reputation of the author(s); and/or (iii) imply endorsement by the author(s) and/or the Rightsholder. This licence does not apply to any article which is credited to another source and which does not have the copyright line '© IOP Publishing Ltd'. User must check the copyright line of the article from which the Work is to be reused to check that IOP Publishing Ltd has all the necessary rights to be able to grant permission. User is solely responsible for identifying and obtaining separate licences and permissions from the copyright owner for reuse of any such third party material/figures which the Rightsholder is not the copyright owner of. The Rightsholder shall not reimburse any fees which User pays for a republication license for such third party content. This licence does not apply to any material/figure which is credited to another source in the Rightsholder's publication or has been obtained from a third party. User must check the Version of Record of the article from which the Work is to be reused, to check whether any of the material in the Work is third party material. Third party citations and/or copyright notices and/or permissions statements may not be included in any other version of the article from which the Work is to be reused and so cannot be relied upon by the User. User is solely responsible for identifying and obtaining separate licences and permissions from the copyright owner for reuse of any such third party material/figures where the Rightsholder is not the copyright owner. The Rightsholder shall not reimburse any fees which User pays for a republication license for such third party content. User and CCC acknowledge that the Rightsholder may, from time to time, make changes or additions to these special terms and conditions without express notification, provided that these shall not apply to permissions already secured and paid for by User prior to such change or addition. User acknowledges that the Rightsholder (which includes companies within its group and third parties for whom it publishes its titles) may make use of personal data collected through the service in the course of their business. If User is the author of the Work, User may automatically have the right to reuse it under the rights granted back when User transferred the copyright in the article to the Rightsholder. User should check the copyright form and the relevant author rights policy to check whether permission is required. If User is the author of the Work and does require permission for proposed reuse of the Work, User should select 'Author of requested content' as the Requestor Type. The Rightsholder shall not reimburse any fees which User pays for a republication license. If User is the author of the article which User wishes to reuse in User's thesis or dissertation, the republication licence covers the right to include the Version of Record of the article, provided it is not then shared or deposited online. User must include citation details. Where User wishes to share their thesis or dissertation online, they should remove the Version of Record before uploading it. User may include a Preprint or the Accepted Manuscript (after the embargo period) in the online version of the thesis or dissertation, provided they do so in accordance with the Rightsholder's policies on sharing Preprints or Accepted Manuscripts. User may need to obtain separate permission for any third party content included within the article. User must check this with the copyright owner of such third party content. Any online or commercial use of User's thesis or dissertation containing the article, including publication via ProQuest, would need to be expressly notified in writing to the Rightsholder at the time of request and would require separate written permission from the Rightsholder. As well as CCC, the Rightsholder shall have the right to bring any legal action that it deems necessary to enforce its rights should it consider that the Work infringes those rights in any way. For content reuse requests that qualify for permission under the STM Permissions Guidelines, which may be

updated from time to time, the STM Permissions Guidelines supplement the terms and conditions contained in this license.

CCC Terms and Conditions

1. Description of Service; Defined Terms. This Republication License enables the User to obtain licenses for republication of one or more copyrighted works as described in detail on the relevant Order Confirmation (the "Work(s)"). Copyright Clearance Center, Inc. ("CCC") grants licenses through the Service on behalf of the rightsholder identified on the Order Confirmation (the "Rightsholder"). "Republication", as used herein, generally means the inclusion of a Work, in whole or in part, in a new work or works, also as described on the Order Confirmation. "User", as used herein, means the person or entity making such republication.

2. The terms set forth in the relevant Order Confirmation, and any terms set by the Rightsholder with respect to a particular Work, govern the terms of use of Works in connection with the Service. By using the Service, the person transacting for a republication license on behalf of the User represents and warrants that he/she/it (a) has been duly authorized by the User to accept, and hereby does accept, all such terms and conditions on behalf of User, and (b) shall inform User of all such terms and conditions. In the event such person is a "freelancer" or other third party independent of User and CCC, such party shall be deemed jointly a "User" for purposes of these terms and conditions. In any event, User shall be deemed to have accepted and agreed to all such terms and conditions if User republishes the Work in any fashion.

3. Scope of License; Limitations and Obligations.

    3.1. All Works and all rights therein, including copyright rights, remain the sole and exclusive property of the Rightsholder. The license created by the exchange of an Order Confirmation (and/or any invoice) and payment by User of the full amount set forth on that document includes only those rights expressly set forth in the Order Confirmation and in these terms and conditions, and conveys no other rights in the Work(s) to User. All rights not expressly granted are hereby reserved.

    3.2. General Payment Terms: You may pay by credit card or through an account with us payable at the end of the month. If you and we agree that you may establish a standing account with CCC, then the following terms apply: Remit Payment to: Copyright Clearance Center, 29118 Network Place, Chicago, IL 60673-1291. Payments Due: Invoices are payable upon their delivery to you (or upon our notice to you that they are available to you for downloading). After 30 days, outstanding amounts will be subject to a service charge of 1-1/2% per month or, if less, the maximum rate allowed by applicable law. Unless otherwise specifically set forth in the Order Confirmation or in a separate written agreement signed by CCC, invoices are due and payable on "net 30" terms. While User may exercise the rights licensed immediately upon issuance of the Order Confirmation, the license is automatically revoked and is null and void, as if it had never been issued, if complete payment for the license is not received on a timely basis either from User directly or through a payment agent, such as a credit card company.

    3.3. Unless otherwise provided in the Order Confirmation, any grant of rights to User (i) is "one-time" (including the editions and product family specified in the license), (ii) is non-exclusive and non-transferable and (iii) is subject to any and all limitations and restrictions (such as, but not limited to, limitations on duration of use or circulation) included in the Order Confirmation or invoice and/or in these terms and conditions. Upon completion of the licensed use, User shall either secure a new permission for further use of the Work(s) or immediately cease any new use of the Work(s) and shall render inaccessible (such as by deleting or by removing or severing links or other locators) any further copies of the Work (except for copies printed on paper in accordance with this license and still in User's stock at the end of such period).

    3.4. In the event that the material for which a republication license is sought includes third party materials (such as photographs, illustrations, graphs, inserts and similar materials) which are identified in such material as having been used by permission, User is responsible for identifying, and seeking separate licenses (under this Service or otherwise) for, any of such third party materials; without a separate license, such third party materials may not be used.

    3.5.

Use of proper copyright notice for a Work is required as a condition of any license granted under the Service. Unless otherwise provided in the Order Confirmation, a proper copyright notice will read substantially as follows: "Republished with permission of [Rightsholder's name], from [Work's title, author, volume, edition number and year of copyright]; permission conveyed through Copyright Clearance Center, Inc. " Such notice must be provided in a reasonably legible font size and must be placed either immediately adjacent to the Work as used (for example, as part of a by-line or footnote but not as a separate electronic link) or in the place where substantially all other credits or notices for the new work containing the republished Work are located. Failure to include the required notice results in loss to the Rightsholder and CCC, and the User shall be liable to pay liquidated damages for each such failure equal to twice the use fee specified in the Order Confirmation, in addition to the use fee itself and any other fees and charges specified.

3.6. User may only make alterations to the Work if and as expressly set forth in the Order Confirmation. No Work may be used in any way that is defamatory, violates the rights of third parties (including such third parties' rights of copyright, privacy, publicity, or other tangible or intangible property), or is otherwise illegal, sexually explicit or obscene. In addition, User may not conjoin a Work with any other material that may result in damage to the reputation of the Rightsholder. User agrees to inform CCC if it becomes aware of any infringement of any rights in a Work and to cooperate with any reasonable request of CCC or the Rightsholder in connection therewith.

4. Indemnity. User hereby indemnifies and agrees to defend the Rightsholder and CCC, and their respective employees and directors, against all claims, liability, damages, costs and expenses, including legal fees and expenses, arising out of any use of a Work beyond the scope of the rights granted herein, or any use of a Work which has been altered in any unauthorized way by User, including claims of defamation or infringement of rights of copyright, publicity, privacy or other tangible or intangible property.

5. Limitation of Liability. UNDER NO CIRCUMSTANCES WILL CCC OR THE RIGHTSHOLDER BE LIABLE FOR ANY DIRECT, INDIRECT, CONSEQUENTIAL OR INCIDENTAL DAMAGES (INCLUDING WITHOUT LIMITATION DAMAGES FOR LOSS OF BUSINESS PROFITS OR INFORMATION, OR FOR BUSINESS INTERRUPTION) ARISING OUT OF THE USE OR INABILITY TO USE A WORK, EVEN IF ONE OF THEM HAS BEEN ADVISED OF THE POSSIBILITY OF SUCH DAMAGES. In any event, the total liability of the Rightsholder and CCC (including their respective employees and directors) shall not exceed the total amount actually paid by User for this license. User assumes full liability for the actions and omissions of its principals, employees, agents, affiliates, successors and assigns.

6. Limited Warranties. THE WORK(S) AND RIGHT(S) ARE PROVIDED "AS IS". CCC HAS THE RIGHT TO GRANT TO USER THE RIGHTS GRANTED IN THE ORDER CONFIRMATION DOCUMENT. CCC AND THE RIGHTSHOLDER DISCLAIM ALL OTHER WARRANTIES RELATING TO THE WORK(S) AND RIGHT(S), EITHER EXPRESS OR IMPLIED, INCLUDING WITHOUT LIMITATION IMPLIED WARRANTIES OF MERCHANTABILITY OR FITNESS FOR A PARTICULAR PURPOSE. ADDITIONAL RIGHTS MAY BE REQUIRED TO USE ILLUSTRATIONS, GRAPHS, PHOTOGRAPHS, ABSTRACTS, INSERTS OR OTHER PORTIONS OF THE WORK (AS OPPOSED TO THE ENTIRE WORK) IN A MANNER CONTEMPLATED BY USER; USER UNDERSTANDS AND AGREES THAT NEITHER CCC NOR THE RIGHTSHOLDER MAY HAVE SUCH ADDITIONAL RIGHTS TO GRANT.

7. Effect of Breach. Any failure by User to pay any amount when due, or any use by User of a Work beyond the scope of the license set forth in the Order Confirmation and/or these terms and conditions, shall be a material breach of the license created by the Order Confirmation and these terms and conditions. Any breach not cured within 30 days of written notice thereof shall result in immediate termination of such license without further notice. Any unauthorized (but licensable) use of a Work that is terminated immediately upon notice thereof may be liquidated by payment of the Rightsholder's ordinary license price therefor; any unauthorized (and unlicensable) use that is not terminated immediately for any reason (including, for example, because materials containing the Work cannot reasonably be recalled) will be subject to all remedies available at law or in equity, but in no event to a payment of less than three times the Rightsholder's ordinary license price for the most closely analogous licensable use plus Rightsholder's and/or CCC's costs and expenses incurred in collecting such payment.

8. Miscellaneous.

8.1.

User acknowledges that CCC may, from time to time, make changes or additions to the Service or to these terms and conditions, and CCC reserves the right to send notice to the User by electronic mail or otherwise for the purposes of notifying User of such changes or additions; provided that any such changes or additions shall not apply to permissions already secured and paid for.

8.2. Use of User-related information collected through the Service is governed by CCC's privacy policy, available online here:https://marketplace.copyright.com/rs-ui-web/mp/privacy-policy

8.3. The licensing transaction described in the Order Confirmation is personal to User. Therefore, User may not assign or transfer to any other person (whether a natural person or an organization of any kind) the license created by the Order Confirmation and these terms and conditions or any rights granted hereunder; provided, however, that User may assign such license in its entirety on written notice to CCC in the event of a transfer of all or substantially all of User's rights in the new material which includes the Work(s) licensed under this Service.

8.4. No amendment or waiver of any terms is binding unless set forth in writing and signed by the parties. The Rightsholder and CCC hereby object to any terms contained in any writing prepared by the User or its principals, employees, agents or affiliates and purporting to govern or otherwise relate to the licensing transaction described in the Order Confirmation, which terms are in any way inconsistent with any terms set forth in the Order Confirmation and/or in these terms and conditions or CCC's standard operating procedures, whether such writing is prepared prior to, simultaneously with or subsequent to the Order Confirmation, and whether such writing appears on a copy of the Order Confirmation or in a separate instrument.

8.5. The licensing transaction described in the Order Confirmation document shall be governed by and construed under the law of the State of New York, USA, without regard to the principles thereof of conflicts of law. Any case, controversy, suit, action, or proceeding arising out of, in connection with, or related to such licensing transaction shall be brought, at CCC's sole discretion, in any federal or state court located in the County of New York, State of New York, USA, or in any federal or state court whose geographical jurisdiction covers the location of the Rightsholder set forth in the Order Confirmation. The parties expressly submit to the personal jurisdiction and venue of each such federal or state court.If you have any comments or questions about the Service or Copyright Clearance Center, please contact us at 978-750-8400 or send an e-mail to support@copyright.com.

v 1.1

Thesis and Dissertation Services